




2021

UNDERSTANDING THE ROLE OF CHARGE ON PARTICLE TRANSPORT WITHIN SEMIDILUTE AND CONCENTRATED BIOPOLYMER SOLUTIONS AND TAU PROTEIN CONDENSATES

Kanthi Nuti

University of Kentucky, kanthi.nuti@gmail.com

Author ORCID Identifier:

 <https://orcid.org/0000-0003-0862-4689>

Digital Object Identifier: <https://doi.org/10.13023/etd.2021.375>

[Right click to open a feedback form in a new tab to let us know how this document benefits you.](#)

Recommended Citation

Nuti, Kanthi, "UNDERSTANDING THE ROLE OF CHARGE ON PARTICLE TRANSPORT WITHIN SEMIDILUTE AND CONCENTRATED BIOPOLYMER SOLUTIONS AND TAU PROTEIN CONDENSATES" (2021). *Theses and Dissertations--Chemistry*. 149.

https://uknowledge.uky.edu/chemistry_etds/149

This Doctoral Dissertation is brought to you for free and open access by the Chemistry at UKnowledge. It has been accepted for inclusion in Theses and Dissertations--Chemistry by an authorized administrator of UKnowledge. For more information, please contact UKnowledge@lsv.uky.edu.

STUDENT AGREEMENT:

I represent that my thesis or dissertation and abstract are my original work. Proper attribution has been given to all outside sources. I understand that I am solely responsible for obtaining any needed copyright permissions. I have obtained needed written permission statement(s) from the owner(s) of each third-party copyrighted matter to be included in my work, allowing electronic distribution (if such use is not permitted by the fair use doctrine) which will be submitted to UKnowledge as Additional File.

I hereby grant to The University of Kentucky and its agents the irrevocable, non-exclusive, and royalty-free license to archive and make accessible my work in whole or in part in all forms of media, now or hereafter known. I agree that the document mentioned above may be made available immediately for worldwide access unless an embargo applies.

I retain all other ownership rights to the copyright of my work. I also retain the right to use in future works (such as articles or books) all or part of my work. I understand that I am free to register the copyright to my work.

REVIEW, APPROVAL AND ACCEPTANCE

The document mentioned above has been reviewed and accepted by the student's advisor, on behalf of the advisory committee, and by the Director of Graduate Studies (DGS), on behalf of the program; we verify that this is the final, approved version of the student's thesis including all changes required by the advisory committee. The undersigned agree to abide by the statements above.

Kanthi Nuti, Student

Dr. Jason DeRouchey, Major Professor

Dr. Yinan Wei, Director of Graduate Studies

UNDERSTANDING THE ROLE OF CHARGE ON PARTICLE TRANSPORT
WITHIN SEMIDILUTE AND CONCENTRATED BIOPOLYMER SOLUTIONS AND
TAU PROTEIN CONDENSATES

DISSERTATION

A dissertation submitted in partial fulfillment of the
requirements for the degree of Doctor of Philosophy in the
College of Arts and Sciences
at the University of Kentucky

By
Kanthi Nuti
Lexington, Kentucky
Director: Dr. Jason DeRouchey, Associate Professor of Chemistry
Lexington, Kentucky
2021

Copyright © Kanthi Nuti 2021
<https://orcid.org/0000-0003-0862-4689>

ABSTRACT OF DISSERTATION

UNDERSTANDING THE ROLE OF CHARGE ON PARTICLE TRANSPORT WITHIN SEMIDILUTE AND CONCENTRATED BIOPOLYMER SOLUTIONS AND TAU PROTEIN CONDENSATES

Biological polymer networks such as mucus, extracellular matrix, nuclear pore complex, and bacterial biofilms, play a critical role in governing the transport of nutrients, biomolecules and particles within cells and tissues. The interactions between particle and polymer chains are responsible for effective selective filtering of particles within these macromolecular networks. This selective filtering is not dictated by steric alone but must use additional interactions such as electrostatics, hydrophobic and hydrodynamic effects to control particle transport within biogels. Depending on chemical composition and desired function, biogels use selective filtering to allow some particles to permeate while preventing others from penetrating the biogel. The mechanisms underlying selective filtering are still not well understood yet have important ramifications for a variety of biomedical applications. Controlling these non-steric interactions are critical to understanding molecular transport *in vivo* as well as for engineering optimized gel-penetrating therapeutics. Fluorescence correlation spectroscopy (FCS) is an ideal tool to study particle transport properties within uncharged and charged polymer solutions. In this dissertation, our research focuses primarily on the role of electrostatics on the particle diffusion behavior within polymer solutions in the semi-dilute and concentrated regimes.

Using a series of charged dye molecules, with similar size and core chemistry but varying net molecular charge, we systematically investigated their diffusion behavior in polymer solutions and networks made up of polysaccharide and proteins. Specifically, we studied in Chapter 3 the probe diffusion in semidilute and concentrated dextran solutions. The hindered diffusion observed in attractive gels is dependent on the probe net charge and shows a dependence on the solution ionic strength. Using a biotinylated probe, we also show evidence of an additional non-electrostatic interaction between the biotin molecule and the dextran polymer chains. In contrast, comparisons to a highly charged, water soluble polyvinylamine (PVAm) semidilute solution shows that all probes, regardless of charge,

were highly hindered and a weaker dependence on solution ionic strength was observed. In Chapter 4, we characterized the transport properties of our probe molecules within pure and mixed charge solutions of amino(+)-dextran and carboxymethyl(-)-dextran. We show that these mixed charge polymer solutions still have the potential to be efficient filters for interacting particles even with comparably few attractive interaction sites. By chemical modification of the amino dextran, we also compare these results to those obtained in polyampholytic solutions. Lastly, we investigate the transport properties of both probes and a much larger bovine serum albumin (BSA) protein molecule within liquid-liquid phase separated (LLPS) tau protein in chapter 5. Tau is an intrinsically disordered protein with both positive and negatively charged amino acids. We show that despite having a high local protein concentration, tau droplets are relatively low density and comparable to semi-dilute polymer solutions. Both probe molecules and BSA are observed by FCS to be recruited within the liquid droplet resulting in $\sim 10x$ fold increase in particle concentration inside the tau droplet compared to outside. Probe transport within the phase separated tau is sensitive to probe net charge and solution ionic strength. Lastly, we show that BSA transport inside the tau droplet can be fairly well described by using Stokes-Einstein adjusted for the experimentally determined microviscosity within the tau droplet.

Keywords: diffusion, biological gels, fluorescence correlation spectroscopy, electrostatic, interaction filtering

Kanthi Nuti

(Name of Student)

08/20/2021

Date

UNDERSTANDING THE ROLE OF CHARGE ON PARTICLE TRANSPORT
WITHIN SEMIDILUTE AND CONCENTRATED BIOPOLYMER SOLUTIONS AND
TAU PROTEIN CONDENSATES

By
Kanthi Nuti

Dr. Jason DeRouchey

Director of Dissertation

Dr. Yinan Wei

Director of Graduate Studies

08/20/2021

ACKNOWLEDGMENTS

I would like to thank my advisor Dr. Jason DeRouchey for his mentorship, guidance, and understanding throughout my graduate studies. I could not have imagined having a better advisor and there are no words that can express my gratitude for everything he has done for me. I am very appreciative of the assistance and perspective I was given by Dr. Trevor Creamer for tau project experiments, and I am thankful for his time and expertise. Additionally, I would like to acknowledge my group members Daniel Kirchoff, Joseph Duke, Ehigbai Oikeh, Md Nasir Uddin, Md Abu Monsur Dinar, Richard Mitchell for their support, assistance, and friendship. Furthermore, I am grateful to my committee members Dr. Stephen Testa, Dr. Trevor Creamer, Dr. Christopher Richards for their time, and suggestions on my research work. I also want to specially thank Dr. Christopher Richards for sharing his great knowledge about instrumental trouble shooting and training on confocal imaging. I really appreciate his detailed explanation about every part of the instrument and his patience in guiding new trainees to learn.

Finally, I would like to thank my family for their love, sacrifices and for their faith in me over the course of my graduate studies. This last word of acknowledgment I have saved for my husband, Rohit Charepalli. I am thankful for his endless love, support, understanding and confidence on our relationship during the time we are separated.

TABLE OF CONTENTS

ACKNOWLEDGMENTS	iii
LIST OF TABLES	viii
LIST OF FIGURES	ix
CHAPTER 1 INTRODUCTION	1
1.1 Biological Hydrogels.....	1
1.2 Permeability of biogels.....	3
1.3 Composition of biogels.....	4
1.4 Filtration strategies	6
1.4.1 Size filtering	6
1.4.2 Interaction filtering.....	8
1.4.2.1 Regulation of particle diffusion in saccharide-based hydrogels.....	10
1.4.2.2 Regulation of particle diffusion in protein-based hydrogels.....	11
1.5 Charge-charge interactions in model hydrogels	12
1.6 Dissertation outline.....	14
CHAPTER 2. FLOURESCENCE CORRELATION SPECTROSCOPY	16
2.1 Introduction	16
2.2 Principle of FCS	16
2.2.1 Autocorrelation.....	16
2.2.2 Triplet state.....	18
2.3 FCS Experimental set up.....	20
2.3.1 Detectors in FCS	21
2.4 Application of FCS in polymers.....	24
2.4.1 Translational diffusion coefficient and concentration measurements.....	24
2.4.2 Association and dissociation event studies	25
2.5 Application of FCS in polyelectrolytes	27
2.6 Application of FCS in in vivo	29
2.6.1 Diffusion studies within cell	29

2.6.2 Diffusion studies on membrane.....	29
2.6.3 Directed transport.....	30
CHAPTER 3 PARTICLE TRANSPORT IN SEMIDILUTE POLYMERS: EFFECT OF PARTICLE CHARGE AND POLYMER CHAIN CHARGE DENSITY	31
3.1 Introduction	31
3.2 Materials and methods.....	34
3.2.1 Materials.....	34
3.2.2 Preparation of methyl ester terminated ATTO.....	35
3.2.3 Preparation of polymer solutions	35
3.2.4 Preparation of PEG-coated glass.....	36
3.2.5 FCS set-up.....	36
3.2.6 FCS data analysis	37
3.3 Results and discussion.....	38
3.3.1 Solution behavior of polymers	38
3.3.2 Dextran and polyvinylamine polymer.....	39
3.3.3 Fluorescent probes.....	41
3.3.4 Polymer properties and calculation of overlap concentration c^*	43
3.3.5 Microviscosity for probe diffusion in neutral polymer networks	45
3.3.6 Probe transport properties inside neutral and charged semidilute polymers.....	48
3.3.7 Effect of probe charge on particle transport in semidilute dextran and PVAm solutions	50
3.3.8 Particle transport of a biotinylated-dye probe in semidilute dextran and PVAm solutions	52
3.3.9 Salt effects on probe transport within charged semidilute polymer solutions ..	55
3.4 Conclusions	57
CHAPTER 4 TRANSPORT PROPERTIES BASED ON LOCAL DISTRIBUTION OF MIXED ATTRACTIVE AND REPULSIVE INTERACTIONS	58
4.1 Introduction	58
4.2 Materials and methods.....	62
4.2.1 Materials.....	62
4.2.2 Synthesis of succinylated amino dextran	62

4.2.3 Preparation of dextran solutions.....	63
4.2.4 FCS set up	63
4.2.5 FCS data analysis	64
4.3 Results and discussion	65
4.3.1 Charged dextrans structure and their properties.....	65
4.3.2 Probe transport in charged dextran solutions	66
4.3.3 Probe transport in mixed charged gels	68
4.3.4 Synthesis and characterization of N-succinylated amino dextran (NSA-Dex). 70	
4.3.4.1 ¹ H-NMR spectra of Am-Dex and NSA-Dex polymers	72
4.3.4.2 FTIR spectra of Am-Dex and NSA-Dex polymers	73
4.3.5 Determination of particle transport in polyampholytic dextran solutions.....	74
4.4 Conclusion	76
CHAPTER 5 CONSTRAINED PARTICLE TRANSPORT WITHIN PHASE- SEPARATED LIQUID DROPLETS OF TAU PROTEIN	78
5.1 Structure and function of tau	78
5.1.1 Liquid-liquid phase separations (LLPS)	80
5.1.2 Role of tau droplets in formation of microtubule bundles	84
5.1.3 Mechanism of tau aggregation	85
5.1.4 Project overview.....	86
5.2 Materials and methods.....	89
5.2.1 Materials.....	89
5.2.2 Droplet formation.....	89
5.2.3 Sample preparation with fluorophores	90
5.2.4 Confocal imaging	90
5.2.5 FCS set up	90
5.2.6 FCS data analysis	91
5.2.7 Micro viscosity measurements from Stokes-Einstein equation	92
5.3 Results and discussion	92
5.3.1 Droplet solution profile showing differential interaction for probes	92
5.3.2 R110 diffusion within tau solution, dextran solution and tau condensates.....	95
5.3.3 Electrostatic effects on particle transport within tau condensates.....	99

5.3.4 Protein transport within protein droplets.....	104
5.3.5 Dependency of ionic strength on tau droplet formation and particle transport inside droplets	107
5.4 Conclusion.....	110
References.....	112
Vita	130

LIST OF TABLES

Table 3.1 Molecular dimensions of polymers as determined for R_g , c^* , ξ	44
Table 4.1 Percent degree of substitution for NSA-Dex synthesized from different mole ratios of Am-Dex and succinic anhydride	72

LIST OF FIGURES

1.1 Steric effects on particle transport in polymeric gels of a given mesh size	7
1.2 Biopolymer based hydrogels acting as selective permeable barriers for microscopic particle translocation.....	9
2.1 Overview of Fluorescence correlation spectroscopy (FCS)	17
2.2 Jablonski diagram showing possible radiative process of absorption, emission by solid arrows and non-radiative transitions by dashed arrows	19
2.3 Schematic representation of experimental FCS set up	20
2.4 Photomultiplier tube used for photon detection in our FCS	22
2.5 Avalanche Photodiode	23
2.6 Representative autocorrelation plots of Alexa labeled albumin in normal cartilage and chemically digested matrix	25
2.7 Electrostatic screening of fluorophores and lipid interactions.....	27
2.8 Translational diffusion coefficient of labeled polymer and hydrodynamic radius R_h as a function of pH	28
3.1 Graphical representation of the dilute, semi-dilute and concentrated regimes for polymer solutions.....	38
3.2 Chemical structures for dextran polymers used in this study	40
3.3 Synthesis of polyvinylamine from the hydrolysis of polyvinylformamide	41
3.4 Molecular structures of the five probes used in this study.....	42
3.5 Characterization of AT-E synthesis	43
3.6 Cartoon depiction of a negatively charged particle diffusing in neutral (Dex), repulsive (Dex(-), and attractive (Dex(+)) dextran physically crosslinked polymer networks where polymer concentration is above c^* and semi-dilute polymer solutions	46
3.7 Representative normalized FCS autocorrelation curves for the diffusion of negatively charged ATTO 488 carboxy (At-C, -2) in varying weight volume percent solutions of (a) Dex(-), (b) Dex(+) and (c) PVAm solutions.....	49
3.8 The relative diffusivity (D/D_0) as a function of polymer concentration plotted for charged probes in neutral and charged Dextran and PVAm polymer solutions	51
3.9 Surface passivation of glass coverslips using pegylated silane	53

3.10 a) Normalized autocorrelation curves for At-E and At-B probes in 2 wt.% Dex(+) and PVAm solutions in 10 mM MES buffer b) Relative diffusivity (D/D_0) for At-E and At-B as a function of polymer concentration.....	54
3.11 Ionic strength effect on translational diffusion coefficients as determined by FCS for At-A, At-E, At-C and Al-C probe molecules in charged Dex and PVAm polymer solution.....	55
4.1 Particle mobility in mixed charged polymeric networks	61
4.2 Chemical structures of charged dextrans at neutral pH a) positively charged amino dextran (Am-Dex) b) negatively charged carboxymethyl dextran (CM-Dex)	66
4.3 Translational diffusion coefficients plotted as a function of polymer concentration plotted for charged probes in Am-Dex (circle) and CM-Dextran (triangle) polymer solutions	67
4.4 Transport properties of two negatively charged probes in mixed gel solutions	69
4.5 (A) NSA-Dex reaction scheme and (B) $^1\text{H-NMR}$ spectrum for amino dextran and succinylated products obtained for 5 %, 40 % and 65 % modifications.....	71
4.6 FTIR spectrum for amino dextran and succinylated NSA-Dex products.	73
4.7 Representative normalized FCS autocorrelation curves for (Al-C, -3) in 2 % wt polymer solutions of Am-Dex (+), CM -Dex(-) 40 % modified NSA, in 10 mM MES buffer (pH =6.4).....	74
4.8 Relative diffusivity (D/D_0) as a function of polymer concentration for Al-C(-3) probe diffusion with Am-Dex(+) and various polyampholytic NSA-DEX solutions.	75
5.1 Tau isoforms and amino acid sequence of tau 441	79
5.2 a) Phosphorylation of tau b) Stabilization of microtubules of neurons	81
5.3 Algorithm CIDER analysis of intrinsically disordered protein tau 441 showing net charge per residue sequence at neutral pH.....	83
5.4 Formation of microtubule by tau drops	84
5.5 Pathology of neurodegenerative disorder	86
5.6 Droplet solution profile.....	94
5.7 a) Plot showing the normalized autocorrelation curves for probe R110 in different tau protein environments b) Nanodrop Lite spectrophotometer absorbance (280 nm) facilitates	

for the measurement of protein concentration of tau before and after liquid demixing process.....	97
5.8 Schematic illustration showing molecular chain interactions in semi-dilute regime of tau condensates	99
5.9 Molecular structures of the four probes used in this study	100
5.10 a) Representative plots of normalized FCS autocorrelation of probe molecules of varying net charge in tau protein condensates. b) Comparative apparent diffusion coefficients D determined from FCS for various controls and condensates in understanding the reduced transport within condensates.	101
5.11 Normalized micro viscosity (η/η_0) using Stokes Einstein equation.....	104
5.12 a) Represents the autocorrelation plots for the protein albumin bovine serum BSA, Alexa fluor 488 conjugates ($R_h \sim 3.4$ nm) with net negative charges of (-13) in buffer system of 25 mM HEPES 150 mM KCl, tau protein solution, 10% dex as controls and condensate system. b) Comparative apparent diffusion coefficients D of probe BSA determined from FCS for various controls and condensates	106
5.13 Salt effect study in tau condensates	108
5.14 Ionic strength effect on translational diffusion for At-A (0) through Al-C (-3) and labelled BSA probe molecules in tau protein condensate solution.....	110

Chapter 1: Introduction

The exchange of molecules between various organelles or cell compartments and their environment are vital for life. In recent years, the selective permeability of lipid bilayers, such as the cell membrane of organisms, is relatively well understood.^{1, 2} Frequently overlooked, however, is that many of these bilayers are also associated with polymeric networks known as biological hydrogels. These biogels themselves serve as selective barriers to the exchange of molecules. The limited understanding of particle-biogel interactions, particularly under physiological conditions, is still a significant hurdle to the design of optimal therapeutics.⁴ Studies to understand the particle-matrix interactions represent the intersection of chemistry, biology, engineering and medicine.

1.1 Biological hydrogels

A hydrogel is a 3D network of crosslinked polymer chains that contain, absorb, and hold large quantities of water.⁶ Biological hydrogels, or biogels, consist of biologically derived polymers, such as polysaccharides or glycoproteins, where the network form entanglements due to either physical or chemical crosslinks.⁷ Chemically crosslinked gels are formed by having covalent linkages between polymer chains. Physically crosslinked gels are formed through non-covalent interactions between polymer chains including ionic bonds, hydrogen bonding or hydrophobic forces.⁸ Biogels are typically only a few percent by weight polymer, with 90-99% consisting of water.⁹ Depending on composition, biogels can cover a range of material properties from soft, elastic to highly viscous networks.¹⁰

Biogels are found in almost all domains of life from prokaryotes to eukaryotes. Prokaryotes, like archaea and bacteria, develop biofilms made up of a collection of surface-associated microbial cells enclosed in an extracellular polymeric substance matrix.¹¹⁻¹³ These bacterial biofilms are complex networks, consisting of many types of molecules (including polysaccharides, proteins, lipids and extracellular nucleic acids) and have a composition that varies depending on bacterial strain, species, as well as, environment. Biofilm formation is an important aspect of many bacterial diseases including chronic lung infections in cystic fibrosis patients and infections due to medical device and implants. A

key role of the extracellular polymeric substances (EPS) barrier in biofilms is protection from hostile environments. The EPS barrier creates an environment inside conducive to microbe growth protecting it mechanically from shearing forces, yet also acting as a selective barrier protecting the colony against environmental and chemical stresses.¹⁴

In eukaryotes, biogels have evolved to perform many functions. For example, mucus gel is one of the largest biogels in the body and is comprised of glycopolymer polymers of mucin monomers heavily saturated with O-linked oligosaccharide units.^{15, 16} Mucus acts as the first line of defense against various pathogens and toxins entering human body.¹⁷⁻²⁰ Another important biogel is the nuclear pore complex (NPC) that form channels across the nuclear envelope and controls the passage of molecules in and out of the nucleus.²¹⁻²⁴ The NPC is comprised of a family of intrinsically disordered proteins known as nucleoporins.²² Nucleoporins have short hydrophobic repeats, known as FG repeats, which are thought to serve as crosslinkers in the NPC matrix.²⁵⁻²⁷

Intrinsically disordered proteins (IDPs), like nucleoporin, are ubiquitous in nature.^{2, 21, 28} In recent years, it has been observed that many IDPs are able to undergo liquid-liquid phase separation (LLPS) *in vivo* to form membraneless organelles.^{29, 30} Examples include nucleoli, centrosomes, stress granules, Cajal bodies, and P-granules, all of which perform their own various biological functions.³¹ *In vitro* studies have shown many IDPs are able to undergo LLPS, both in the absence or presence of nucleic acids, resulting in the formation of protein-rich spherical liquid droplets. Despite growing evidence of their formation, their function and biological significance *in vivo* is still limited.³² LLPS has been proposed as a means to efficiently organize cellular processes *in vivo*. LLPS allows the reversible formation of distinct, membraneless compartments within the complex, heterogeneous environment inside a cell. These membraneless compartments could facilitate the concentration of a specific set of molecules required for particular cellular processes and minimize interference from other cellular components.³³

1.2 Permeability of biogels

One of the main physiological roles of biogels is its selective permeability controlling the transport of molecules between different compartments. However, how these selective barriers permit passage of some biomolecules while rejecting others is not fully understood. This creates a significant challenge for the design of drug delivery systems. For example, biofilms formed by *Pseudomonas aeruginosa* are known to be associated with infection on wounds and medical implants, as well as forming microbial communities in lung disease like cystic fibrosis. These bacteria have adapted different resistance mechanisms within their biofilms.³⁴ This includes specific binding of antibiotics, such as ciprofloxacin, to extracellular polymers within the biofilm network as well as hindered particle penetration resulting in sublethal concentrations of therapeutics accumulating inside the biofilm. Meanwhile the biofilms can also facilitate a corresponding increase in the diffusion of nutrients and oxygen promoting bacterial growth.³⁴⁻³⁶ Similarly, mucus gel, which lines all wet epithelia inside the body, limits permeability of certain molecules and drugs.³⁷ Mucus is therefore a critical barrier to overcome for the successful mucosal administration of particles designed for inhaled, oral or vaginal delivery of drugs. Successful delivery of these drugs will depend on the ability of the nanoparticles to reach their target cells underneath the mucus. That success will be dependent on the pharmacokinetic properties of these drug delivery nanoparticles; including both the diffusive penetration of the nanoparticles within the mucus as well as the ability to avoid mucus layer turnover.^{38, 39} In both mucus and biofilms, the permeability of a wide variety of small molecules (nutrients, metal ions, toxins, etc.) depends on the properties of the biogels. Selective transport of molecules is also a primary function for nucleoporin proteins that form a network within the nuclear pore complex. The NPC permits ions and small molecules with a radius ≤ 2.6 nm through by passive diffusion while larger cargos are transported actively using specific receptors.^{40, 41} Similarly, proteins undergoing liquid-liquid phase separation are thought to use LLPS to tune biochemical processes by acting as a selective filter. One such example is in nuclear ribonucleoprotein (RNP) granules, where di-snRNP complex cannot leave the droplet while U4/U6/U5 tri-snRNP complex can, allowing selective accumulation of a reactant in the confined space of the liquid-protein droplet.⁴²

1.3 Composition of biogels

Biological hydrogels, or biogels, are ubiquitous in nature and serve several functions. Biogels are important for structural support and mechanical function, such as lubricating surfaces of biological tissues.⁴³ As discussed above, biogels also serve the important role of being a selective barrier allowing for permeation of vital nutrients and other molecules while impeding diffusion of certain harmful substances.¹⁰ To accomplish these varied functions, biogels have complex and diverse structures dependent on their purpose. For example, mucus may contain 90-95% water but the remaining components include proteins, lipids, and electrolytes.⁴⁴ In humans, a family of secreted proteins known as mucins are the main gel-forming component of mucus. These mucins themselves are complex glycoproteins with hydrophilic and hydrophobic domains as well as charged, mostly anionic domains, due to glycosylation.^{45, 46} The exact composition of mucus also varies depending on disease state, such as the thick, sticky, dehydrated mucus with concentrated mucins that is responsible for respiratory problems for cystic fibrosis patients.⁴⁷ Due to their complex composition, the particle-mucus gel interactions in vivo are likely to involve a variety of specific and nonspecific interactions including electrostatics and hydrophobic interactions. Bacterial biofilms are also multicomponent with their composition varying widely depending on the strain, species and environment.¹² One of the best studied biofilms are formed by *Pseudomonas aeruginosa*, discussed in section 1.2. *Pseudomonas aeruginosa* is a rod-shaped bacterium known to be a major cause of healthcare associated infections. Even in this one bacterial species, anionic, cationic and neutral polysaccharides are produced to form its biofilm.^{48, 49, 50} Varying the EPS composition of bacterial biofilms greatly alters their chemical and physical properties including their adhesive properties.⁵¹ For our studies, we have chosen a simpler model system of uncharged or charged, water-soluble polymer networks, including the polysaccharide dextran and polyvinylamine. These systems are not only useful models for understanding particle transport in mucus or biofilms, but for understanding how particles diffuse inside polysaccharide networks which are currently used as vehicles for gene and drug delivery. In chapter three, we systematically investigate the effect of net probe charge

on the transport properties inside these model polymer systems both in the concentrated and semi-dilute regimes. In chapter four, we switch to amino-dextran polymers to investigate charge-charge interactions and their role on the diffusive behavior of particles in both pure charged systems and mixed cationic/anionic charged systems.

Nature also uses many other biogels, which have widely varied compositions of proteins, yet still share a common function of selective filtration. The nuclear pore complex (NPC) is a selective filter controlling the transport of molecules between the nucleus and cytoplasm. The NPC composition includes at least 30 distinct proteins. Key to the central channel are intrinsically disordered proteins (IDPs) called nucleoporins. Nucleoporins contain many phenylalanine-glycine (FG) domains believed to interact with hydrophobic amino acids to form a network structure. How the NPC controls selective transport is still not well understood. For example, it has been shown that hydrophobic interactions with FG domains is important for particle transport through the NPC, but unexpectedly, so is charge.⁵² Another protein-rich network is formed by liquid-liquid phase separation (LLPS) which enables dynamic compartmentalization of molecules in a protein-rich phase without the use of lipid membranes. Typically, LLPS is observed for IDPs or proteins with intrinsically disordered regions. By LLPS, these proteins form membraneless organelles. *In vivo*, these liquid-like droplets are presumed to have a complex composition that includes not only the concentrated protein of interest but also other biomacromolecules including other proteins or nucleic acids. While not known, one function of these protein droplets *in vivo* is also thought to be related to selective transport allowing for the concentration and recruitment of certain molecules to enable certain biological functions.⁴² For example, prion like domains of transcription factors (TFs) undergo LLPS helping with the recruitment of RNA polymerase II,^{53, 54} or recently phase-separated droplets of TFs formed in the presence of mediator coactivator have been shown to be involved in gene activation.⁵⁵ Other protein droplets, such as HP1 α , formed by LLPS have been suggested to have a role in driving heterochromatin domain formation.^{56, 57} Biomolecular interactions between the disordered protein regions in these proteins dictate the thermodynamic driving forces for condensate formation by LLPS.⁵⁸ As the composition of condensates is varied, their partition coefficient changes in a manner that determine the phase separated thermodynamic free energies manifesting in selective transport. As the composition of

condensates is varied, their partition coefficient changes in a manner that determines the phase separated thermodynamic free energies. The variation partition coefficients dictate the formation and composition of the LLPS droplet. For example, in a hub of RNA processing condensate nucleolus, there is a selective exclusion of ribonucleoprotein complex generating a non-equilibrium steady flux state. This flux drives RNA out of the nucleolus.^{59, 60} In Chapter 5, we investigate particle-protein network interactions in liquid-like droplets formed from tau protein using both a series of probe molecules, with similar size and core chemistry but varying net molecular charge, as well as a fluorescently labeled bovine serum albumin protein molecule.

1.4 Filtration strategies

1.4.1 Size filtering

Any polymeric network can be described by a characteristic length inside the polymer gels known as the mesh size. The mesh size is determined based on the entanglement of physically or chemically crosslinked polymer chains and is characteristic of the average distance between crosslinks. The relationship between the particle size to the gel mesh size determines the transport properties of particles within a polymeric network (**Figure 1.1**). These steric interactions are simple to understand assuming particles that do not interact significantly with the polymer chains of the network. When the particle size is small relative to the mesh size, the particles diffuse freely in the interstitial fluid between polymer chains. We will describe in Chapter 3, these particles experience a local microviscosity environment that can be used to understand their diffusive properties (**Figure 1.1a**) within the context of Stokes-Einstein diffusion. When the particle size is large, relative to the network mesh size, the particle will become ensnared and trapped within the network (**Figure 1.1c**). For particles on the order of the mesh size (**Figure 1.1b**), the transport is hindered but not halted. Steric interactions play a role in particle transport in biogels. The mesh size/correlation lengths of mucus and biofilms are typically in the range of 10-1000 nm while nucleoporins are reported to be in the range of $\sim 2.5-5$ nm.^{10, 61-65} Due to these small mesh sizes, nucleoporins exclude proteins larger than 30-100 kDa unless transport is guided by using nuclear transport receptor (NTR).^{66, 67} Also, in mucociliary clearance,

mucus blocks large pollutants by steric interactions allowing for the clearing of the invading particle before its entry to epithelium.¹⁹ Steric interactions alone, however, are not a sensitive means to selectively filter particles as they only depend on the particle size. The selective transport in biogels therefore must also incorporate other chemical interactions to control what molecules permeate the biogels.

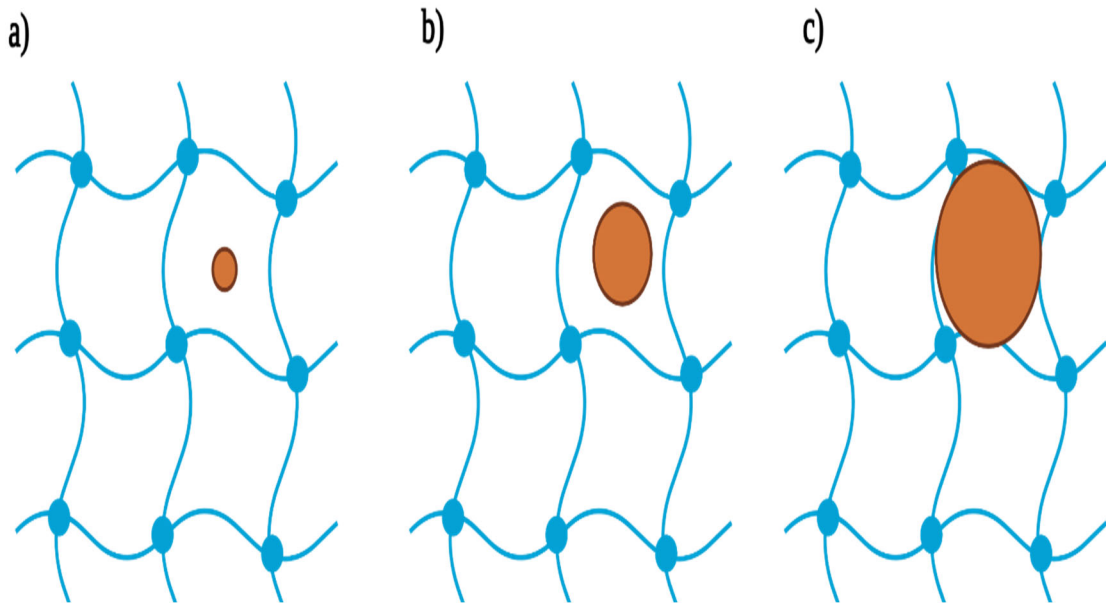


Figure 1.1 Steric effects on particle transport in polymeric gels of a given mesh size. (a) when particles are small, relative to the mesh size, they diffuse freely inside the hydrogel interstitial fluid. (b) Particles which are nearly on the same order of mesh size experience steric effects and get obstructed but pass through the hydrogel eventually. (c) Particles much larger than mesh size are trapped inside the hydrogel.

1.4.2 Interaction filtering

A major function of biogels is selective filtration of particles. Particle-biogel interactions *in vivo* must include other specific and nonspecific interactions, such as electrostatics, or hydrophobic interactions to facilitate the selective filtering of particles (**Figure 1.2**). This selection process in biogels is referred to as interaction filtering. Interaction filtering enables biogels to allow some particles to permeate the network while others are kept out that is not solely dependent on the ratio of particle size to network mesh size. These nonsteric interactions, such as electrostatic interactions between particle and polymer chains, can be attractive or repulsive in nature. Experiments have shown that electrostatic interactions are important for mobility of charged particles in mucus,^{61, 68} the extracellular matrix,⁶⁹ biofilms⁶⁴ and the nuclear pore complex.^{25, 70} Depending on the specific context, it could be advantageous to make particles that more readily permeate the biogels (for instance mucus penetrating particles to deliver drugs to the epithelial cells under the mucus) or particles with engineered reduced transport within the biogels, such as mucoadhesive drug delivery systems, that would enable longer drug action within the mucus matrix. Understanding how biogels regulate particle transport within their networks by interaction filtering is therefore critically important for a wide range of therapeutic applications. Using model polymer solutions and hydrogels allows for the examination of particular interactions, like electrostatics, within a less complex network environment to gain insight on interaction filtering mechanisms in biogels.

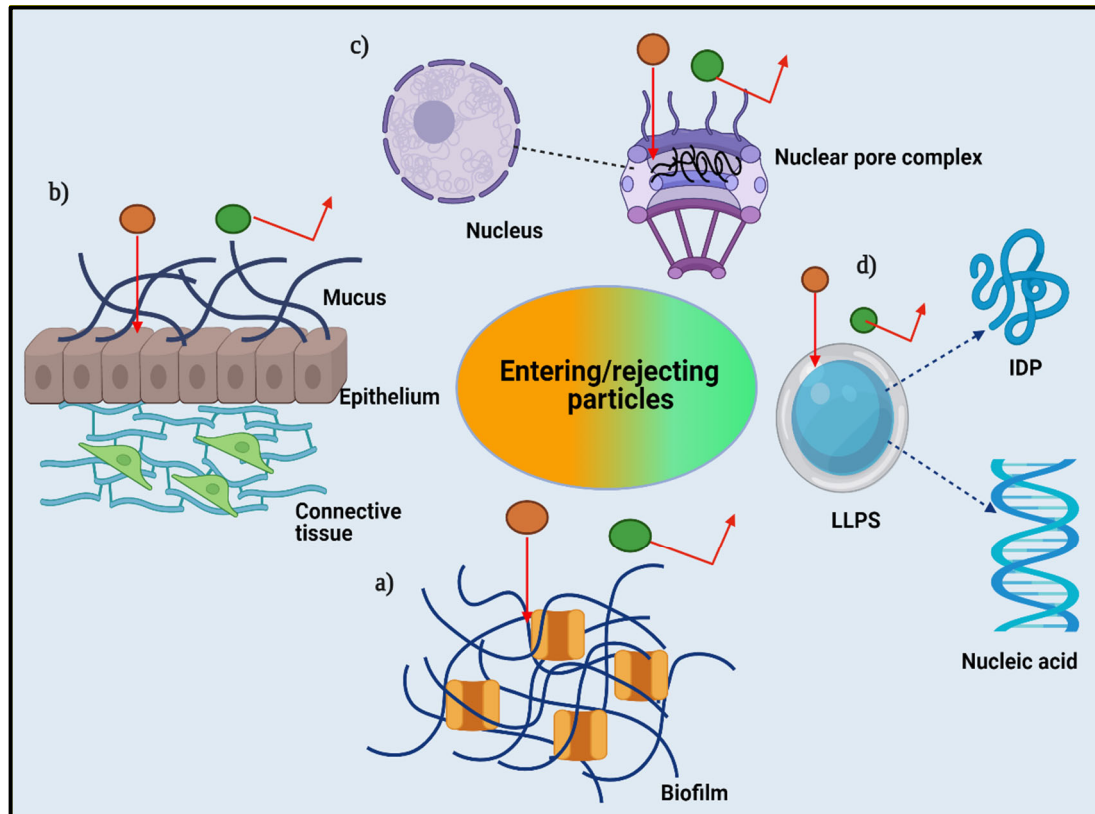


Figure 1.2 Biopolymer based hydrogels acting as selective permeable barriers for microscopic particle translocation. They permit the passage of certain particles while exclude others (a) Bacterial biofilms have secreted extracellular polymeric substances around it, to protect bacteria from entry of antibiotics. (b) Mucus lines all the wet surfaces of the body, protects from entry of pathogens and toxins. Connective tissue or extracellular matrix, a proteoglycan controls the entry of particles between cells. (c) Nuclear pore complex imports and exports particles from nucleus to cytoplasm. (d) Membraneless organelles are thought to act as selective filters to carry out biochemical reactions.

1.4.2.1 Regulation of particle diffusion in saccharide-based hydrogels

Mucins consists of a protein core glycosylated with complex oligosaccharide structures.^{71,72} Cervical mucus has large mesh size (~300-400 nm) yet particles like herpes simplex virus, that is less than 200 nm, are strongly trapped inside the cervical mucus network. Using charged polymeric nanoparticles (diameters ~100-300 nm), diffusion in intestinal mucus was shown by multiple particle tracking to be hindered for both positively and negatively charged particles, while particles with a charge near-neutral can more readily permeate the network.⁷³ These results suggest it is the charge magnitude, not the sign, of the charge, that is the key determinate for particle transport within biogels. These are just a few examples of the importance of interaction filtering in polysaccharide-based biogels.^{63,74,75} Particle transport in mucus is also known to be dependent on pH.^{61,76} For example, in acidic cervicovaginal mucus, negatively charged human immunodeficiency viruses are trapped but are not hindered in the same mucus at neutral pH.^{61,76} This behavior is also seen in reconstituted mucin gels where mobility of charged particles are suppressed at low pH but at neutral pH, both neutral and charged particles diffuse freely. Within the reconstituted mucus, the trapped particles at low pH are released on addition of high salt concentrations⁶¹ or heparin.⁷⁷ This behavior can be understood by considering electrostatic interactions. The linked sugar moieties and protonation levels of amino acids develop charge states on the polymer, sensitive to the pH which in turn controls the transport of particles based on the surface charge. The sensitivity of the mucus polymer to pH is utilized by the human body in maintaining neutral pH during ovulation whereas cervical mucus at acidic pH is neutralized by seminal fluid for penetration of sperm cells.^{78,79}

Further examples of interaction filtering in saccharide-based biogels are found in extracellular matrix and bacterial biofilms.⁸⁰ The extracellular matrix, a collection of different proteins and proteoglycan polymers demonstrate that the permeability barrier is in control of glycosaminoglycan heparan sulfate.^{81,82} The interactions of heparan sulfate chains, which carry net negative charge, are electrostatic in nature allowing binding of growth factors such as fibroblast.⁸³ It has been also shown the binding interactions depends on the charge density on the heparan sulfate which in turn set up degree of sulfation.⁸⁴⁻⁸⁷ Similar electrostatic filtration is observed in biofilms where the diffusion of charged

molecules are less than large neutral molecules.^{88, 89} This effect is attributed to negatively charged exopolysaccharides, such as alginate, which can interact electrostatically with positively charged antibiotics aminoglycosides, hindering penetration into biofilms.^{90, 91} To gain insight in charge-charge interactions within these saccharide biogels, we have chosen model branched polysaccharides called dextrans for our studies in Chapter 3. These dextrans can be obtained as uncharged polymers or in cationic (Diethylaminoethyl (DEAE)-dextran) and anionic (Carboxymethyl (CM)-dextran) variations. DEAE-dextran consists of unreactive tertiary and quaternary amines, so in Chapter 4, we switched to amino-dextrans which are dextrans functionalized with primary amines. Using amino-dextran and CM-dextran, we studied mixed cationic/anionic hydrogels comprised of different ratios of the two charged polymers. By functionalization of the primary amines on amino-dextran, we then compared the transport of probe molecules in a polyampholytic system compared to the mixed charge polymer solutions.

1.4.2.2 Regulation of particle diffusion in protein-based hydrogels

The selective barrier within the nuclear pore complex (NPC) is mainly due to nucleoporins which contain phenylalanine-rich repeats (FG-repeats) separated by hydrophilic spacer regions.^{92, 93} It was observed that some proteins, like histones or ribosomal proteins, possess small size (~15-21 kDa) yet could not pass through the nuclear pore whereas larger size transport receptors of size ~ 90-200 kDa could translocate.⁹⁴⁻⁹⁶ This paradox suggests that size filtering mechanism cannot explain the transport behavior in nuclear pore complex.⁹⁷ While hydrophobic interactions between particle and FG repeat was thought crucial for translocation of molecules through the NPC, a closer inspection also revealed the presence of electrostatic interactions that contribute to NPC selectivity. The unfolded domains that separate FG-repeats consists of polymers carrying net positive charge groups that can translocate negatively charged molecules.²⁵ In the previous example, illustrated histones cannot diffuse through the pore channel despite its relatively small size. But binding of histones to transport receptors such as importin β and importin 7, a net negative charge can be acquired by histones and becomes competent for translocation process.⁹⁶ Therefore, the positively charged sections of the polymers contribute to electrostatic

sieving which helps the NPC control particle entry based on the particle surface charge. However, other mechanistic models of nuclear translocation process also demonstrate the contribution of hydrophobic and entropic effects for particle translocation.^{98, 99} Proteins that bind to soluble nuclear transport receptors, like importin β , account for a majority of particle nuclear transport through the NPC. Nucleoporins are characterized by short hydrophobic residues FXFG, GLFG separated by hydrophilic spaces. The translocating particles with hydrophobic groups can attract towards Phe-rich clusters of nucleoporins and partition selectively into the permeability barriers.^{98, 100, 101} It is also believed that the FG domains constitute a special group of intrinsically disordered regions and can undergo phase separation to form membraneless organelle. The best studied condensate is P-granule found in *Caenorhabditis elegans* embryos which has numerous FG-dipeptides repeats suggesting its phase separation from nucleoporins.^{22, 102-104}

Like the protein-rich NPC, membraneless organelles are also recognized to recruit molecules into them selectively. Condensates are concentration hubs where they act as biochemically selective barriers for particle entry, as they enrich for specific proteins while excluding others.¹⁰⁵ For example, centrosomes form membrane less organelles that recruit specific microtubule protein tubulin for nucleation.¹⁰⁶ This biomolecular filtration mechanism is also reported for reconstituted membraneless organelles made in similar fashion and appearance to nucleolus using Ddx4 protein which exclude chromatin but absorb single stranded DNA (ssDNA) molecules. This selectivity for absorbing molecules within organelles is believed to involve the interactions of the absorbed molecules with the interior of the organelle via cation- π interactions for nucleic acids and by electrostatics of the charged protein chains that forms the membraneless organelles.^{107, 108}

1.5 Charge-Charge interactions in model hydrogels

Considering the importance of interaction filtering, the DeRouchey lab has focused on the study of probe-polymer charge interactions using dextrans as a model saccharide-based hydrogel. Using high molecular weight dextran at sufficiently high polymer concentration, above the critical overlap concentration, physically crosslinked hydrogel solutions can be formed. In previous work, the transport properties of a single probe (net charge -2) was

examined by fluorescence correlation spectroscopy (FCS) in neutral and charged dextrans [CM-dextran (-) and DEAE-dextran (+)]. We showed that probe transport in the charged hydrogels was highly asymmetric, with diffusion significantly hindered by attractive electrostatic interactions compared to repulsion and that the filtering capability of the dextran solutions was sensitive to the solution ionic strength.¹⁰⁹ In collaboration with the Roland Netz lab (Freie Universität Berlin, Germany), a simple network model was developed for Brownian dynamic simulations. The simulations, in quantitative agreement with our experiments, revealed the charge asymmetry arose due to particle sticking at the vertices of the attractive (oppositely charged) polymer gel.¹¹⁰ In my work, we extended this experimental approach to examine the role of particle net charge, and the charge density of the network, on transport properties of probe molecules (chapter 3). Using FCS, we determined the translation diffusion coefficient of a series of probe molecule, with similar size and core chemistry but varying net molecular charge in neutral and charged dextran solutions. In this study, we looked at both low and high molecular weight dextrans resulting in polymer solutions in the semi-dilute or concentrated regime, respectively. Transport of our probe molecules in the semi-dilute and concentrated regimes showed similar diffusional behavior as the particle was small relative to the corresponding polymer length scales. As anticipated, high particle charge resulted in more hindered diffusion in the attractive dextran solutions and this particle transport was dependent on solution ionic strength. Using a biotinylated probe, we were also able to observe the effect of additional non-electrostatic interactions between probe and the dextran networks.

Using the developed network model, and appreciating the complex composition of biogels, we also previously worked with the Netz lab to do a quantitative comparison between experimental data on a single probe molecule inside mixed cationic/anionic dextran gels and a coarse-grained simulation model for particle transport inside gels with a random distribution of interaction sites.¹¹¹ Both experiment and simulation showed that particle transport in mixed gels was nearly identical to purely attractive gels, over a broad range of compositions, despite the reduced number of attractive interaction sites. This is due to the magnitude of the attractive interaction being large compared to weak repulsive electrostatic interactions inside the gel network. By simulation, the particle trapping in mixed gels is similar to purely attractive interactions and dominated by vertex trapping. Taken together

this work illustrates why heterogeneous biogels can serve as highly effective and robust selective filters for interacting particles. As most biogels have compositions consisting of biopolymers with attractive and repulsive domains along the same polymer chain, my research focused on the creation of polyampholytic polymeric networks for comparison to mixed charged hydrogel networks (chapter 4). By functionalization of the primary amines of an amino-dextran, polyampholytes with varying amounts of cationic/anionic functionalization were synthesized and characterized. Particle transport of probes of varying charge was compared in these polyampholytic polymer solutions to transport in mixed charged dextran solutions of amino-dex (+) and CM-dex (-). Due to the high molecular weight of the dextrans, all polymer concentrations explored were above the critical overlap concentration and in the concentrated polymer solution regime. Interestingly, in the polyampholytic dextran solution, the strong electrostatic attractions between probe and polymer chain are lost faster than with the mixed dextran solutions. For example, 40% succinylation of the primary amines in the polyampholyte is sufficient to no longer observe hindered transport due to the attractive electrostatic interactions. In the mixed polymer solutions, even 20% amino-dex (+) in a matrix of CM-dex (-) was still sufficient to hinder the probe particle transport. This could be rationalized from the particle studies in ECM, where local charge distribution of different charges on polymeric network is shown to be important in trapping the particles within biopolymers.⁶⁹

1.6 Dissertation outline

This dissertation outlines progress on understanding electrostatic interactions and their role on particle transport within model polymer networks. Chapter 2 of this dissertation provides a description of the principles of fluorescence correlation spectroscopy and summarizes prior work on using FCS for analyzing translational diffusion coefficients of fluorescently labeled molecules in polymer solutions and networks.

In chapter 3, I focus on a series of probe molecules, with similar size/chemistry, but different net molecule charge. Using FCS, the particle transport properties were determined in both neutral and charged dextran solutions in both the semidilute and concentrated regimes. We show how increasing the probe molecule charge leads to increased attractive

interactions in attractive polymer solutions and more hindered diffusion. This particle filtering is sensitive to solution ionic strength, however, the more highly charged probes still showed hindered diffusion even at high ionic strength. The charged dextran solutions are relatively low charge density, which ~ 1 charge per 3-5 sugar repeat units. For comparison, probe transport was also examined in semidilute polymer solutions of polyvinylamine (PVAm). PVAm is a water-soluble polymer with a high linear charge density with one primary amine per monomer repeat unit. In PVAm solutions, all probe molecules were highly hindered in the PVAm solutions and had modest sensitivity to solution ionic strength.

Chapter 4 explores probe diffusion in mixed charged and polyampholytic polymer hydrogels and their dependence on probe charge. Using a new cationic dextran with primary amines suitable for functionalization, we again observe that particle transport in mixed attractive/repulsive charged polymer solutions is nearly identical to purely attractive gels over a wide range of compositions. The incorporation of negative charges onto the cationic amino-dextran chains, to form a polyampholytic network, however results in higher sensitivity to the charge composition within the polyampholytic networks. The polyampholytic dextrans show a loss of the selective particle filtering at much lower ratios of positive to negative charge moieties.

In chapter 5, we switch to a mixed charge protein-based system, specifically tau protein condensates formed by LLPS. Using the same series of probe molecules, we systematically investigated the effect of probe charge on the transport properties within tau protein condensates. Despite being protein-rich phases, the tau droplets are observed to be moderately low-density droplets comparable to semi-dilute polymer solutions. Experimentally we observe both the probe molecules and BSA are able to freely diffuse within the permeable voids between tau protein chains. I will show there are dependencies on the probe charge and ionic solution conditions on the diffusion behavior inside the tau droplets. In addition, I explore possible mechanisms that can account for the transport properties of the BSA molecule inside tau droplets. Together, these findings suggest some of the different parameters controlling the transport of particles within protein droplets that could provide insight on the design of novel membraneless organelle therapeutics.

Chapter 2: Fluorescence Correlation Spectroscopy (FCS)

2.1 Introduction

In 1972, Douglas Magde, Elliot Elson and Watt W. Webb described the theory, experimental set-up, and applications for FCS.¹¹²⁻¹¹⁴ FCS was first developed as a tool to measure chemical reaction kinetics and diffusion via fluorescence fluctuations. A significant advancement of FCS occurred in the 1990s with the introduction of a confocal configuration into FCS by Rudolf Rigler and Manfred Eigen enabling single molecule sensitivity.^{115, 116} Due to advances in strong, stable lasers and sufficiently sensitive detectors, Rigler and coworkers were able to use a confocal configuration with a high numerical aperture objective and pinholes to limit detection volume, minimize scattered light and increase signal to noise. In so doing, they showed FCS was capable of the direct detection of single fluorescently labeled molecules diffusing freely in aqueous solution.¹¹⁷ In the last couple of decades, the integration of more advanced optical approaches, such as dual-color cross-correlation and multi-photon excitation, has enabled FCS to describe multiple dynamic processes occurring in complex environments in a wide range of in vitro and in vivo systems.¹¹⁸⁻¹²²

2.2 Principle of FCS

2.2.1 Autocorrelation

To study the transport properties of nanoparticles within biopolymer solutions, we used FCS, which offers non-invasive and direct monitoring of dynamic processes of single molecules in polymeric systems, hydrogels and tissues.¹²³⁻¹²⁵ FCS is based on statistical analysis of temporal fluctuations of the fluorescence intensity (**Figure 2.1**). These fluctuations arise due to the Brownian motion of the particles in solution due to continuous collisions with other molecules in the surrounding medium. Generally, the two major results obtained from FCS studies are:^{115, 126} (1) Characteristic diffusion time, τ_d and (2)

the average number of molecules, N , present in the observation volume, known as the confocal

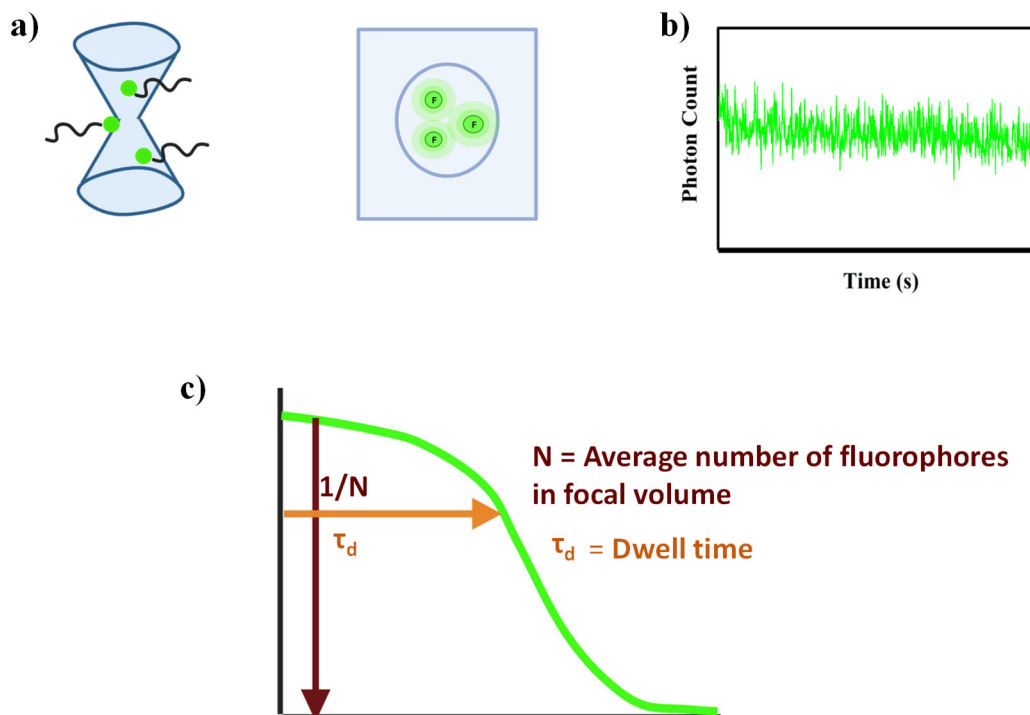


Figure 2.1 Overview of fluorescence correlation spectroscopy (FCS). (a) fluorescently labeled molecules are excited while diffusing through a defined confocal detection volume (b) by detecting the emitted photons, a fluctuating intensity trace is recorded. (c) the corresponding autocorrelation function calculated from the fluorescence intensity trace is used to obtain information about the number of molecules (N) and diffusion time (τ_d) in the observation area.

volume, in which intensity fluctuations of fluorophores are observed. Translation diffusion coefficients, D , can be determined from τ_d and the size of the confocal area which is determined by measurements of a dye with known D .¹²⁶

The intensity of fluorescence fluctuation can be calculated at a certain time using equation (1):

$$\delta I(t) = I(t) - \langle I(t) \rangle \quad (1)$$

where $I(t)$ is the intensity of fluorescence and $\langle I(t) \rangle$ is the average intensity over time. The autocorrelation curve is calculated from the intensity trace where each signal is compared to itself after a delay time τ . This autocorrelation function for FCS is expressed as:¹¹⁴

$$G(\tau) = \frac{\langle \delta I(t) \cdot \delta I(t + \tau) \rangle}{\langle I(t) \rangle^2} \quad (2)$$

where, $I(t + \tau)$ is the intensity of fluorescence after a lag time or delay time.

2.2.2 Triplet state

The autocorrelation discussed above have not considered that some of the illuminated particles may be excited to the triplet state where they don't emit any photons for a characteristic time. The triplet state concept is well explained by the Jablonski diagram (**Figure 2.2**). Under normal conditions, the fluorophore occurs in the lowest vibrational state of the lowest electronic state (S_0). Excitation of this fluorophore can be achieved by absorption of light. The absorption is proportional to the difference between the excited and ground states of the molecule.^{127, 128} According to the Born-Oppenheimer approximation, the electrons can be separated from the nucleus only when the spin is conserved. In reality, addition to the spin allowed transition there are other transitions such as singlet-triplet and triplet singlet transitions called intersystem crossing which are observed in some systems.¹²⁸ The spin allowed transitions yields fluorescence and in latter case, it leads to radiative transition called phosphorescence.¹¹⁴ Assuming these processes are well separated in the time domain, the full autocorrelation function for identical fluorescent particles undergoing ideal Browning diffusion can then be written as:¹²⁸

$$G(\tau) = \frac{1}{N} \left(1 + \frac{\tau}{\tau_D}\right)^{-1} \left(1 + \frac{1}{\left(\frac{r_0}{z_0}\right)^2 \tau_D}\right)^{\frac{1}{2}} \left(1 + \frac{\exp\left(-\frac{\tau}{\tau_t}\right)}{1-T}\right) \quad (3)$$

where N denotes the number of particles within the confocal volume, τ_d is the diffusion time of the particle of interest, and $\left(\frac{r_0}{z_0}\right)$ is the ratio of the axial and radial dimensions of the confocal volume. The triplet times are characterized by a characteristic flickering time (τ_t) and the dark fraction T .

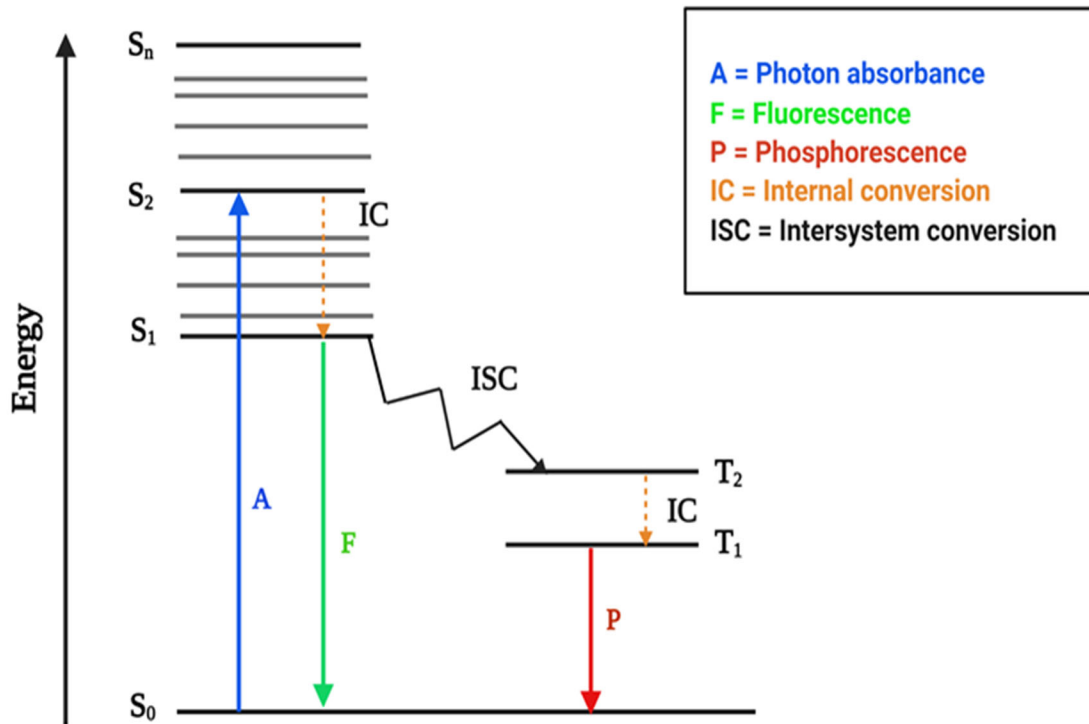


Figure 2.2 Jablonski diagram showing possible radiative process of absorption, emission by solid arrows and non-radiative transitions by dashed arrows.

2.3 FCS experimental set up:

A common experimental set-up used for FCS is depicted in **Figure 2.3**. The excitation radiation, often a continuous-wave laser, is directed by a dichroic mirror into a microscope objective and focused on the sample. A water immersion objective is used for measurements.

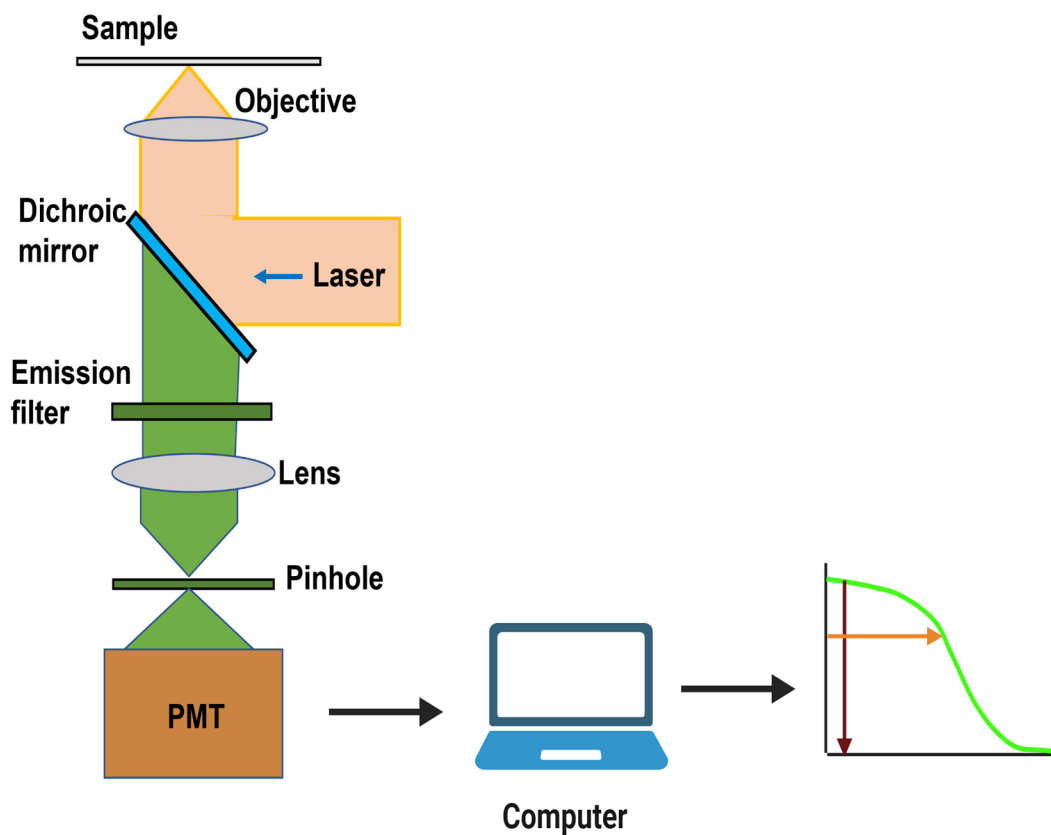


Figure 2.3 Schematic representation of experimental FCS set up. The incident light from laser source to reemitted fluorescent photons reaching detector pathway are shown.

Emitted fluorescence light from the sample is collected by the same microscope objective and passed through the dichroic and an additional emission filter. A pinhole is used in the image plane to attenuate any fluorescence light not originating from the focal region.¹²⁴ As depicted in Figure 2.3, after passing through the pinhole, the light is then focused onto a detector with single photon sensitivity, often a photomultiplier tube (PMT) or avalanche photodiode (APD). The output from the detector is then time autocorrelated using a hardware correlation card.¹²⁴ In my work, all FCS experiments were made using a commercial ISS Alba confocal fluorescence fluctuation system coupled to a Nikon Ti-U microscope equipped with a 60×/1.2 NA water-immersion objective lens. The emission signals were passed through a 514-nm long-pass edge filter before detection. Emission signals are recorded by two separate PMTs.

2.3.1 Detectors in FCS

As FCS measures fluctuations arising from single molecules entering or leaving the confocal volume, detectors capable of measuring single photons are required. The most common detectors for FCS are therefore photomultiplier tubes (PMTs) and avalanche photodiodes (APDs). Both detectors amplify the original signal of photons by using either the photoelectric effect or using avalanche breakdown, respectively, and are sensitive enough to detect single photons of light.

As shown in **Figure 2.4**, PMTs are vacuum tubes where light enters and is absorbed by a photocathode. The absorption of the light excites electrons in the photocathode resulting in the emission of electrons due to the photoelectric effect. These emitted electrons are accelerated and focused onto a series of dynodes resulting in a multiplication effect due to secondary electron emission at each dynode. This produces a cascade of electrons within the PMT amplifying the original signal by as much as 10^8 . Lastly, the multiplied secondary electrons are collected at the anode resulting in an electrical current output to an external circuit.¹²⁹

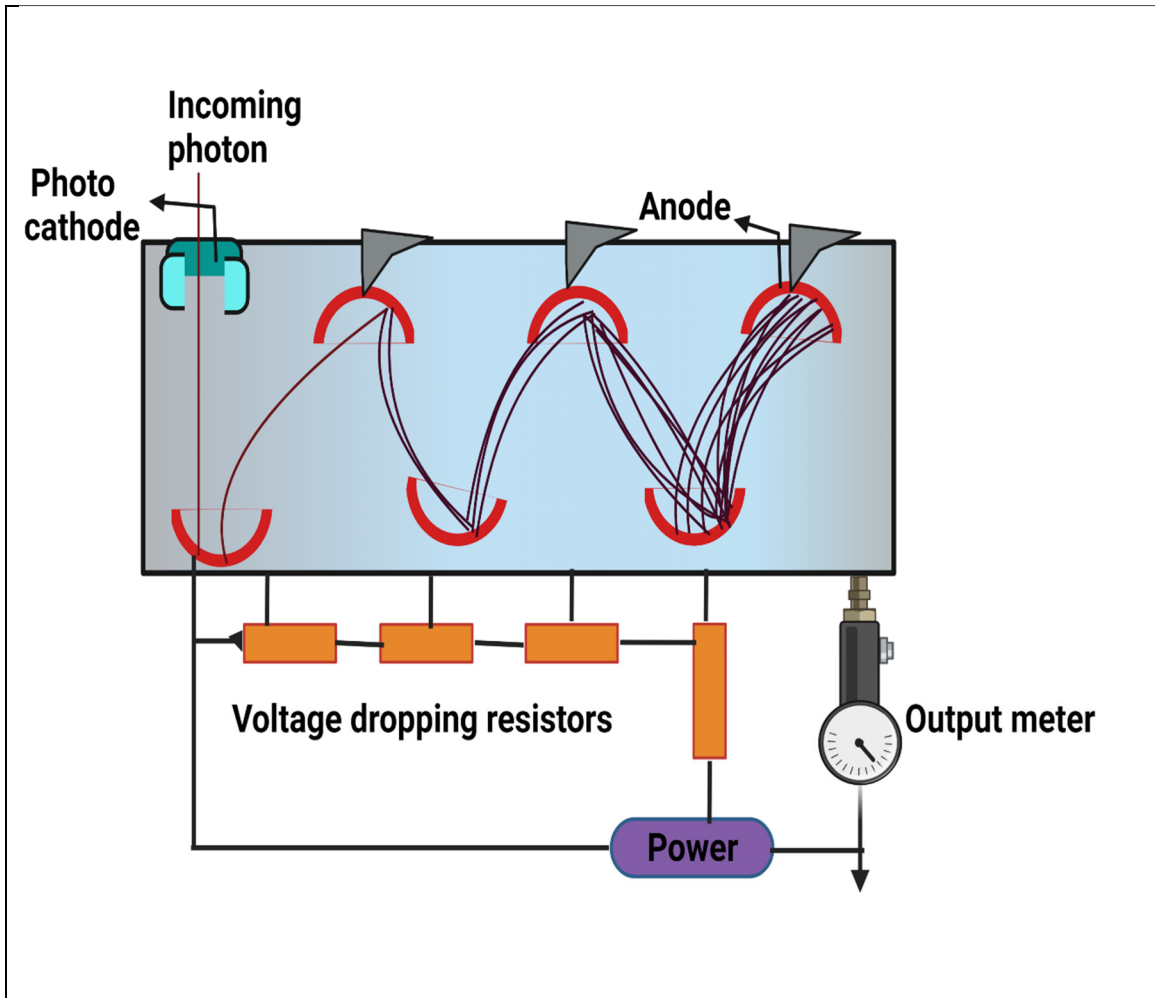


Figure 2.4 Photomultiplier tube used for photon detection in our FCS. Represents components of photodetector multiplier tube to process output by converting photon of light to electrical signal.

Avalanche photodiodes (APDs) (**Figure 2.5**) are also commonly used for low light detection in FCS. An APD is a semiconductor photodiode containing positively doped P region and a negatively doped n region operated at a high reverse voltage. Within a depletion region, absorbed photons generate electron-hole pairs that in turn generate an electrical current. The initial electron-hole pairs are accelerated within a strong internal electric field resulting in the generation of secondary carriers. This results in an "avalanche" of electron-hole pairs which is used to amplify the original signal.¹³⁰ A couple advantages of APDs over PMTs is their small size and large capacitance.

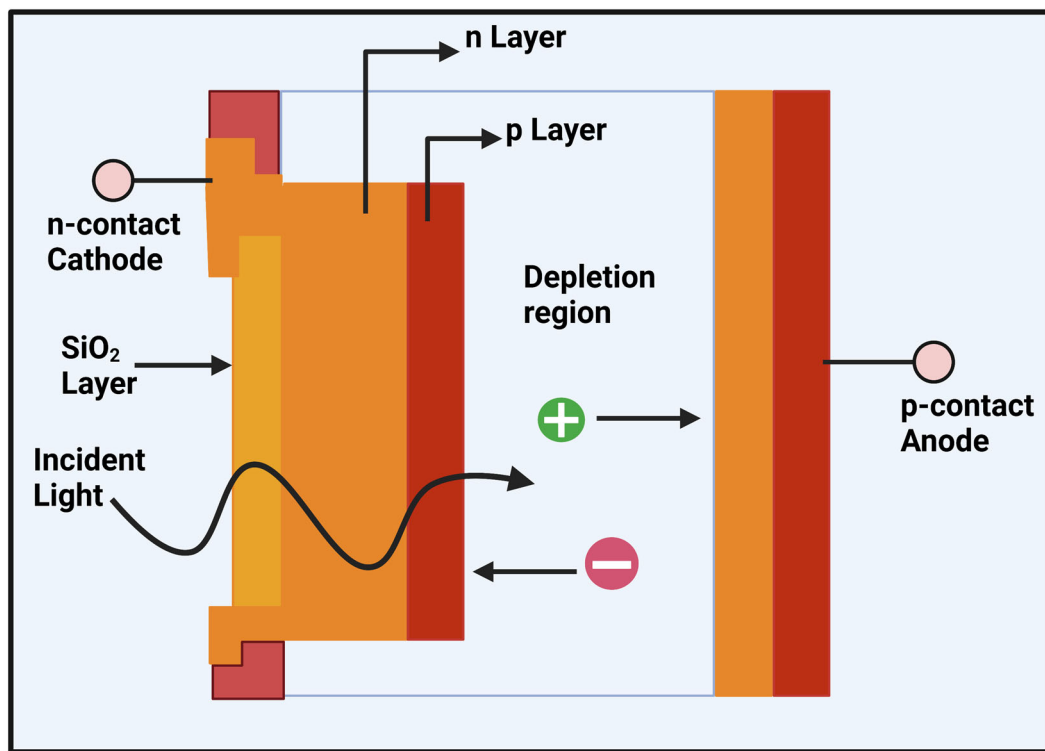


Figure 2.5 Avalanche Photodiode.

2.4 Applications of FCS in polymers

2.4.1 Translational diffusion coefficient and concentration measurements

FCS allows for direct measurement of diffusion properties of molecules diffusing in biomolecular environments. The diffusion of molecules inside polymer solutions and gels is mainly determined by the size of the diffusing particle, the relevant polymer correlation lengths, and interactions between diffusing particle and polymer network.¹²⁵ For example, the complexation of negatively charged rhodamine labeled oligonucleotides with cationic polymers was previously studied using FCS.¹³¹ It is also possible to measure concentrations of fluorescent molecules for more than one species diffusing at different rates. The interaction of cationic Rh6G dye molecules with anionic polystyrene sulfonate polymers results in a fraction of polymer-bound dye and a fraction of free molecules. At higher ionic solution strength, the fraction of bound dye decreases indicating an exchange process between free and bound cationic probe molecules.¹³² The parameters of molecular dynamics of polymer networks can also be extracted by evaluating the diffusion behavior of probes, such as commercially available Alexa dyes. Studies on probe diffusion of Alexa labeled albumin within articular cartilage, a proteoglycan (made of gluconic acid and N-acetyl glucosamine), were studied using FCS (**Figure 2.6**).¹³³ Diffusion coefficients of Alexa-albumin were determined in trypsin treated cartilage for different time periods from 3 h to 24 h (trypsin -3 to trypsin -24) to understand the molecular dynamics after chemical digestion. Increase in chemical digestion increased diffusion coefficients of labeled albumin. Early stages of trypsin digestion hinders the diffusion of labeled albumin because of changing of the natural available space of cartilage to a much more intricate environment.¹³³ These studies show how FCS provides the advantage of direct measurement of diffusion behavior of molecules within proteoglycan tissues and details about their time-related degeneration.

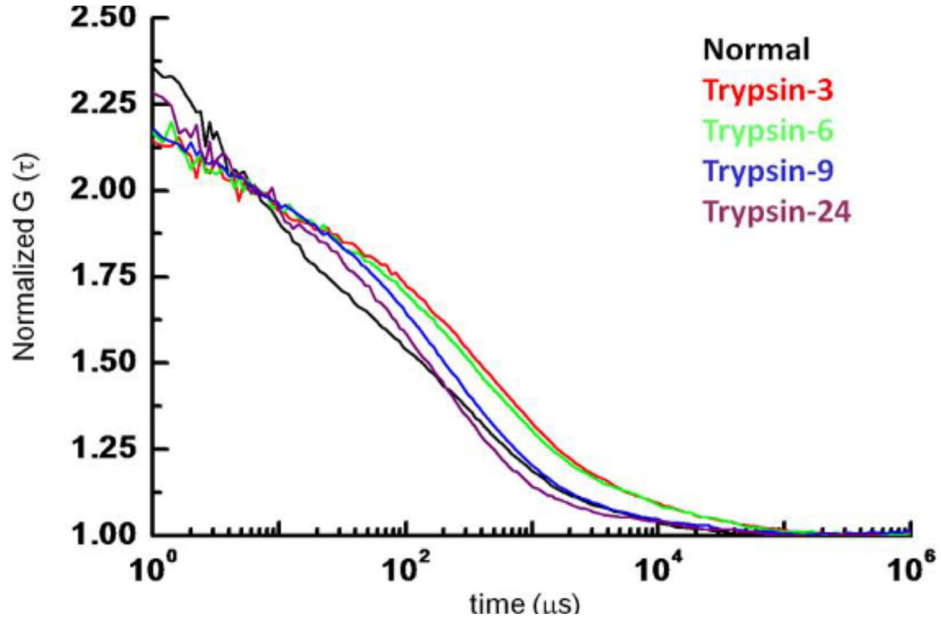


Figure 2.6 Representative autocorrelation plots of Alexa labeled albumin in normal cartilage and chemically digested matrix with Trypsin-3, Trypsin-6, Trypsin-9 and Trypsin-24. The dwell times increases for chemical digested samples with time in comparison to normal cartilage indicating more free diffusion of probe. (Reprinted with permission from Lee, J.I., Sato, M., Ushida, K. *et al. Measurement of diffusion in articular cartilage using fluorescence correlation spectroscopy*. BMC Biotechnology **11**, 19 (2011), @ copyrights ©2011 Lee et al; licensee BioMed Central Ltd)

2.4.2 Association and dissociation event studies

Measurement of binding interactions is crucial for understanding biochemical reactions that drives cellular functions.^{134, 135} For example, FCS was used to study interactions between fluorophores and lipids and to quantify the partition of fluorophores into lipid membrane by following two species FCS autocorrelation equation:¹³⁶

$$G(\tau) = \frac{1}{N_{tot}} (1 - \xi) \left(1 + \left(\frac{\tau}{\tau_{d1}}\right)\right)^{-1} \left(1 + \frac{1}{S^2} \left(\frac{\tau}{\tau_{d1}}\right)\right)^{-0.5} \left(1 + K_1 e^{\frac{-\tau}{T_{k1}}}\right) + \xi \left(1 + \left(\frac{\tau}{\tau_{d2}}\right)\right)^{-1} \left(1 + \frac{1}{S^2} \left(\frac{\tau}{\tau_{d2}}\right)\right)^{-0.5} \left(1 + K_2 e^{\frac{-\tau}{T_{k2}}}\right) \quad (4)$$

where, s is the ratio between axial and lateral ratio of detection volume, N_{tot} is the total number of molecules in detection volume, τ_{d1} , K_1 , T_{k1} are diffusion time, triplet fraction and triplet lifetime of the free fluorophore and τ_{d2} , K_2 , T_{k2} are diffusion time, triplet fraction and triplet lifetime of the bound fluorophores, respectively. Here ξ represents the fraction of bound fluorophores to the lipid vesicle. The electrostatic interactions between charged fluorophores and the cationic lipid 1,2-dioleoyl-3-trimethylammonium-propane (DOTAP) as a function of varying NaCl salt concentration was examined using FCS.¹³⁶ **Figure 2.7A** shows the autocorrelation curves for the cationic Atto 647N dye in the presence of 4 mM cationic DOTAP lipid at two different salt concentrations. Fitting the data to equation (4) shows that the lipid-bound fraction of fluorophore Atto 647N changes from 5% in 14 mM salt to $\sim 10\%$ in 140 mM NaCl resulting in a shift in the autocorrelation curve to longer decay times with increasing salt concentration. At low salt, the repulsive electrostatic interactions between the cationic, +1 charged Atto647N dye and DOTAP with a +1 charged lipid head minimizes the amount of dye binding to the lipid. At high salt, these coulombic interactions are effectively screened, and more dye is observed to interact attractively to DOTAP resulting in more dye bound at high salt. In **Figure 2.7B**, attractive electrostatic effects were observed between anionic Alexa 647 dye (-4 charge) and cationic DOTAP where increased salt concentration screens coulombic fluorophore-lipid interactions. The autocorrelation curves reveal that the characteristic diffusion time of Alexa647 decreases at high NaCl salt concentration due to a decrease in bound dye at high solution ionic strength.

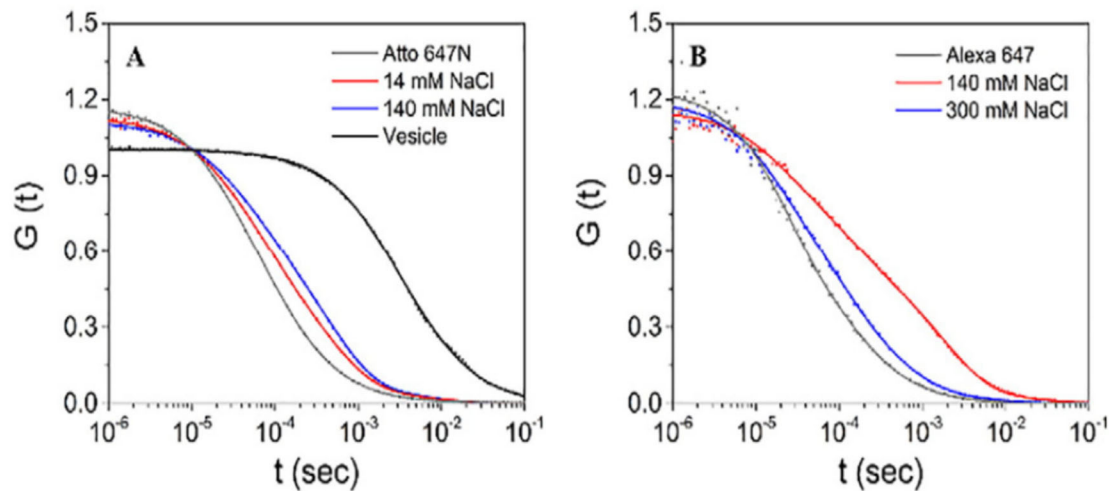


Figure 2.7 Electrostatic screening of fluorophores and lipid interactions. (A) Normalized autocorrelation curves of 1nM Atto 647N (-1 charge) and 4mM DOTAP at different salt concentrations (red and blue) using a two-species fit. For comparison, the normalized autocorrelation curve of fluorescent lipid vesicle is also shown. Longer decay shifts are observed with increasing salt concentration due to an increase in fluorophore-lipid interactions. (B) Normalized autocorrelation plots of 1nM Alexa 647 (-4 charge) and 4mM DOTAP at different salt concentrations (red and blue). The plot indicates shorter decay shifts with increasing salt concentration due to increase in repulsive forces between fluorophore-lipid interactions. (Reprinted with permission from Zhang Z, Yomo D, Gradinaru C. *Choosing the right fluorophore for single-molecule fluorescence studies in a lipid environment*. *Biochim Biophys Acta Biomembr.* 2017 Jul;1859(7) 1242-1253.)

2.5 Applications of FCS in polyelectrolytes

The properties of polyelectrolytes are mainly due to their dual character of being flexible and highly charged polymers.^{137, 138} Dynamic changes of polyelectrolyte solutions with pH, helps to measure the conformational transitions of the polymer chain. For example, the hydrodynamic radius of a fluorescently labelled poly(methacrylic acid) (PMAA) was monitored by FCS (**Figure 2.8**) to understand changes in the polymer conformation as a function of pH.¹³⁹ The effects of enhanced ionization and rise of intramolecular repulsions on expansion of labelled PMAA chains were studied. The experimentally determined value of hydrodynamic radius R_h for PMAA changes from 8.5 nm to 15 nm over a pH range of

4.5 to 9. This corresponds to a fully uncharged polymer at low pH to a highly charged polymer chain at high pH. Experiments like these show the promise of FCS to provide molecular level information about the structural dynamic changes of a polyelectrolyte polymer chain.¹³⁹ Another example of FCS being used for studies of polyelectrolyte dynamic studies was done by Kim et al.¹⁴⁰ Using fluorescently labeled dextran, they investigated the solvent-dependent uptake of a neutral polymer into polyelectrolyte multilayer microcapsules. FCS was used to determine the dextran hydrodynamic radius with a decreased R_h indicative of dextran encapsulated within the microcapsules. They showed that in water, the dextran polymer was not able to diffuse through the shells. In the presence of small amounts of ethanol or acetone, however, large nanopores were formed allowing the dextran to become encapsulated within the microcapsules.

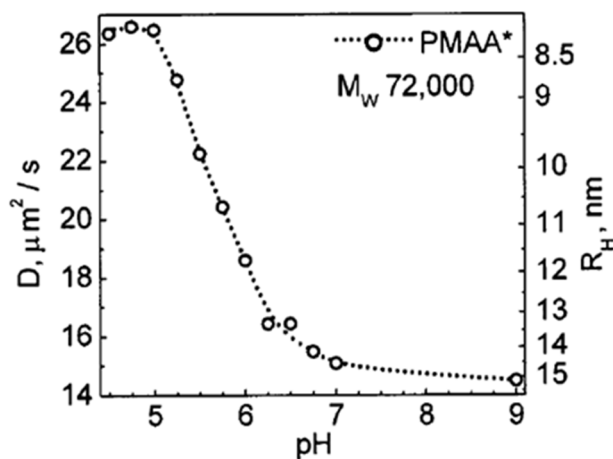


Figure 2.8 Translational diffusion coefficient of labeled polymer and hydrodynamic radius R_h as a function of pH. Change in pH from 5 to 8 results in expansion of polymer coils. (Reprinted with permission from Denis et.al; "*Fluorescence correlation spectroscopy studies of diffusion of a weak polyelectrolyte in aqueous solutions*", The Journal of Chemical Physics 122, 014907 (2005)).

2.6 Applications of FCS *in vivo*

2.6.1 Diffusion studies within cell

FCS has the potential for studying dynamic process in or on cells at the single-molecule level. Experimental studies have demonstrated that molecules exhibit anomalous sub diffusion in the cytoplasm because it contains high concentration of liquid vesicles, proteins, and organelles such a Golgi apparatus and endoplasmic reticulum (ER).^{141, 142} The cytoplasm is also crowded with many macromolecular species like RNA, ribosomes and proteins diffusing and binding to various structural elements. It was demonstrated by FCS, the sub diffusion of dextran probe molecules persisted after disruption of cytoskeleton indicating anomalous sub diffusion is not solely due to higher order structure hindrance.¹⁴³ However, the reduced particle mobility in cells appears to depend on type of cell and their location within the cell.

FCS was also employed for the study of fluorescein labeled oligodeoxynucleotides in the nucleus to measure their diffusion. It was observed that the major fraction of oligodeoxynucleotides moved rapidly, similar to diffusion rate in aqueous solution, whereas a small fraction moved slowly due to hybridization to endogenous RNA or other macromolecular complexes.¹⁴⁴ One concern for FCS experiments performed in cells is that a variety of cellular molecules, like flavoproteins and nicotinamide adenine dinucleotide (NADH), have intrinsic fluorescence.¹⁴⁵ The background signal arising from this autofluorescence depends both on the excitation wavelength and location within the cell. For example, autofluorescence is brighter in the cytoplasm and is heterogeneous and can fluctuate on the timescale of seconds. Care must be taken to reduce the autofluorescence background signal. Due to its low background, two-photon FCS is often used in cells as biomolecules in the cell are not capable of absorbing wavelengths higher than 900nm,

2.6.2 Diffusion studies on membrane

The first successful *in vivo* applications of FCS was achieved by measuring diffusion of protein in cell membrane.¹⁴⁶ Before the wide spread of FCS, most of the early studies used FRAP for studying membrane protein diffusion. But the results of FRAP experiments on

labeled proteins *in vivo* showed that the diffusion of molecules appeared to be slower than predicted by the hydrodynamic Saffman-Delbreck theory.^{147, 148} Reexamination of single-phase model in the 1990s using FCS confirmed the presence of anomalous sub diffusion on cell membranes and that this it is not an artifact of the FRAP technique.¹⁴⁹

2.6.3 Directed transport

Many biochemical processes take place in cell requires metabolites to be transported between compartments for cellular functions. FCS has been used to distinguish active transport and passive diffusion in plant biology.¹⁵⁰ Previously FRAP studies indicated that plastids in plant cells have tubular projections through which molecules are exchanged.¹⁵¹ Experiments on chloroplasts using FCS reveals that the GFP expressed in plastids moved by active transport through tubules while a free diffusion is observed through cytosol.¹⁵² If the molecular motion involves active transport, the correlation is modified as:

$$G(\tau) = G_D(\tau) \times G_{Flow}(\tau) \quad (5)$$

where $G_D(\tau)$ and $G_{Flow}(\tau)$ are calculated from equation 6 and equation 7,

$$G_D(\tau) = \frac{1}{N} \frac{1}{\left(1 + \frac{\tau}{\tau_D}\right)} \frac{1}{\left(1 + \frac{\tau}{\omega^2 \tau_D}\right)^{1/2}} \quad (6)$$

$$G_{Flow}(\tau) = \exp\left(-\left(\frac{\tau}{\tau_{Flow}}\right)^2\right) \quad (7)$$

$$V = \frac{r_0}{\tau_{Flow}} \quad (8)$$

Using this approach, τ_{Flow} and velocity (V) for active transport can be calculated for the average residence time of the molecule in the focal volume if the dimensions of the focal volume are well-defined. By this method, it was determined that diffusion in tubules is 50-100 times slower than aqueous solution and cytosol, respectively.

Chapter 3: Particle transport in semidilute polymer solutions: effect of particle charge and polymer chain charge density

3.1 Introduction

Hydrogels are commonly described as the three-dimensional network of polymer chains with ability to absorb water.^{6, 10} Biological hydrogels, or biogels, are hydrogels composed of biologically derived polymers. Biogels are ubiquitous in living systems with examples ranging from bacterial biofilms, mucus, extracellular matrix and nucleopore complex. Biogels have important physiological roles not only as structural supports but also serving as selective filters to control the passage of various biomolecules such as nutrients, proteins, ions, drugs, and acts as barrier against pathogens.¹⁵³⁻¹⁵⁵ A defining feature of synthetic filters is that rapid flux comes at the expense of high selectivity and specificity.¹⁵⁶ Biogels however can have both high specificity and flux. The selective permeability of molecules in biogels is dictated by its interactions with varied type of polysaccharide units in biofilms^{90, 91} and by proteoglycans acting mostly as polysaccharides in mucus^{157, 158} and connective tissues of extracellular matrix.^{9, 69, 81} To achieve high flux and high specificity, biogels use a variety of polymer compositions and complex interactions. For example, mucins, the primary gel-forming component of mucus in humans, are a family of secreted glycoproteins that contain hydrophobic, hydrophilic and charged domains capable of interacting with particles trapped within the mucus gel. In addition, biogels have been shown to achieve different functions by particle interactions dependent on the context. For instance, binding interactions usually lead to hindered diffusion for particles within a polymer network. This behavior is observed within mucosal membranes, where inert nanoparticles that minimize binding interactions show higher permeability.¹⁵⁹⁻¹⁶¹ But in the nuclear pore complex, proteins that bind have been shown to have a higher flux than inert proteins.^{94, 162, 163} Despite their importance for biological function, how these biogels selectively regulate particle transport within their networks is still not well understood. Alongside hydrodynamic and steric effects, nonsteric interactions, such as electrostatics and hydrophobicity must also play a major role in the diffusive behavior of particles in biogels. A more complete understanding of the filtering mechanisms of biogels is therefore

critical for both designing nanoparticles for therapeutic applications as well as the design of better synthetic filters with high flux and selectivity.

Biopolymers, such as polysaccharides, are also promising carriers for a wide range of therapeutic agents.¹⁶⁴⁻¹⁶⁷ Dextran complexed with small molecules or drugs has shown promise in the fields of drug delivery for controlled release and tissue engineering.¹⁶⁸⁻¹⁷¹ For example, cis-platinum (II) complexed with charged dextran derivative, carboxymethyl dextran (CM-Dex), is reported to be cytotoxic against human derived tumor cell lines *in vitro*.^{172, 173} Understanding particle transport within these complex biopolymer systems is also crucial for their optimization.^{25, 61} There is a growing number of studies to better elucidate the partitioning and diffusivity of small molecules in polymer-based hydrogels, but the complexity of diverse interactions like sterics, hydrophobic, electrostatic, van der Waal makes this a challenging problem.^{63, 76, 174, 175} Other factors shown to be critical for particle transport in hydrogels are charge density, particle surface charge^{9, 25, 61, 68, 174, 176} and their magnitude rather than their algebraic sign^{69, 177} and the solution ionic strength.^{9, 61, 69, 178, 179} Beyond just nanoparticle transport in gels, many applications depend on particle transport in other complex fluids such as semi-dilute polymer solutions. In networks, particle transport is dictated by the ratio of the size of particles relative to the size of the mesh network. For particles small, relative to the mesh, particles can diffuse freely in the interstitial fluid. In unentangled polymer solutions, particle dynamics are determined by the distance between neighboring chains. For polyelectrolytes, attractive and repulsive interactions can occur between particle and polymer chain. In addition, same charge on the polymer chains results in repulsions between monomers that alter the chain dynamics and stiffness in the semidilute regime. These conformational changes likely affect the diffusive properties of nanoparticles within the solutions as well. *In vivo*, there is growing evidence that small molecule transport through crowded cytoplasmic environments effects the cellular function.^{180, 181} Changes in concentration of charged biopolymers present *in vivo*^{15, 178, 182-184} with their related effects on viscoelastic properties,¹⁸⁵ requires a proper interpretation of characteristic length scales like mesh size, effects of polymer entanglements affecting probe-polymer interactions, and characterizing the transport mechanisms in different polymer regimes.¹⁸⁶

To gain insight into the complex interactions responsible for selective filtering in biogels, it is useful to examine transport within simpler model systems. We report here on biophysical studies to better understand the importance of electrostatics on particle filtering within reconstituted water-soluble polymer solutions. Fluorescence correlation spectroscopy (FCS) experiments are performed to determine translational diffusion coefficients on charged probe molecules in uncharged and charged polymer solutions. Probe transport within neutral and charged branched polysaccharide (dextran) were performed in both the semi-dilute and concentrated polymer solution regimes. To systematically investigate the effect of probe charge, a series of dye molecules with nearly identical core chemistry and size, but varying net molecular charge (0 to -3) were used. To investigate the effect of polymer chain charge density, probe transport in the relatively low charged dextran solutions was compared to transport within a highly charged polyvinylamine (PVAm) solution.

Previously, we showed that nonsteric interactions are crucial to understanding particle diffusivity of a charged probe molecule within dextran hydrogels.^{111, 187} By theory and experiment, we showed that particle filtering of a -2 probe dye was highly charge asymmetric with particles being strongly immobilized in the gel vertices in oppositely charged gels due to their attractive interactions. In this work, we show the filter capabilities of charged and uncharged dextran solutions are nearly identical for both semidilute and concentrated polymer solutions (i.e., both below and above the critical overlap concentration). Probe charge has nearly no effect in uncharged dextran or repulsive dextran solutions but has a strong charge-dependent effect on the hindered diffusion within attractive dextran solutions. In contrast, all probes, regardless of net molecular charge, were observed to have strongly hindered diffusion within the highly charged PVAm solutions. Next, we examined additional non-electrostatic interactions using a biotinylated probe molecule. Compared to the non-biotinylated probe with the same net charge, the biotinylated probe shows hindered particle diffusivity presumably due to additional hydrogen bonding or Van der Waal interactions between biotin and the dextran polymer chains. Lastly, we show that particle diffusivity in both attractive dextran and PVAm polymer solutions has a salt dependence that varies with both probe molecule charge as well as the polymer network charge density indicating the importance of attractive

electrostatic interactions for particle filtering. Interestingly, the transport properties showed a characteristic crossover behavior at a critical salt concentration that varied depending on the probe charge and polymer composition. In the positively charged dextran solutions, neutral and -1 probes showed little salt dependence while probes with higher net molecular charge showed increased particle diffusivity with the addition of salt up to ~100 mM. While the diffusion coefficient increased, the measured D plateaued at a lower value than that observed in neutral polymer solutions suggesting the electrostatics were not fully screened even at salt concentrations as high as 500 mM. In the highly charged PVAm solutions, probe transport increased but plateaued at ~200 mM NaCl for net neutral zwitterionic probe and at ~400 mM for all negatively charged probes. The crossover behavior with solution ionic strength indicated the potential for gating behavior within these semidilute polymer solutions.

3.2 Materials and methods

3.2.1 Materials: For this study, uncharged and charged dextrans were purchased. Dextran (DEX) is charge-neutral, carboxymethyl-dextran (CM-dextran, Dex (-)) is negatively charged, and diethylaminoethyl-dextran (DEAE-dextran, Dex (+)) is positively charged. Low and high molecular weight dextran (DEX, 15-25 kDa and 500kDa mol wt.), DEAE-dextran (Dex (+), 20 kDa and 500 kDa mol wt) and low molecular weight CM-dextran (Dex (-), 15-20 kDa mol wt.), were purchased from Sigma Aldrich (St. Louis, MO). High molecular weight CM-Dextran (500 kDa mol wt.) was purchased from TdB Labs. Polyvinylamine (PVAm, Mw = 25 kDa) was purchased from Polysciences, Inc. A variety of water-soluble fluorescent probe molecules were purchased from Invitrogen (Carlsbad, CA). ATTO488-amine (AT-A, +0 charge), ATTO488-biotin (AT-B, -1 charge), and ATTO488-Carboxy (AT-C, -2 charge) were purchased from ATTO-TEC (Siegen, Germany). Alexa Fluor 488 carboxylic acid (AL-C, -3 charge) (Abs/Em maxima, 500/525 nm) was purchased from ThermoFisher Scientific (Waltham, MA). All of the fluorescent probe molecules (Abs/Em maxima, ~500/525 nm) were used without further purification.

3.2.2 Preparation of methyl ester terminated ATTO: Methyl ester terminated ATTO probe (AT-E, -1 charge) was synthesized by esterification of AT-C as follows. ATTO-488 carboxy (17.5 mmol), methanol (1.0 mL, 17.5 mmol) were mixed in a 5 mL conical vial. Concentrated sulfuric acid (1 mL, 19 mmol) was then added. The reaction mixture was then refluxed for 45 mins using a water condenser at 175 °C. The reaction mixture was subsequently cooled with ice for one hour. To neutralize remaining sulfuric acid, 1.5 mL of 1M sodium carbonate was added. After addition of the carbonate solution two layers were generated in the reaction mixture, the top organic layer was collected containing product. Successful esterification was subsequently determined by ¹H- NMR and FTIR.

¹H-NMR characterization was conducted on a 400 MHz Bruker Avance NEO spectrometer equipped with a smart probe. For NMR analysis, 2.6 mg of probe molecule was dissolved in 1 mL D₂O and data was analyzed with Topspin 4.0.3 data analysis software. FTIR spectra of AT-E and AT-C were collected to confirm the successful esterification using an iS50 FT-IR equipped with a diamond ATR within the range 400-4000 cm⁻¹ equipped with OMNIC software.

¹H-NMR δ (400 MHz, D₂O, TMS, ppm) : δ 2.4-2.9 (-CH₂); δ 6.5-7.0 (-C₆H₅); δ 3.6 (-OCH₃). IR (wavenumber, cm⁻¹): 3395 (O-H stretch); 2900 (C-H stretch)

3.2.3 Preparation of polymer solutions: Dextran and PVAm stock solutions were prepared by dissolving solid polymer powder in 10 mM MES buffer (pH 6.4) and mixing thoroughly to a final concentration of 8% w/v. Solutions were vortexed and incubated overnight at room temperature to ensure uniform mixing. Subsequent dilutions with MES were made from the stock solutions to achieve desired final polymer solution concentrations (2-6% w/v). These diluted polymer solutions were then allowed to equilibrate for 24 h before use. For FCS experiments, fluorescent probe molecules were prepared and mixed with the desired polymer solutions to achieve a final probe concentration of ~5 nM. Samples were then mixed thoroughly and incubated at room temperature for more than 6 h to ensure uniform dispersion of the probe molecules throughout the dextran polymer solution. Samples were then mixed thoroughly by vortexing and incubated at room temperature for more than 8 h to ensure uniform

dispersion of the probe molecules throughout the polymer solution. Following incubation, samples deposited onto a No. 1 glass coverslip and measured directly by FCS at room temperature. Biotinylated ATTO dye (AT-B) was observed to interact with the glass coverslip and thus required surface passivation of the glass coverslip. For experiments involving AT-B, coverslips were passivated by PEGylation of the surface as described below.

3.2.4 Preparation of PEG-coated glass: To prevent nonspecific binding of the biotinylated dye molecule (AT-B) to the surface of the glass coverslip, coverslips (No. 1, Fisherbrand) were surface passivated using methoxy-PEG (mPEG) silane¹⁸⁸. Glass substrates were sonicated in 5 M NaOH for a period of 60 min at 45 °C. Once cooled to room temperature, coverslips were thoroughly rinsed with Barnstead GenPure 18 MΩ DI water followed by rinsing with 100% EtOH then blown dry with N₂ gas. Next, coverslips were sonicated for an additional 60 min in 0.1 M HCl at 45 °C and rinsed and dried in the same way. Coverslips were then plasma cleaned with a Harrick PDC-32G using the high setting for a period of 4 min to ensure no remaining organic impurities were left on the surface. Cleaned coverslips were subsequently reacted with a 2 mg/ml methoxy-PEG (mPEG, MW 5000 Da) silane solution in 95 % ethanol and incubated at room temperature for 30 mins. The excess PEG was rinsed with ethanol and water and the coverslips were dried overnight or under N₂ before use.

3.2.5 FCS set up: All FCS measurements were carried using a commercial dual-channel confocal fluorescent fluctuation system (ALBA FFS system, ISS, Champaign, IL). FCS experiments were made using a continuous wave 488 nm laser diode as an excitation source. The emitted light was then passed through a 514 nm long pass edge filter before detection of signals. Excitation light was directed into experimental samples through a Nikon Ti-U microscope (60×/1.2 NA water-immersion objective lens). The emission signal was recorded by separate Hamamatsu H7422P-40 PMTs. Confocal volume dimensions were determined through measurement of aqueous Rhodamine 110 at known

concentrations. All FCS measurements were performed using 50 μL of sample deposited on a glass coverslip (24 x 60 mm) with sampling times of 60 s. To ensure homogeneity of measurements within the solutions, all FCS results shown are taken as an average of at least 9 measurements at various positions within the sample. FCS curves were analyzed using the VistaVision Software (ISS, Champaign, IL) to determine the diffusion coefficient with measured diffusion coefficients expressed as the mean \pm SD.

3.2.6 FCS Data analysis: The principles of FCS have been described in detail in literature^{189, 190} and chapter 2 of this dissertation. Here, we provide a brief overview. FCS measures the fluorescence fluctuations emitted from labeled molecules moving in and out of a small ~ 1 fL confocal volume. The size of the effective illumination volume is fixed by the confocal detection optics and the excitation profile of the focused laser beam and characterized by measurements against standard Rhodamine 110 of known diffusion constant ($D = 440 \mu\text{m}^2/\text{s}$).¹⁹¹ For uniformly distributed fluorescent particles diffusing by Brownian motion, dynamic information can be determined from the intensity fluctuations by means of a time autocorrelation given by

$$G(\tau) = 1 + \frac{1}{N} \left(1 + \frac{\tau}{\tau_d}\right)^{-1} \left(1 + \frac{\tau}{\beta^2 \tau_d}\right)^{-\frac{1}{2}} \quad (1)$$

where N is the average number of molecules in the detection volume, τ is the delay time, τ_d is the characteristic diffusion time, or the average passage time of a molecule through the confocal volume, and β is the structure parameter ($= z_o/\omega_o$) is the ratio of the axial to the radial dimensions of the confocal observation volume as determined by calibration measurements using dye with known diffusion constant. Here, β was fixed to 10 in all fits, based on results from calibration measurements with Rhodamine 110. Cross correlation with both detectors minimizes the effects of detector after-pulsing in the resulting autocorrelations. The translational diffusion coefficient D ($\mu\text{m}^2/\text{s}$) can be calculated from τ_d and the radial width using

$$\tau_d = \frac{\omega_o^2}{4D} \quad (2)$$

For spherical particles, the diffusion coefficient D follows from the hydrodynamic radius, R_h , in solution and can be calculated by the Stokes-Einstein relation $D = k_B T / 6\eta\pi R_h$, where k_B is the Boltzmann constant, T is the temperature, and η is the viscosity of the medium.

3.3 Results and discussion

3.3.1 Solution behavior of polymers

Polymers are well known to change their behavior in solution as a function of concentration. To summarize this behavior, we will briefly discuss dilute, semi-dilute and concentrated polymer solutions.^{192, 193} At low polymer concentrations, individual polymer chains are well separated from each other and behave like isolated ideal chains (**Figure 3.1 left**). The size of polymer chains in dilute solution is often described by the radius of gyration, R_g , defined as the mass weighted average distance of a chain segment from the center of mass of the molecule.¹⁹⁴ Some methods, including DLS and FCS, measure

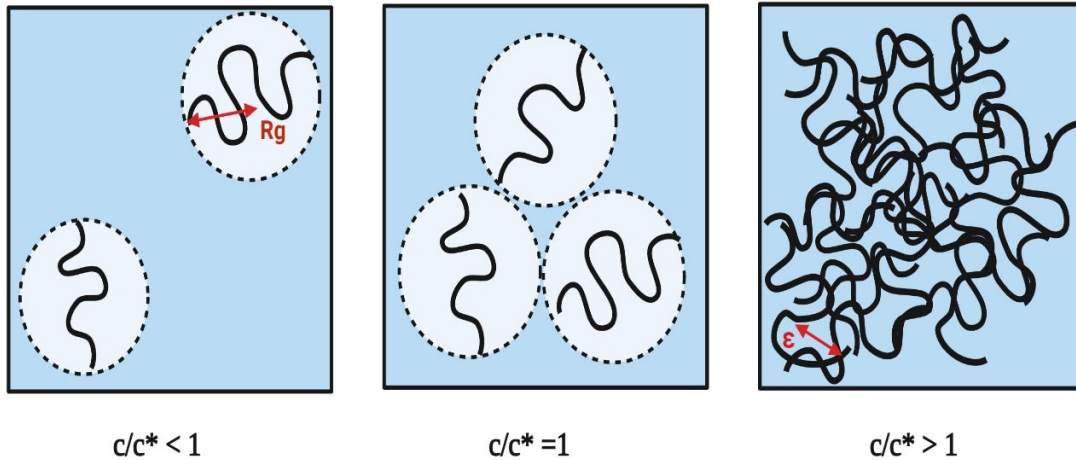


Figure 3.1 Graphical representation of the dilute, semidilute and concentrated regimes for polymer solutions. c represents the polymer concentration in the solution and c^* denotes the critical overlap concentration of the polymer coils.

properties dependent on the hydrodynamic properties of the polymer chain such as the translational diffusion coefficient D_t . D_t is related to the hydrodynamic radius (R_h) through Stokes-Einstein equation ($D = k_B T / 6\pi\eta R_h$). R_h of the dilute polymer chains is typically

comparable in size to the polymer R_g . At or near the overlap concentration (c^*), coils begin to overlap and be randomly packed (**Figure 3.1, middle**) defining the semidilute regime. In this regime, the polymer chain can be described by a blob model where a blob represents the average unit length of the polymer that is not overlapping with other polymer chains.¹⁹⁵ In a semi-dilute solution, polymer density fluctuations play an important role determining interactions between neighboring chains.¹⁹⁶ In this range, the polymer chains may interpenetrate but do not topologically entangle like in the concentrated regime (**Figure 3.1, right**). Above the critical polymer concentration, the polymer coils become more entangled and interpenetrate to form network-like structure. These networks can be characterized by a correlation length, or mesh size ξ , characteristic of the resulting size of the pores within the network of entangled polymer chains. These entangled polymer solutions mimic the sieving properties of covalently crosslinked gels.

3.3.2 Dextran and polyvinylamine polymer

For this study on probe transport in semidilute and concentrated polymer solutions, neutral and charged dextran polymers of approximate molecular weight (MW) 20kDa and 25 kDa were used. Dextran is a complex branched polysaccharide typically obtained from the bacteria *Leuconostoc mesenteroides*. Dextran consist primarily of linear glucose chains linked by α -D-(1-6 linkages) with a small degree (~1-5%) of short branches resulting from α (1 \rightarrow 2), α (1 \rightarrow 3), and α (1 \rightarrow 4)-linkages.¹⁶⁴ As we are interested in electrostatic contributions to the probe-polymer interaction, we also used carboxymethyl-dextran [CM-DEX, Dex(-)] and diethylaminoethyl-dextran [DEAE-DEX, Dex(+)] which are polyanionic and polycationic derivatives of dextran. A simplified structure for dextran and the charged dextran (Dex(-) and Dex (+)) are shown in **Figure 3.2**. Both Dex(-) and Dex (+) have relatively low chain charge density with Dex(-) having approximately one negative charge per five glucoses, whereas Dex(+) has approximately one amine group per three glucoses.

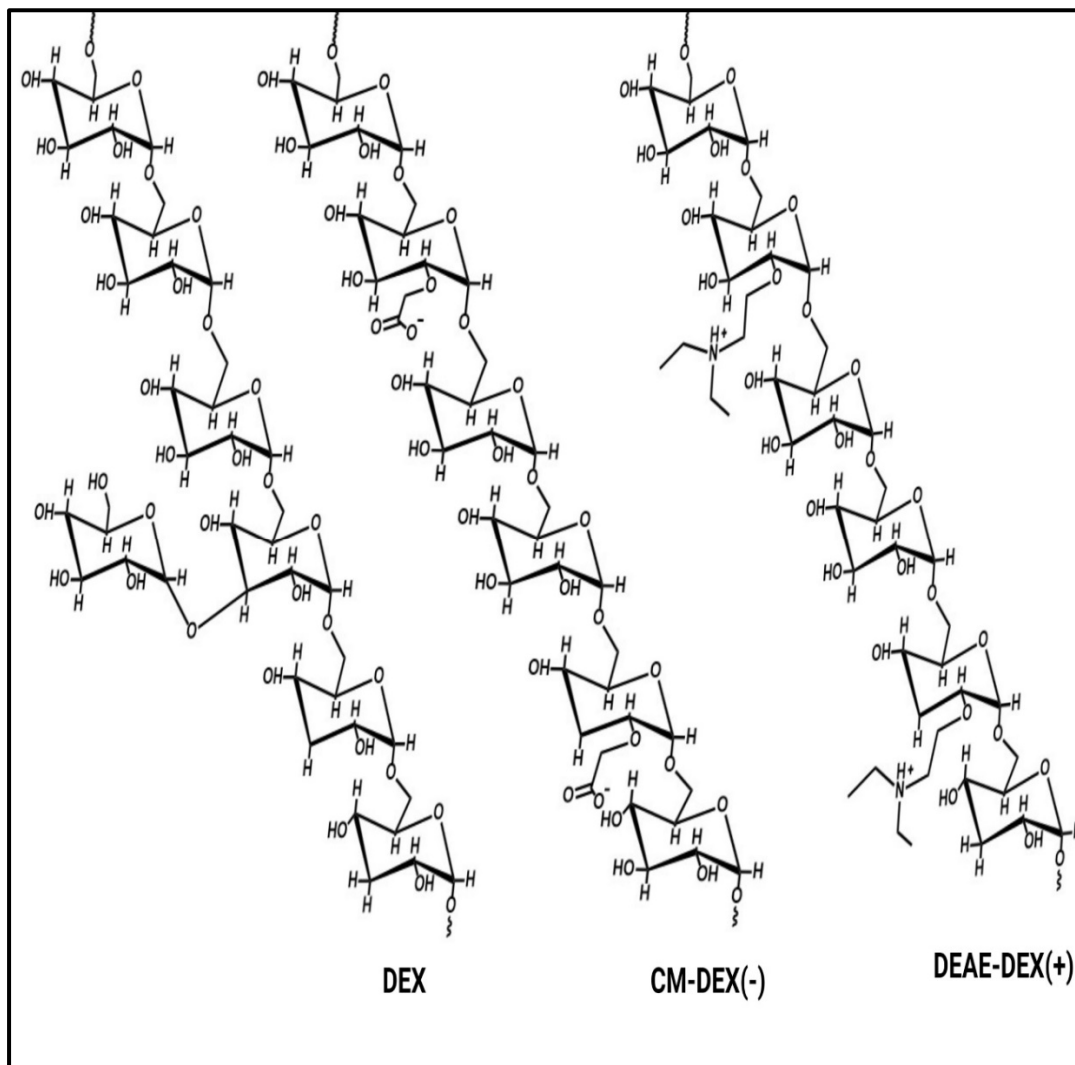


Figure 3.2 Chemical structures for dextran polymers used in this study. (a) Structural fragment of dextran chain with dextran (1-3) branch unit, carboxymethyl-dextran [CM-DEX, Dex(-)], diethylaminoethyl-dextran [DEAE-DEX, Dex(+)].

For a comparative study with a high charge density polymer, we used 25 kDa polyvinylamine (PVAm). PVAm is typically synthesized by the hydrolysis of polyvinylformamide. The synthesis and chemical structure of polyvinylamine (PVAm) is shown in **Figure 3.3**. PVAm is a highly water-soluble polymer with the highest content of primary amine functional groups of any polymer. PVAm find use in a wide range of

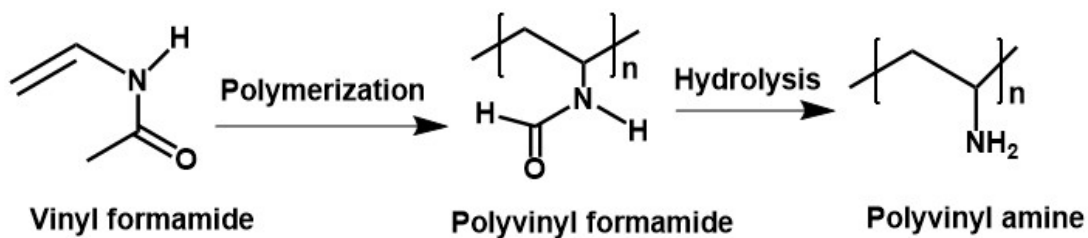


Figure 3.3 Synthesis of polyvinylamine from the hydrolysis of polyvinylformamide.

applications including surface modification¹⁹⁷, CO₂ capture¹⁹⁸, and gene delivery.¹⁹⁹ While ethylamine has a pKa of 10.7, meaning it is nearly completely ionized at neutral pH, PVAm is partially ionized at most pHs. This partial ionization behavior is a result of interactions with neighboring amine groups and is well known phenomenon for polyelectrolytes. For MES buffer (pH 6.4), as used in this study, PVAm has ~75% of its primary amines ionized.¹⁹⁷

3.3.3 Fluorescent probes

To systematically examine the effect of probe charge on the transport properties within our polymer solutions, we used a series of fluorophores with similar size and core structure but varying net molecule charge. The chemical structure for all probes used in this study and their net molecular charge are given in **Figure 3.4**. Four of the five probes are based on the same ATTO 488 core structure. Amine terminated (AT-A, 0), methyl ester terminated (AT-E, -1), biotinylated (AT-B, -1), and carboxy terminated (AT-C, -2) were used. For a net charge of -3, a carboxylic acid Alexa Fluor 488 (A-C, -3) was used which has a core structure similar to the ATTO probes. All probes were determined by FCS to have a

hydrodynamic radius of $R_h \sim 6.2 \text{ \AA}$ in water except for the much larger biotinylated probe which had an R_h of 7.8 \AA .

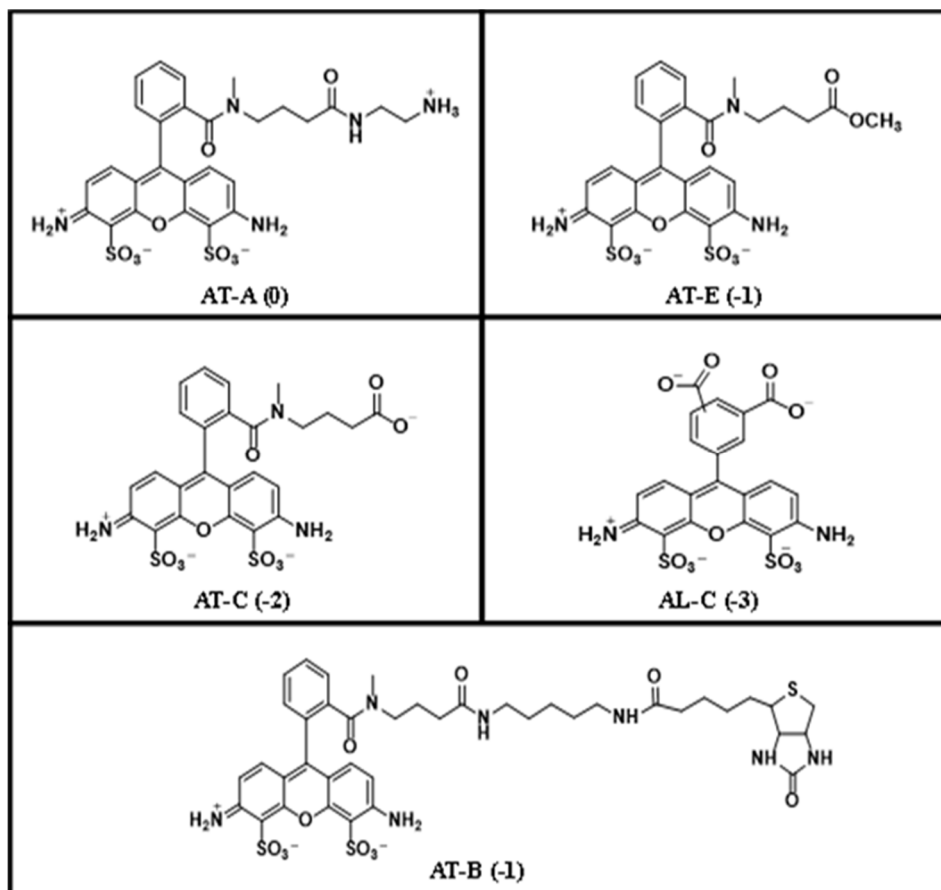


Figure 3.4 Molecular structures of the five probes used in this study.

AT-E (-1) was synthesized via Fischer's esterification reaction of AT-C as described in the methods. The resulting product was purified and characterized using ^1H NMR and FTIR (**Figure 3.5**). The ^1H -NMR spectra of AT-C and AT-E are shown in **Figure 3.5a**. Both probes have core substituent protons (a-d) that have chemical shifts at ~ 2.4 - 2.9 ppm, and phenyl protons that have chemical shifts at 6.5 - 7.0 ppm (e-h) and 8.8 - 9.1 ppm (i-j) respectively. Upon successful esterification of AT-C to form AT-E, a characteristic methoxy proton peak is observed at 3.6 ppm. **Figure 3.5b** shows FTIR spectra for AT-E and AT-C. Upon successful esterification of AT-C, the characteristic O-H stretch (3395 cm^{-1}) and out of plane O-H bending (950 cm^{-1}) found in AT-C disappear with a subsequent

sharp rise in symmetric and asymmetric C-H stretching (2900 cm^{-1}) for AT-E evidence of a successful conversion of the carboxylic acid of At-C to the methyl ester of At-E.

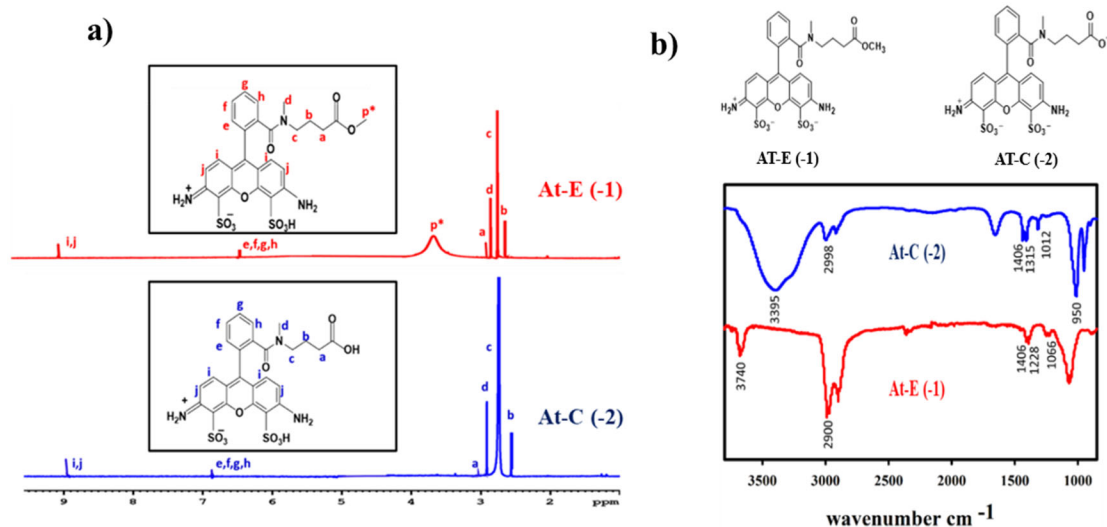


Figure 3.5 Characterization of AT-E synthesis. (a) ^1H -NMR of AT-E and AT-C probes. A characteristic peak at 3.6 ppm is observed due to the methoxy protons after esterification of AT-C. (b) Chemical structures and FTIR spectra of AT-E and AT-C. By FTIR, the characteristic -OH stretch (3395 cm^{-1}) and out of plane O-H bending (950 cm^{-1}) peaks of AT-C disappear upon successful esterification to AT-E.

3.3.4 Polymer properties and calculation of overlap concentration c^*

As discussed in 3.3.2, dextran is a highly soluble polysaccharide produced by bacteria through the condensation of glucose. The main chain is formed from $\alpha(1\rightarrow6)$ linked D-glucose units but, depending on the bacterial strain, have varying ratios of linkages and branches. In dilute solution, dextran behave like flexible random coil polymers.²⁰⁰ The molecular dimensions of dextran depend on both the molecular weight and polymer concentration. The space occupied by a flexible polymer chain in solution is characterized by radius of gyration R_g , which is the root mean square of segment distances from the center of gravity of the molecule.^{201, 202} In this work, we used high (500 kDa, Dex500) and low (20kDa, Dex20) molecular weight dextran. Previous work has shown that polymer

scaling for the radius of gyration is different for low and high molecular weight dextran depends on branching and thereby changing viscosity effects. For polymers with molecular weight $< 10^5$, R_g can be determined by $R_g = 0.83 M^{0.41}$, where the scaling factor 0.41 is for polymers in a good solvent. For higher MW dextran polymers, it was shown that R_g scales as $0.37 M^{0.41}$ due to higher degree of branching.²⁰³ The calculated R_g for Dex500 and Dex20 is therefore 18 nm and 4.2 nm, respectively (**Table 3.1**). Comparable R_g values have been reported for Dex500 by light scattering experiments ($R_g \sim 18$ -19 nm)²⁰⁴ and by calculations from measured intrinsic viscosities ($R_g \sim 16$ nm).²⁰² We also used a low MW (25kDa) polyvinylamine (PVAm), a water-soluble polyamine, with a calculated $R_g = 4.7$ nm.

The correlation length, ξ , characterizes the average distance between entanglements in the concentrated region and is proportional to the individual coil sizes in the semi-dilute region of flexible polymers.²⁰⁵ It is expressed as, $\xi = R_g \left(\frac{c}{c^*}\right)^{-0.75}$ and is related to the ratio of the polymer concentration (c) to the overlap concentration (c^*). The critical overlap concentration defines the boundary between the dilute and semi-dilute regimes and represents the concentration at which different polymer chains cease being separated from each other and begin to overlap as depicted in **Figure 3.1**. c^* depends on the molar mass of the polymer and can be calculated using $c^* = \frac{M_p}{\left(\frac{4}{3}\pi(R_g)^3 N_A\right)}$ where M_p is the molecular weight of the polymer and N_A is Avagadro's number.²⁰⁶ The calculated values for overlap concentration and correlation lengths for Dex500, Dex20, and PVAm are listed in **Table 3.1**. For 500 kDa Dextran, polymer concentrations of ~ 2 wt% or higher result in concentrations above the overlap concentration (**Figure 3.1, right**). For the 20 kDa Dex and 25kDa PVAm, overlap concentrations are ~ 10 wt%, with polymers between 2-10% being in the semidilute range (**Figure 3.1 middle**).

Table 3.1 Molecular dimensions of polymers as determined for R_g , c^* , ξ

Polymer	R_g (nm)	c^* (g cm ⁻³)	ξ (nm) at $c=c^*$
Dex 500	18	0.024	18
Dex 20	4.2	0.100	4.2
PVAm	4.7	0.095	4.7

3.3.5 Microviscosity for probe diffusion in neutral polymer networks

When particle radius, R , is larger than the correlation lengths, ξ , inside the polymer solution, diffusion coefficients can be calculated using the Stokes-Einstein (SE) relation using the macroscopic viscosity of the polymer solution. However, for nanoparticles with $R \leq \xi$, diffusion much faster than expected from bulk viscosity is observed. The apparent diffusion coefficient in polymer networks and semi-dilute polymer solutions can, however, be described by SE relation where the macroscopic viscosity is replaced by a size dependent apparent viscosity, or microviscosity, that reflects the local environment influencing the transport properties of the nanoparticles within the void volumes between polymer chains.^{186, 206} Before investigating the charge-charge interactions between probe and polymer, we first determined the probe diffusion of the neutral zwitterionic At-A in uncharged dextran polymer systems Dex20 and Dex500 at 4 wt%. This concentration represents a semi-dilute polymer solution for Dex20 and a concentrated polymer solution for Dex500 with $c > c^*$. As the probe is net charge neutral and the dextran solutions are uncharged, diffusion of the probe inside the polymer solutions should be dictated by sterics. The apparent diffusion coefficients, as determined by FCS, were similar with $D = 336 \pm 5 \mu\text{m}^2/\text{s}$ and $328 \pm 8 \mu\text{m}^2/\text{s}$ for Dex20 and Dex500 respectively. Errors measured for an average of at least 9 measurements at various positions within each sample. Using the experimentally determined hydrodynamic radius of At-A in buffer at room temperature, $R_h = 0.62 \text{ nm}$, the microviscosity can be calculated using the Stokes-Einstein relation $D = \frac{k_B T}{6\pi\eta R_h}$ where η is the apparent viscosity, T is the temperature (295 K), and k_B is the Boltzmann constant $1.38 \times 10^{-23} \text{ JK}^{-1}$. The microviscosity values obtained were nearly identical for dextran solutions above and below c^* with $\eta = 1.11 (\pm 0.50) \times 10^{-3} \text{ Pa s}$ for 4 wt% Dex 20 compared to $\eta = 1.15 (\pm 0.21) \times 10^{-3} \text{ Pa s}$ for 4 wt% Dex 500. As expected, the measured microviscosities are small compared to bulk viscosity for dextran. For example, 5 wt% Dex500 was determined to have a bulk viscosity of 0.01 Pa s by cone-plate rheometer measurements.²⁰⁷ Normalized viscosity (η/η_0) for At-A was determined to be 1.28 with solvent viscosity $\eta_0 = 9.01 \times 10^{-4} \text{ Pa s}$. This value is similar to previously reported normalized viscosities for labelled calmodulin protein, where $R < \xi$, in

comparable wt% solutions of Dex25 and Dex500.²⁰⁸ The reduced microviscosity results in At-A diffusing faster than expected for bulk viscosity within the Dextran solutions.

3.3.6 Probe transport properties inside neutral and charged semidilute polymer solutions

Next, we focused on understanding charged probe diffusion in neutral and charged semidilute polymer solutions. Previously, we used FCS to measure the transport properties of a single charged dye probe (net charge -2) inside neutral and charged dextran polymer solutions above the overlap concentration.¹⁰⁹ We showed that particle transport was highly asymmetric with probe diffusion being greatly reduced within attractive hydrogels (e.g. negative probe in positively charged polymer hydrogels) but are not significantly hindered in repulsive gels. Despite anticipating the probes in repulsive gels to further hinder particle transport, we actually observed that the negative probe diffusion was nearly identical in the

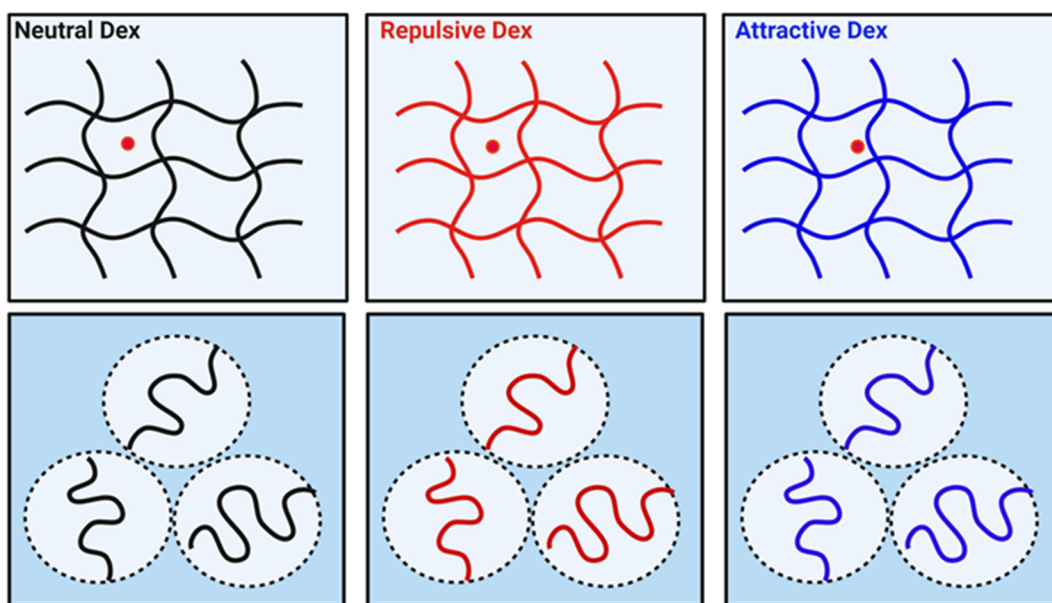


Figure 3.6 (top row) Cartoon depiction of a negatively charged particle diffusing in neutral (Dex), repulsive (Dex(-), and attractive (Dex(+)) dextran physically crosslinked polymer networks where polymer concentration is above c^* . Particle diffusion in attractive gels is slowed down due to strong attractive interactions with the network vertices (bottom row). Cartoon depiction for this work with probe diffusion in semi-dilute neutral, repulsive, and attractive semi-dilute polymer solutions.

repulsive Dex(-) hydrogels as in neutral Dex hydrogels. Brownian dynamic (BD) simulations were performed in collaboration with the lab of Roland Netz (Freie Universität Berlin) revealing particles in attractive gels associating most strongly in the vertices of the polymer network.¹⁰⁹

Here, we focused on At-C (net charge -2) diffusion in semi-dilute attractive and repulsive dextran polymer solutions. **Figure 3.7a** show normalized autocorrelation functions of the negatively charged At-C in solutions of 20kDa Dex(-) as a function of polymer concentration. To stay in the semi-dilute regime, we focused on 2-8 wt% dextran solutions as we calculated $c^* > 10$ wt% for 20kDa dextrans. In the repulsive Dex(-) semidilute solutions, we see a modest increase in the characteristic diffusion time τ_d only weakly increasing with increasing Dex(-) concentration. The translational diffusion coefficient D for At-C in Dex(-) over this concentration regime are nearly identical to those measured in uncharged 20kDa Dextran. These results are also comparable to what was previously observed in 500kDa Dex or Dex(-) where the polymer solution is above the critical overlap concentration resulting in an entangled network.¹⁸⁷ In the attractive semi-dilute 20kDa Dex(+) solutions (**Figure 3.7b**), however, we see large changes in the τ_d that are dependent on Dex(+) weight percentage. The largest increase in τ_d , or equivalently largest decrease in translational diffusion coefficient D , was observed between the pure buffer (0 wt%) and 2 wt% Dex(+). Modest increase in τ_d is observed for increasing polymer concentration within the semi-dilute regime. Again, these results in semidilute Dex(+) solutions are very comparable to what is observed for 500kDa Dex(+) in the concentrated regime.¹⁸⁷

To examine how the polymer chain charge density effects particle transport within semidilute polymer solutions, we also looked at At-C diffusion within PVAm. **Figure 3.7c** shows normalized autocorrelations of At-C in solutions of 25kDa PVAm as a function of polymer concentration. Even larger changes in the characteristic diffusion time are observed for the probe in the attractive PVAm solution when compared to Dex(+) solutions. This corresponds to increased hindered diffusion of At-C in semidilute attractive PVAm solutions compared to attractive dextran solutions. This hindered diffusion was not particularly sensitive to polymer concentration in the range of 2-8 wt%. Many biogels,

include mucus, extracellular matrix, and nuclear pore complexes, are known to not only filter particles due to steric interactions but also use interaction filtering mechanisms to allow some particles to pass through the biogels while others are kept out. Controlling particle transport through repulsive and attractive electrostatic interactions is one way to control the filtering capability within these biogels. Similarly, we show that attractive electrostatic interactions also control charged particle transport within semidilute polymer solutions, and that particle diffusion is also dependent on the polymer charge density. For example, At-C diffusion in 2 wt% dextran and Dex(-) solutions was $D = 350(\pm 6) \mu\text{m}^2/\text{s}$ and only slightly hindered when compared to pure buffer. This is consistent with sterics playing only a small role in the hindered probe diffusion in neutral and repulsive semidilute polymer solutions. In contrast, At-C diffusion in 2 wt% Dex(+) semidilute solution was reduced approximately 2.5-fold to $D = 142(\pm 6) \mu\text{m}^2/\text{s}$ due to attractive electrostatic interactions. In a 2 wt% highly charged PVAm semidilute polymer solution, however, we see this particle transport reduced by ~ 15 -fold to $D = 23(\pm 5) \mu\text{m}^2/\text{s}$ compared to similar 2 wt% semidilute solutions of neutral or repulsive dextran solutions of comparable molecular weight.

3.3.7 Effect of probe charge on particle transport in semidilute dextran and PVAm solutions

Next, we systematically investigated the effect of probe charge on the transport properties within neutral and charged semidilute polymer solutions. Any electrostatic effects would be expected to have a strong dependence on the probe net molecule charge. Plotted in **Figure 3.8** are the relative diffusion coefficients (D/D_0) as a function of polymer concentrations for At-A (0), At-E (-1), At-C (-2) and Al-C (-3). D_0 is the probe diffusion in pure buffer (10mM MES buffer, pH 6.4). As before, we used 20kDa Dextrans and 25kDa PVAm at concentrations below 10 weight percent to ensure we stayed below the c^* for each polymer system. For probes charged 0 to -2, the relative diffusion coefficients measured by FCS are reduced by $\sim 35\%$ in Dex and Dex(-) semidilute solutions over the

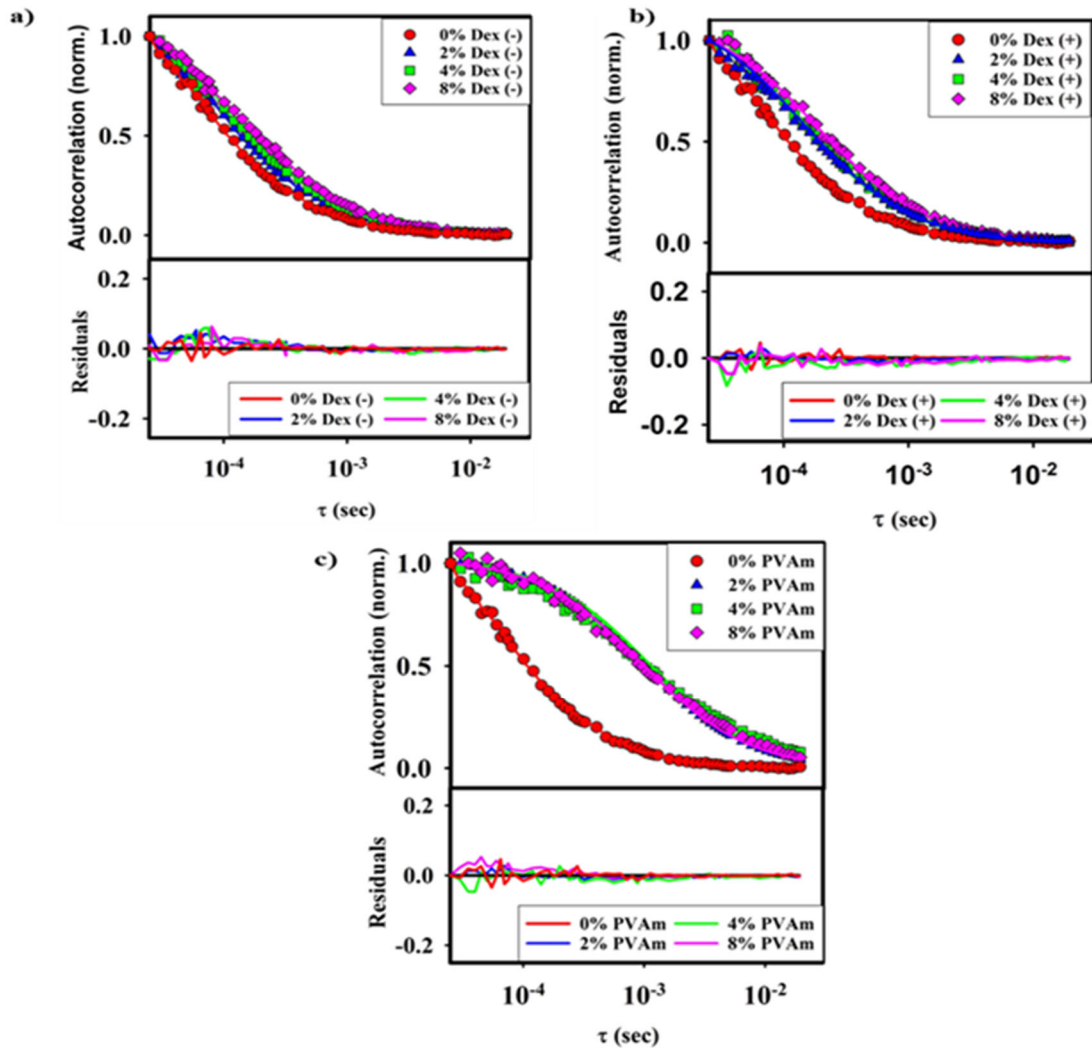


Figure 3.7 Representative normalized FCS autocorrelation curves for the diffusion of negatively charged ATTO 488 carboxy (At-C, -2) in varying weight volume percent solutions (0-8 wt%) of (a) Dex(-), (b) Dex(+) and (c) PVAm solutions in 10 mM MES buffer (pH 6.4). Solid lines represent fits to the experimental data by equation 1 to determine translational diffusion coefficients. This data characterizes the filtering function in different hydrogel systems. Molecular mobility of the charged probe is highly hindered in the high charge density attractive gel (PVAm) compared to low charge density Dex(+), whereas its mobility is nearly unhindered in the repulsive Dex(-) system.

range of 2-8 wt% polymer concentration. The -3 charged Al-C dye shows a stronger reduction of ~40% over the same polymer concentration range. Results in Dex(-) are nearly identical to those in uncharged Dex, indicating the probe molecules do not interact significantly with the dextran polymer chains. The reduced diffusion observed signifies the dominant hydrodynamic and steric interactions between probe and polymer chains that dictate the particle transport within the polymer solutions. Surprisingly, the -1 charged At-E dye and the net neutral At-A dye show comparable behavior in the attractive Dex(+) semidilute solutions as that observed in neutral and repulsive dextran semidilute solutions. Only at probe charge ≥ -2 , do we see significant hindered diffusion due to attractive electrostatic interactions between probe and polymer chains in the semidilute regime. For At-C (-2) probe, D is reduced ~48 % for 2 wt% Dex(+) solution and is nearly unchanged with increasing polymer concentration up to 8 wt%. For Al-C (-3) probe, the relative diffusion is decreased even further (~76 %) with a minimum D measured at 2 wt% and a slight increase in D/D_0 as the polymer concentration is increased further. This increase in D/D_0 may be due to the -3 probe being more shielded by the higher counterion concentration resulting in weaker probe-polymer interactions.

In contrast to dextran, the relative diffusivity is greatly reduced (>90%) in the presence of PVAm regardless of the net probe charge. This can be explained by enhanced probe-polymer attractive electrostatic forces due to the high charge density on the PVAm chains, resulting in significantly hindered particle diffusion in the attractive semidilute PVAm solutions. Even for the neutral but zwitterionic At-A (0) probe, we see significant interactions between the probe and the PVAm solution. With increasing probe charge, the relative diffusion is reduced further with D/D_0 reduced as much as 95% for Al-C (-3) probe. The measured diffusional coefficients for all probes within the attractive PVAm semidilute solutions are not significantly altered with increasing polymer concentration up to 8 wt %. While not quite as strongly hindered, we note that the Al-C (-3) behavior in Dex(+) is similar to the transport observed for all probes in PVAm solutions. This suggests the transport properties for probes in attractive, low-charge density polymer solutions can begin to approach the behavior of charged probes in attractive, high-charge density polymer solutions with sufficiently high net molecular charge on the probe.

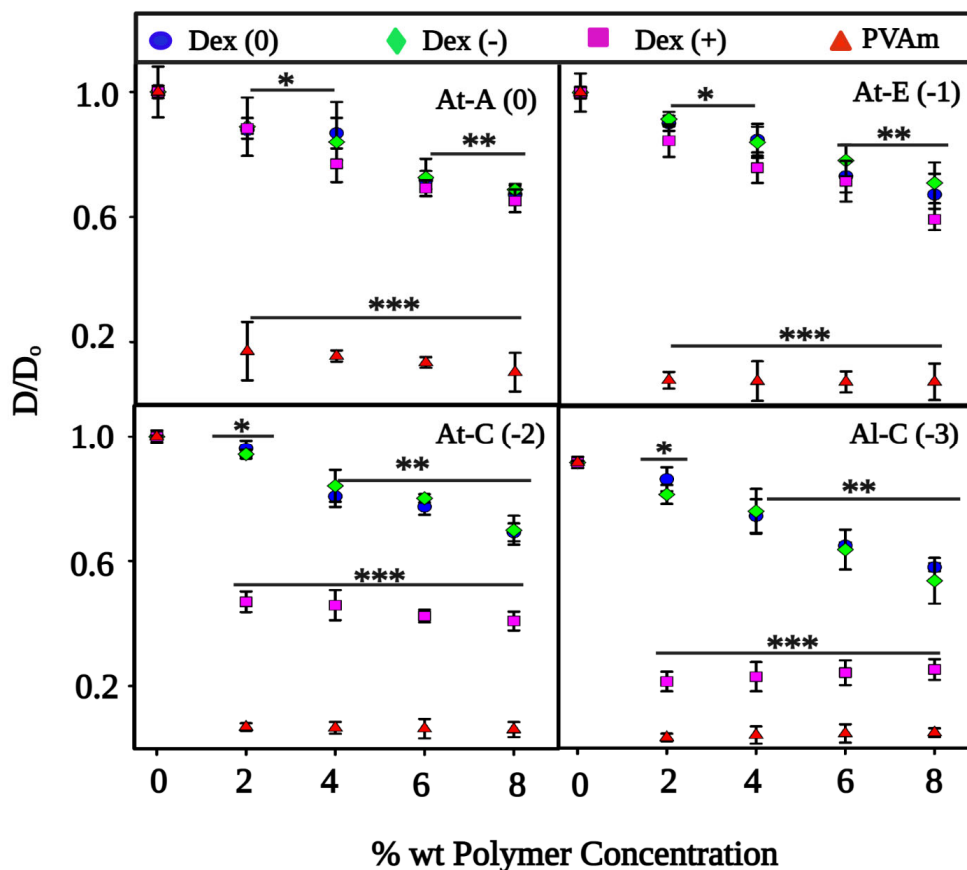


Figure 3.8 The relative diffusivity (D/D_0) as a function of polymer concentration plotted for charged probes in neutral and charged Dextran and PVAm polymer solutions. Similar sized, but different net charged probes At-A (0), At-B (-1), At-C (-2) and Al-C (-3) were used. Significant hindering of particle diffusion in attractive gels is only observed for probes ≥ -2 in dextrans while all probes show greatly reduced particle transport in PVAm. With increase probe charge, the transport properties within Dex(+) become more comparable to PVAm. * $p < 0.05$, ** $p < 0.01$, *** $p < 0.001$ Vs D_0 of each appropriate solution.

3.3.8 Particle transport of a biotinylated-dye probe in semidilute dextran and PVAm solutions

Biotin is a water-soluble B vitamin involved in a variety of metabolic processes in humans.²⁰⁹ Biotin interacts with certain proteins through a combination of van der Waal forces, electrostatics, and hydrogen bonding.²¹⁰ Most notably biotin binding proteins such as avidin and streptavidin form particularly strong complexes with some of the strongest non-covalent protein-ligand interactions known.²¹¹ To probe potential non-electrostatic effects between probe and our semidilute polymer solutions, we did a comparative study of biotinylated dye (At-B (-1)) to the comparably charged non-biotinylated probe At-E (-1) (**Figure 3.9**). While the previously measured probe dyes showed no significant interaction with the glass coverslips used for FCS measurements, the biotinylated probe showed significant nonspecific adsorption onto the glass coverslip. As anticipated, a lower diffusion coefficient in buffer was observed for At-B compared to At-E due to the larger molecule size of At-B. However, using Stokes-Einstein, this lower D resulted in a calculated hydrodynamic radius of 7.8 Å which is too large to be consistent with the size of the biotin dye. To address this issue, we passivated the glass surface with a PEG brush layer as described in the methods. With the PEG brush layer, we saw no change in D for At-E but a statistically significant increase of D for At-B. Upon surface passivation, we then measured a hydrodynamic radius of 6.6 Å for At-B consistent with biotin undergoing unhindered diffusion.

Using PEG passivated glass, we also characterized the relative diffusion coefficient (D/D_0) as a function of polymer concentration for At-E and At-B in semidilute Dex(+), Dex(-) and PVAm solutions. **Figure 3.10a** shows the normalized autocorrelation curves and normalized diffusion coefficients (D/D_0) relative to probe diffusion coefficients measured in water as a function of increasing 20kDa Dextran polymer concentrations. The measured relative diffusion coefficients for At-E (-1) probe (open symbols) in semidilute Dex(-) solutions on PEG passivated coverslips is nearly identical to the results shown in **Figure 3.10b** for At-E in Dex(-) on non-passivated glass. As discussed, these results are also comparable to that measured for At-E in uncharged dextran consistent with minimal repulsive electrostatic effects on At-E in Dex(-) and diffusion coefficients dependent

primarily on the steric and hydrodynamic effects due to dextran polymer chains. At-E diffusion in the attractive Dex(+) solutions on PEG passivated glass is also similar to the

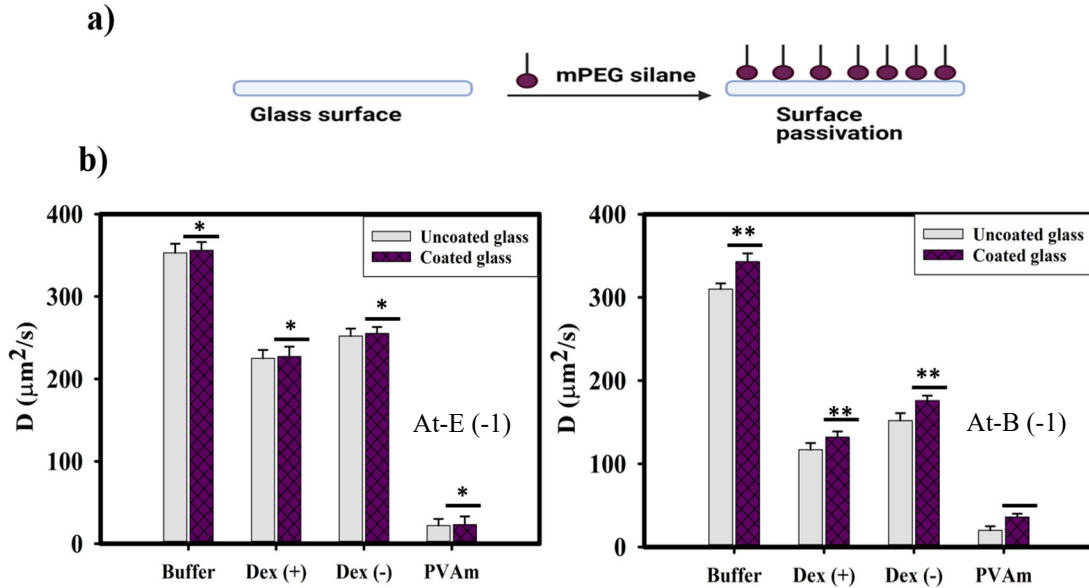


Figure 3.9 Surface passivation of glass coverslips using pegylated silane (a) Depiction of surface passivation of glass coverslips by mPEG silane to reduce non-specific interactions between the biotin-dye and glass (b) Translational diffusion coefficients measured for At-E (-1) and At-B (-1) probes in buffer, charged dextran and PVAm semi-dilute solutions on untreated glass coverslips compared to mPEG-silane treated glass. For At-E, no significant interaction with the glass is observed resulting in statistically indistinguishable D values on uncoated and coated glass. At-B (-1) is larger resulting in a lower D value in buffer. * $p > 0.05$, ** $p < 0.01$ Vs D of non-coated coverslip of each appropriate solution.

data in **Figure 3.8** for At-E in Dex(+) on untreated glass. The attractive electrostatic interactions between the -1 probe and the positively charged dextran chains results in a modest decrease in apparent diffusion coefficient. In contrast, the measured normalized diffusion coefficients (D/D_0) for At-B in the Dex(-) solutions (green diamonds) are significantly reduced compared to At-E. As both probes have a net molecule charge of -1, this cannot be due to electrostatic interactions, but rather suggests hindered diffusion due to non-specific interactions between biotin and the dextran polymer chains. At-B diffusion in the electrostatically attractive Dex(+) solutions shows a further reduction in relative

diffusion; a reduction comparable to that observed for At-E in attractive compared to repulsive dextran solutions. For the highly charged PVAm solutions, the high charge

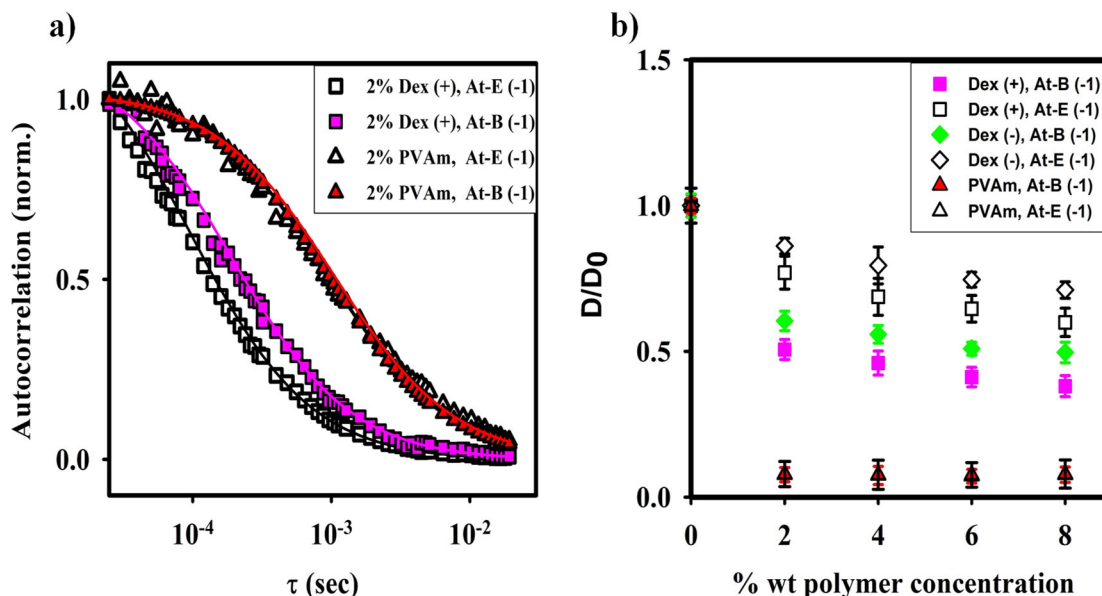


Figure 3.10 (a) Normalized autocorrelation curves and residuals for At-E and At-B probes in 2 wt% Dex(+) and PVAm solutions in 10 mM MES buffer (pH 6.4). Solid lines represent fits to the experimental data by equation 1. In PVAm, both probes are highly retarded with no apparent effect of the biotin on the measured translational diffusion coefficients. In the attractive Dex(+) solutions, additional non-covalent interactions of biotin with dextran results in hindered diffusion relative to At-E probe. (b) Relative diffusivity (D/D_0) for At-E and At-B as a function of polymer concentration in Dex(+) (pink/square), Dex(-) (green/diamond) and PVAm (red/triangle).

density and strong attractive probe-polymer electrostatic interactions greatly reduces the relative diffusion coefficients of both At-B and At-E. No statistically significant difference in D/D_0 is observed suggesting minimal influence on the probe transport due to the presence of biotin.

3.3.9 Salt effects on probe transport within charged semidilute polymer solutions

Lastly, we examined the effect of added NaCl salt concentration on the transport properties of our non-biotinylated probes inside charged semidilute polymer solutions. We would anticipate any electrostatic interactions between probe and polymer chains would have a strong dependence on salt due to the Debye-huckel screening of the charge-charge interactions. Shown in **Figure 3.11** are the translation diffusion coefficients as determined by FCS for At-A (0), At-E (-1), At-C (-2), and Al-C (-3) probe molecules in 2 wt% Dex(+) and Dex(-) polymer solutions.

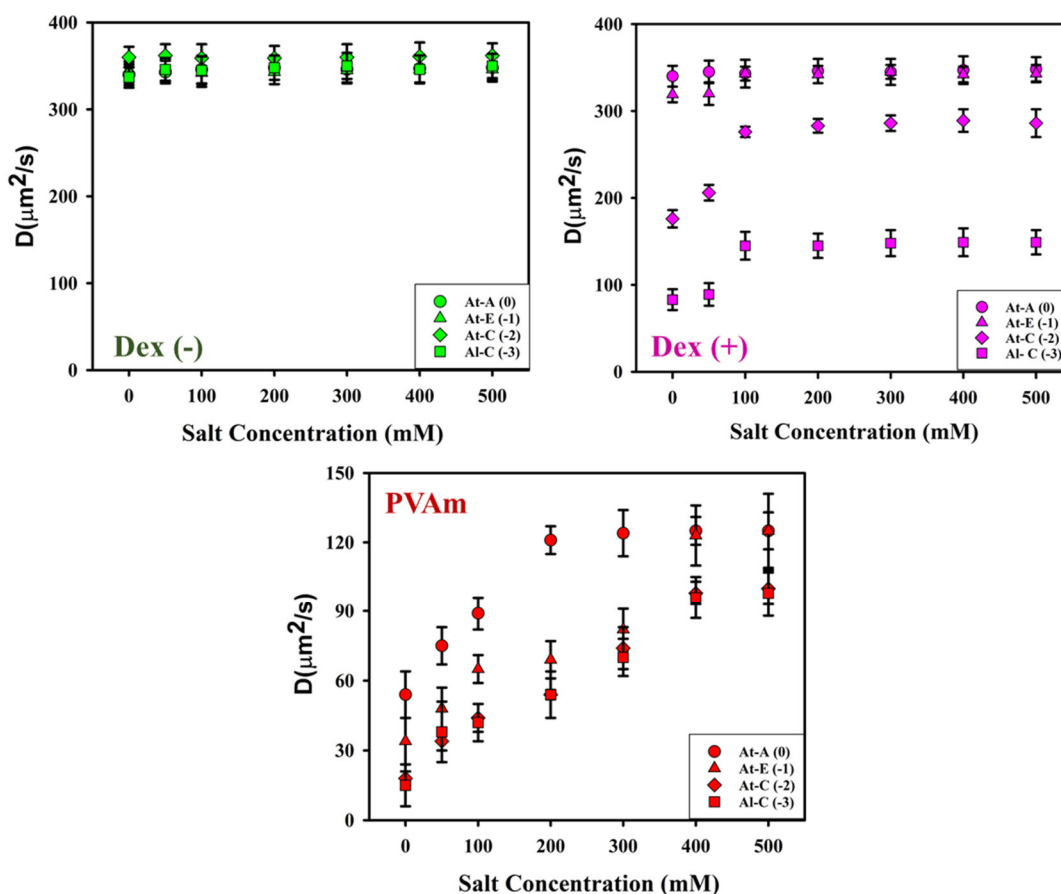


Figure 3.11 Ionic strength effect on translational diffusion coefficients as determined by FCS for At-A, At-E, At-C and Al-C probe molecules in charged Dex and PVAm polymer solution. Here, all data corresponds to 2 wt % polymer solutions of 20 kDa Dex (-), 20 kDa Dex (+) and 25 kDa PVAm.

and Dex (-) polymer solutions and 2 wt% 25kDa PVAm solutions. All systems are well below the calculated critical polymer concentration, c^* , corresponding to semidilute polymer solutions. As expected, diffusion in the semidilute repulsive Dex(-) solution is unaffected by added NaCl salt up to 500 mM regardless of the charge on the probe molecule. Similarly, zwitterionic At-A probe in the attractive Dex(+) solution is also unaffected by added salt suggesting minimal attractive electrostatics between the neutral At-A probe and the Dex(+) chains. As shown previously in **Figure 3.8**, the apparent diffusion coefficient for our probes in attractive semidilute polymer solutions with transport hinderance depending on the probe molecule charge; especially probes ≥ -2 . While the -1 charged At-E dye shows only slightly decreased D in Dex(+), we see that this small attractive probe-polymer interaction can be screened by the addition of ~ 100 mM NaCl salt resulting in At-E diffusion being identical to At-A at NaCl concentration ≥ 100 mM. At-C is significantly reduced due to the -2 net charge on the probe. With added salt, we see D increase and plateau at ~ 100 mM NaCl concentration where D no longer shows a dependence on added salt concentration. Interestingly, while D increases with added salt, the plateau value of D for At-C remains approximately 21% lower than the maximum D observed for At-A and At-E at high salt. At-C (-3) starts at an even lower D in Dex(+) and also shows an increase in D with increased NaCl concentration that plateaus at 100 mM. The characteristic crossover salt concentration for all four probes in Dex(+) is observed around 100 mM salt concentration.

In contrast, PVAm strongly hinders all four probes in the absence of added salt, regardless of net molecule charge. The reduced D value does show a dependent on probe charge resulting in lower D values for the more highly charged At-C and At-E probes compared to At-A and At-E. Upon the addition of added salt, we see a corresponding increase in D for all probes measured due presumably to a systematic screening of the attractive probe-polymer electrostatic interactions. For At-A (0), this increase in D is observed until ~ 200 mM added NaCl concentration and then a plateau value is observed at $D \sim 120 \mu\text{m}^2/\text{s}$ which is still far reduced from the probe transport in water or 2% neutral polymer. At-C (-2) and At-E (-1) probe salt dependence of D is nearly identical with a continuously increasing D observed for added NaCl up to 400 mM before plateauing at $D \sim 95 \mu\text{m}^2/\text{s}$.

shows intermediate behavior with D continuing to increase until plateauing at 400 mM NaCl to D values nearly identical to the zwitterionic At-A probe. It is interesting to note how PVAm appears to have two characteristic crossover salt concentrations. A lower crossover for neutral, zwitterionic probe at ~ 200 mM and a higher crossover of ~ 400 mM added NaCl for all probe molecules with a net negative charge.

3.4 Conclusions

In vivo particle interactions with biological hydrogels are complicated and depend on particle size, charge density, sign and net magnitude of the charge particle.¹⁸⁷ Using FCS, we measured the transport properties of probe molecules with varying net molecular charge neutral and charged in semi dilute polymer solutions. These probe molecules have radii small compared to the correlation lengths within the polymer solutions. In neutral dextran, the particle transport properties can be understood from Stokes-Einstein using the experimentally measured microviscosity of the polymer solution. Diffusive behavior of the probes in semi dilute dextran solutions are nearly identical to dextran solutions above c^* . When the probe molecule can interact electrostatically with the polymer chains, we must account for possible attractive or repulsive charge-charge interactions. Using a reconstituted dextran polymer system, we have shown that transport of particles in repulsive semi dilute polymer solutions behaves similar to neutral solutions, whereas the attractive electrostatic forces between probe and polymer results in strong hinderance of the particle transport. These results indicate that nature uses this asymmetric behavior for particle interaction and their exchange between cells and their environments. Particle diffusivity depends on the probe charge in these dextran solutions, indicating the importance of electrostatic interactions responsible for particle transport. Using a biotinylated probe, we also observe additional non electrostatic biotin-dextran interactions resulting in decreased particle transport within the dextran solutions. All probes, regardless of charge, showed highly hindered diffusion in semi dilute PVAm solutions due to the high charge density of the polymer. Lastly, salt studies show the particle transport of probe molecules within the attractive semi dilute polymer solutions has a crossover behavior at a critical solution ionic strength the depends on the probe charge and polymer charge density.

Chapter 4: Particle transport in mixed-charged and polyampholytic polymeric solutions

4.1 Introduction

Biological hydrogels, such as mucus and the extracellular matrix, are complex macromolecular three-dimensional networks of biologically derived polymers that serve many important physiological roles *in vivo*. These functions range from lubrication^{43, 212-214} of tissue surfaces, to mechanical stability,²¹⁵⁻²¹⁷ to serving as protective selective filters^{10, 69, 218} controlling the passage of molecules and particles between organelles and cells while providing protection from pathogens and other nanoparticles. Biogels also represent another challenge for the delivery of nanotherapeutics that must be efficiently delivered to organelles or cells coated within a biogel matrix.^{18, 219-222}

Despite being over 90% water, the small amount of biopolymers inside the biogel dictate the transport properties of particles within the matrix.²²³ To perform these wide-ranging functions, the biopolymers within biogels are themselves complex, often inhomogeneous, containing different monomers that can repel or attract particles through electrostatics, hydrogen bonding or hydrophobic interactions. For instance, the extracellular matrix (ECM) is comprised of a mixture of proteoglycan polymers including collagen, fibronectin, tenascin, vitronectin, and laminin.^{82, 224, 225} The spatial relationship between laminin and collagen IV is maintained by a cross-linking molecule (nidogen) that connects different biopolymers of the matrix.²²⁶ This polymer-based heterogeneity stimulates cell adhesion, proliferation and is also crucial for proper communication between different cells in tissue development and maintenance.²²⁷⁻²²⁹ The transport of growth factors and distribution of the diffusing molecules, such as proteins and ions, depend on the shape of ECM.²³⁰⁻²³² Another important example of heterogenous charged based biopolymer is mucin biogels containing numerous acidic and basic amino groups which become positively or negatively charged based on the pH of the solution.⁶¹ Thus, molecules diffusing within biopolymers *in vivo* experience a heterogenous environment with mixed attractive and repulsive interaction sites that greatly control molecular transport.

Recent studies have shown that attractive and repulsive non-steric interactions, as well as steric and hydrodynamic effects, are important parameters for the transport properties of the particle within the biogel matrix.⁹ Electrostatic interactions have been found to be particularly important in the mobility of particles within the nuclear pore complex,^{25, 233-235} mucus^{68, 73, 174, 236, 237} the extracellular matrix^{84, 177, 238, 239} and bacterial biofilms.⁶⁴ Additionally, experiments on charged particles within biogels show different diffusive behavior depending if the particle is positively or negatively charged.^{65, 179, 187, 240} Despite its biological importance, there are still many things poorly understood about how biogels are capable of selective filtering under physiological conditions. Understanding these crucial processes is critical for development of therapeutics engineered to bind or penetrate to biogels, as well as, providing insight on how to control diffusive mobility of nanoparticles within artificial hydrogel systems.

In collaboration with the Netz lab, we previously combined course-grained simulations with experiments to investigate the effect of random distribution of attractive and repulsive electrostatic interactions sites within a polymer network on the diffusion of a -2 charged probe molecule.¹¹¹ For these studies, a high MW (500kDa) diethylaminoethyl-dextran (DEAE-Dextran(+)) and low MW (~20kDa) carboxymethyl-dextran [CM-Dextran(-)] were used to form mixed charged polymer solutions. Simulation work showed that due to the magnitude of the attractive interactions, charged particles are highly hindered in mixed cationic/anionic gels due to interactions with oppositely charged sites. Both experiments and simulations were in quantitative agreement and showed the particle transport in mixed gels was highly hindered, similar to diffusion in purely attractive gels, over a broad range of Dex(+)/Dex(-) compositions.¹¹¹ Later work by Hansing and Netz⁷⁰ showed that different trapping mechanisms were observed depending on the degree of spatial disorder within gels. In general, particles attracted to gel fibers are more strongly trapped in spatially disordered gels than in ordered gels. These results were consistent with experiments on particle transport within the ECM and mucus that controlled spatial configuration of charges in the biogel.^{68,241,242} Particle transport in biogels is also dependent on the total charge on the particle. Prior studies have shown that the transport of charged particles, of both algebraic signs, is highly reduced within ECM and mucus, whereas neutral and near-neutral charged particles can more freely diffuse through the matrix.^{69, 236, 243} The

importance of pH of mucus and charge on polymer networks can be well illustrated by understanding the entry of HIV into cervical mucus.^{244, 245} HIV (Human immunodeficiency virus) has a negative surface charge. *In vitro* experiments demonstrate that the acidity of the cervicovaginal fluid provides protection against HIV because the cell associated virions are inactivated at low pH. In contrast, the vagina becomes neutral during and after intercourse, since seminal plasma which is slightly alkaline changes vaginal pH to neutrality.^{79, 63, 246} Thus this heterogenous environment of cervical mucus greatly impacts the transport of HIV particles through the use of mixed attractive and repulsive interaction sites.

In this work, we wanted to explore how particle filtering within mixed-charge gels, gels comprised of positively and negatively charged polymers, compared to polyampholytic gel networks with both positive and negative charges on the same polymer chain (**Figure 4.1**). To investigate the effect of particle charge on transport within these charged hydrogels systematically, a series of probe molecules of similar size and core chemistry, but varying net molecular charge (0 to -3) were used. The translational diffusion coefficients of the probes are analyzed by fluorescence correlation spectroscopy (FCS) measurements. To ensure polymer chain entanglement, high molecular weight (500 kDa) dextrans were used at concentrations above polymer overlap. The model polymers studied for mixed-charged gels are amino dextran (Am-Dex(+)) and CM dextran (CM-Dex(-)). To create a polyampholytic dextran network, the primary amines of Am-Dex were reacted with succinyl anhydride to form a N-succinyl amino-dextran (NSA-Dex) with both cationic and anionic charges on the same polymer chain. Polyampholytic NSA-Dex was synthesized with 5-65% of the primary amines functionalized converting some amines to negatively charged succinyl groups. Similar to our previous study, we observe high particle filtering for negatively charged probe molecules in mixed 500kDa Am-Dex/CM-Dex polymer solutions over a broad range of compositions. Significant hindered diffusion persisted in mixed Am-Dex/CM-Dex polymer solutions even when the attractive Am-Dex comprised

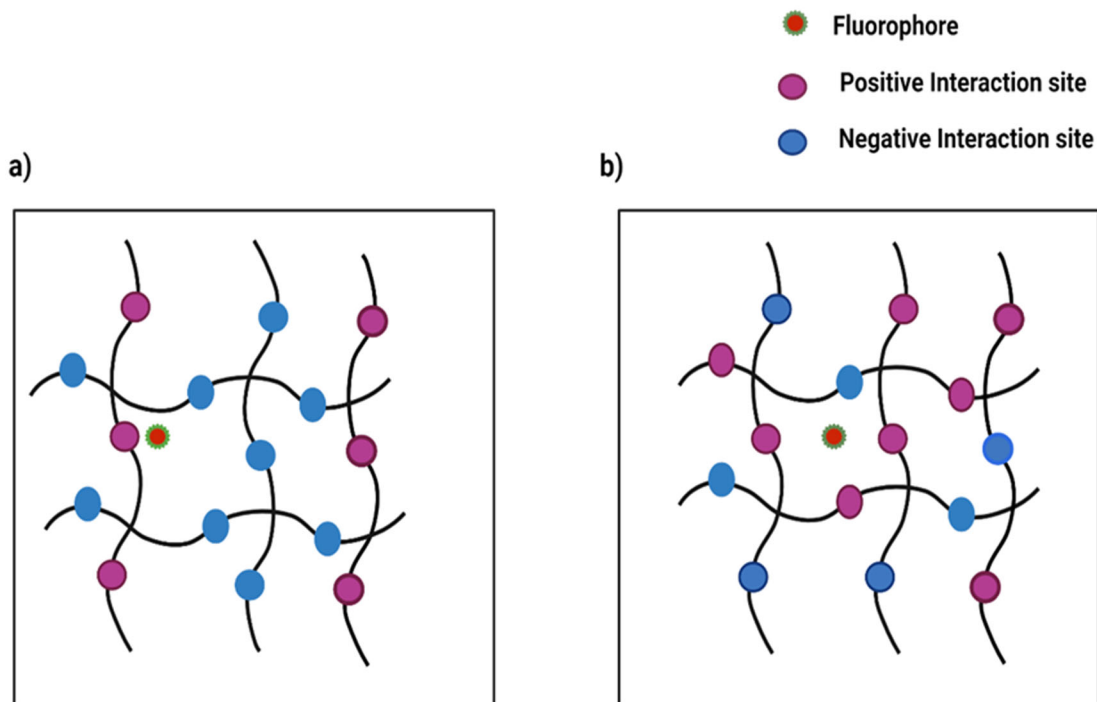


Figure 4.1 Particle mobility in mixed charged polymeric networks. a) Mixed gel systems with both positive and negative interaction sites on different polymer chains. The particles are trapped at the polymer vertices. b) Polyampholyte gel systems with both positive and negative interaction sites on same polymer chain.

only 20% of the matrix. More hindered probe diffusion was observed with increasing net probe charge. In contrast, net neutral probes were not hindered in the Am-Dex/CM-Dex polymer solutions and diffused similar to uncharged dextran solutions. In contrast, diffusion of negatively charged probes in the polyampholytic NSA-Dex solutions was observed to be less hindered at much lower ratios of cationic to anionic monomers. For example, conversion of 40% of the primary amines of Am-Dex to negatively charged succinyl groups was sufficient to lose attractive probe-gel interactions resulting in particle diffusivities comparable to that seen in the purely repulsive CM-Dex solution. Net neutral probes did not show hindered diffusion in NSA-Dex. Taken together, these results suggest a strong role for spatial ordering of charges for effective particle filtering within polymer gels.

4.2 Materials and methods

4.2.1 Materials: Amino dextran (Am-Dex(+), MW 500kDa) was purchased from Fina BioSolutions LLC and carboxymethyl-dextran, (CM-Dex(-), MW 500 kDa) was obtained from Sigma Aldrich (St. Louis, MO). Rhodamine 110 G (Abs/Em peaks, 496/520 nm) used in calibration of confocal volume were purchased from Fischer Scientific. A variety of water-soluble fluorescent probe molecules were purchased from Invitrogen (Carlsbad, CA). ATTO488-amine (AT-A, +0 charge), ATTO488-biotin (AT-B, -1 charge), and ATTO488-Carboxy (AT-C, -2 charge) were purchased from ATTO-TEC (Siegen, Germany). Alexa Fluor 488 carboxylic acid (AL-C, -3 charge) (Abs/Em maxima, 500/525 nm) was purchased from ThermoFisher Scientific (Waltham, MA).

4.2.2 Synthesis of N-succinylated amino dextran: Succinylated, or zwitterion-like aminodextran (NSA) was synthesized as follows; 0.6 gram of amino dextran (Am-Dex, 500kDa) was dissolved in 5 mL of sodium bicarbonate buffer (HCO_3^- , pH 9) and reacted with the desired mole ratio of succinic anhydride. The succinylation reaction proceeded for 6 hours at 65 °C and the final product, aminodextran, was purified by dialysis (membrane molecular weight cutoff = 3.5 kDa) against double distilled water for 24 hours with the water replaced every 4 hours. After dialysis, the product was frozen overnight and lyophilized for 24 hours. The dried product was placed in a -80 °C freezer for storage. Successful reaction and percent succinylation were determined by FT-IR and $^1\text{H-NMR}$ in D_2O , respectively. FTIR spectra of Am-dex and succinylated amino dextran (NSA) were analyzed using an iS50 FT-IR equipped with a diamond ATR within the range 400-4000 cm^{-1} equipped with OMNIC software. For NMR analysis, 5.0 mg of lyophilized polymer was dissolved in 1.0 mL D_2O and $^1\text{H-NMR}$ spectra were recorded using a 400 MHz Bruker Avance NEO spectrometer equipped with a smart probe and data was analyzed with Topspin 4.0.3 data analysis software. A series of percent modified NSA 5%, 40 %, 65 % modification of the total Am-Dex amines was used in this study.

NSA: $^1\text{H-NMR}$ δ (400 MHz, D_2O , TMS, ppm) : δ 2.5-2.7 (- CO-CH₂ -COOH); IR (wavenumber, cm^{-1}): 1726 (-COO stretch)

4.2.3 Preparation of dextran solutions: Dextran polymer stock solutions were prepared by dissolving solid dextran in 10 mM MES buffer (pH = 6.4) to a final concentration of 8 % w/v. Solutions were briefly vortexed and incubated overnight at room temperature to ensure homogeneity. Subsequent dilutions with 10 mM MES (pH = 6.4) were made from the stock solutions resulting in the desired final concentrations of polymer solutions. All the diluted polymer solutions were allowed to equilibrate for 24 h before use. For FCS experiments, different fluorescent probe molecules Atto 488 (At-A, (0), At-E (-1), At-C (-2) and Alexa 488, Al-C (-3) were prepared and mixed with polymer solutions to achieve a final probe concentration of ~5nM. Samples of probe molecules in polymer solutions were vortexed thoroughly and then incubated at room temperature overnight to ensure uniform distribution of probe molecules inside the polymer solution. Following incubation, 50 μ L of sample was deposited onto a glass coverslip to perform FCS measurement at room temperature. For mixed solutions of Am-Dex (+) and CM-Dex (-), stock solutions of each were added together to achieve the desired volumetric ratio of each dextran with respect to total dextran. For all mixed dextran solutions studied, the prepared mixtures resulted in homogeneous polymer solutions.

4.2.4 FCS set up: All FCS measurements were carried using a commercial dual-channel confocal fluorescent fluctuation system (ALBA FFS system, ISS, Champaign, IL). FCS experiments were made using a continuous wave 488 nm laser diode as an excitation source. The emitted light was then passed through a 514 nm long pass edge filter before detection of signals. Excitation light was directed into experimental samples through a Nikon Ti-U microscope (60 \times /1.2 NA water-immersion objective lens). The emission signal was recorded by separate Hamamatsu H7422P-40 PMTs. Confocal volume dimensions were determined through measurement of aqueous Rhodamine 110 at known concentrations. All FCS measurements were performed using 50 μ L of sample deposited on a glass coverslip (24 x 60 mm) with sampling times of 60 s. To ensure homogeneity of measurements within the solutions, all FCS results shown are taken as an average of at

least 9 measurements at various positions within the sample. FCS curves were analyzed using the VistaVision Software (ISS, Champaign, IL) to determine the diffusion coefficient with measured diffusion coefficients expressed as the mean \pm SD.

4.2.5 FCS data analysis: The principles of FCS have been described in detail in literature^{189, 190} and chapter 2 of this dissertation. Here, we provide a brief overview. FCS measures the fluorescence fluctuations emitted from labeled molecules moving in and out of a small ~ 1 fL confocal volume. The size of the effective illumination volume is fixed by the confocal detection optics and the excitation profile of the focused laser beam and characterized by measurements against standard Rhodamine 110 of known diffusion constant ($D = 440 \mu\text{m}^2/\text{s}$).¹⁹¹ For uniformly distributed fluorescent particles diffusing by Brownian motion, dynamic information can be determined from the intensity fluctuations by means of a time autocorrelation given by

$$G(\tau) = 1 + \frac{1}{N} \left(1 + \frac{\tau}{\tau_d}\right)^{-1} \left(1 + \frac{\tau}{\beta^2 \tau_d}\right)^{-\frac{1}{2}} \quad (1)$$

where N is the average number of molecules in the detection volume, τ is the delay time, τ_d is the characteristic diffusion time, or the average passage time of a molecule through the confocal volume, and β is the structure parameter ($= z_0/\omega_0$) is the ratio of the axial to the radial dimensions of the confocal observation volume as determined by calibration measurements using dye with known diffusion constant. Here, β was fixed to 10 in all fits, based on results from calibration measurements with Rhodamine 110. Confocal volume with radial and axial $w_0 = 0.356 \mu\text{m}$, $z_0 = 3.56 \mu\text{m}$ respectively was determined via calibration of rhodamine 110 ($D = 440 \mu\text{m}^2\text{s}^{-1}$) to confirm consistency in confocal beam geometry throughout the experiments. Acquisition time of 30 s, laser intensity 65 % (Power= 193 μW) were used. Cross correlation with both detectors minimizes the effects of detector after-pulsing in the resulting autocorrelations. The translational diffusion coefficient D ($\mu\text{m}^2/\text{s}$) can be calculated from τ_d and the radial width using

$$\tau_d = \frac{\omega_0^2}{4D} \quad (2)$$

For spherical particles, the diffusion coefficient D follows from the hydrodynamic radius, R_h , in solution and can be calculated by the Stokes-Einstein relation $D = k_B T / 6\pi\eta R_h$, where k_B is the Boltzmann constant, T is the temperature, and η is the viscosity of the medium.

4.3 Results and Discussion

4.3.1 Charged dextrans structure and properties

For this study on probe transport, cationic amino dextran (Am-Dex) and anionic carboxy methyl dextran (CM-Dex) of similar molecular weight of 500 KDa were used. Both dextrans are branched polysaccharide consisting primarily of linear glucose chains linked by α -D-(1-6 linkages) with a small (~5%) degree of branching (typically only 1-2 glucose units in length). High molecular weight dextrans, however, may possess longer branches. These two charged dextrans differ in their functionalization with Am-Dex being functionalized with primary amines while CM-Dex is functionalized with O-carboxymethyl groups as shown in **Figure 4.2**. At neutral pH, Am-dex has approximately 250 amine groups per polymer whereas CM-Dex has approximately 555 O-carboxymethyl groups per polymer. This is a relatively low chain charge density resulting in Am-dex with approximately one charge per ten glucoses while CM-Dex has one charge per five glucoses. For a neutral, uncharged 500kDa dextran polymer, we estimated the radius of gyration as $R_g = 18$ nm and overlap concentration $c^* = 0.024$ g/cm³ using methods described previously in chapter 3.3.4. Due to repulsive self-similar charge along the polymer chain, charged dextrans, such as Am-Dex and CM-Dex, would be expected to have a larger R_g and thus lower c^* than uncharged dextrans for pure solutions. The estimates above therefore likely represent an upper bound for c^* for our charged dextrans (Am-Dex/CM-Dex). In this work, we perform all experiments at ≥ 2 wt% solutions, thus above c^* and in the concentrated regime where dextran chains are entangled to form a physically crosslinked polymer network.

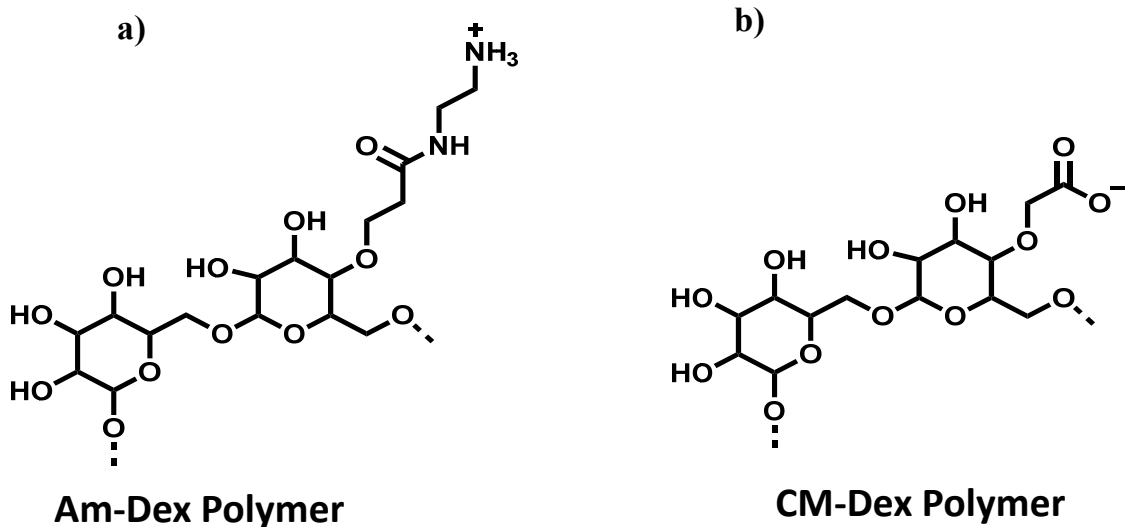


Figure 4.2 Chemical structures at neutral pH a) positively charged amino dextran (Am-Dex) b) negatively charged carboxymethyl dextran (CM-Dex)

4.3.2 Probe transport in charged dextran solutions

Before examining the transport properties of our probe molecules in mixed-charge gels, we first focused on measurements of the translation diffusion coefficient in pure charged dextran solutions. We used the same set of probe molecules described in chapter 3 with similar size and core chemistry but varying net molecule charge from net neutral to -3. Plotted in **Figure 4.3** is the translation diffusion coefficient, as measured by FCS, as a function of polymer concentration for At-A (0), At-E (-1), At-C (-2) and Al-C (-3). As polymer concentration increases we see the translation diffusion coefficient, D , for all probes decrease by $\sim 31\%$ by 8 wt% in the repulsive CM-Dex polymer solutions. These D values are nearly identical to that observed in 500kDa uncharged Dextran (data not shown) and D measured in 20kDa CM-Dextrans resulting in semidilute polymer solutions from Chapter 3. As our probe molecules are small relative to the correlation lengths in our dextran solutions, their diffusion behavior is dominated by simple steric and hydrodynamic effects in CM-Dextran.

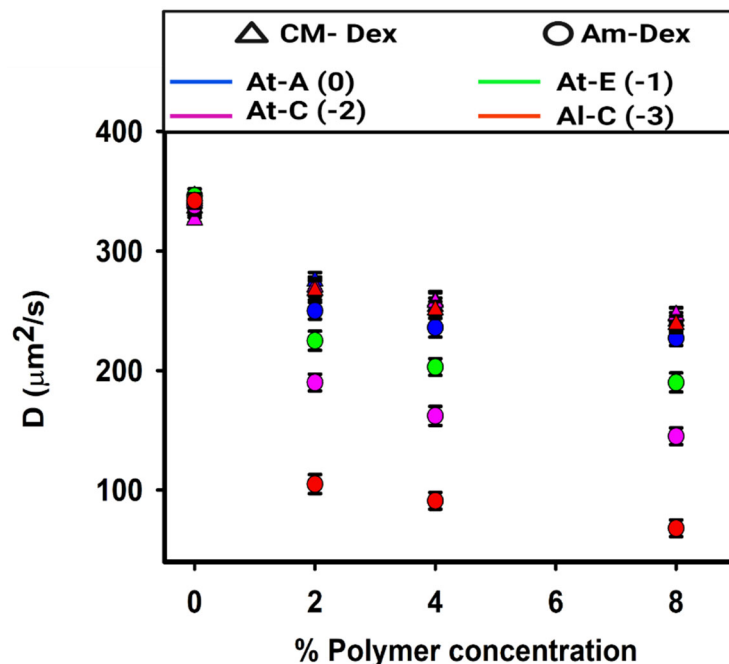


Figure 4.3 Translational diffusion coefficient D plotted as a function of polymer concentration for four different charged probe molecules in Am-Dex(+) (circle) and CM-Dex(-) (triangle) polymer solutions. Probes studied include (blue) At-A (0), (green) At-E (-1), (pink) At-C (-2) and (red) Al-C (-3). Particle transport within repulsive CM-Dex(-) network is nearly identical to uncharged Dextran solutions and dominated by steric and hydrodynamic effects. Uncharged At-A probe diffusion in Am-Dex is identical to CM-Dex. Particle transport for all negatively charged probes was hindered in Am-Dex due to attractive electrostatic interactions dependent on both probe net charge and polymer concentration.

For the cationic Am-Dex solutions, attractive electrostatic interactions between the particle and oppositely charged polymer network results in highly hindered diffusion that varies with probe net charge. For highly charged probes, particle diffusion can be highly hindered even at low polymer concentration. For example, the relative diffusivity of Al-C(-3) decreased by ~65% in 2% Am-Dex relative to 2% CM-Dex. Lower probe net charge results in less hindered particle transport. At-E(-1) and At-C(-2) diffusion in Am-Dex is only reduced by 11% and 24%, respectively, for 2 wt% solutions. The measured D values for all charged probes decreases more with increasing polymer concentration. This behavior observed in Am-Dex is comparable to that previously observed for a -2 probe in 500 kDa DEAE-Dex(+) that contained charged quaternary amines along the dextran

backbone.¹⁰⁹ In contrast, the net neutral At-A probe diffuses nearly identically in both CM-Dex and Am-Dex consistent with minimal electrostatic interaction with the zwitterionic probe.

4.3.3 Probe transport in mixed charged gels

Next, we moved to experiments of negatively charged probe diffusion within mixed-charged gels (i.e., gels comprised of a mixture of positively charged Am-Dex and negatively charged CM-Dex chains). Characteristic normalized fluorescence autocorrelation functions in pure attractive and repulsive dextran solutions and a mixed charge dextran solution ($C_{\text{dex}(-)}/C_{\text{total}} = 0.45$) are given in **Figure 4.4a**. Even with a nearly 50/50 composition of Dex(-)/Dex(+), the characteristic diffusion time is nearly identical to pure Dex(+) solutions. **Figure 4.4b** plots the relative diffusivity of charged probes for varying mixtures of CM-Dex(-) and Am-Dex(+) defined by the ratio of Dex(-) to total dextran concentration ($C_{\text{Dex}(-)}/C_{\text{total}}$). Here the total dextran concentration is maintained at 4 or 8 wt% as indicated in **Figure 4.4b**. Shown are D values for At-E(-1) and Al-C (-3) probe molecules normalized relative to their diffusion in MES buffer (D_0). For $C_{\text{dex}(-)}/C_{\text{total}} = 0$, we have strong attractive electrostatic particle–gel interactions resulting in strongly reduced diffusivities for both At-E and Al-C probe molecules relative to diffusion in buffer. For $C_{\text{dex}(-)}/C_{\text{total}} = 1$, we have purely repulsive electrostatic particle–gel interactions resulting in diffusivities nearly identical to that observed in uncharged 500 kDa Dextran solutions. In agreement with our previously published results with mixed DEAE-Dex(+)/CM-DEX(-) solutions, we also observe in our Am-Dex(+)/CM-Dex(-) solutions that negatively charged probes in mixed charge dextrans show highly hindered diffusion over a very broad range of compositions. Mixtures containing as much as 50% repulsive Dex(-) chains, still significantly hinder probe diffusivity nearly identical to purely attractive Dex(+) solution. Even at $C_{\text{dex}(-)}/C_{\text{total}} = 0.8$, relative diffusivities are observed to be ~40% lower than relative diffusivity measured in pure Dex(-).

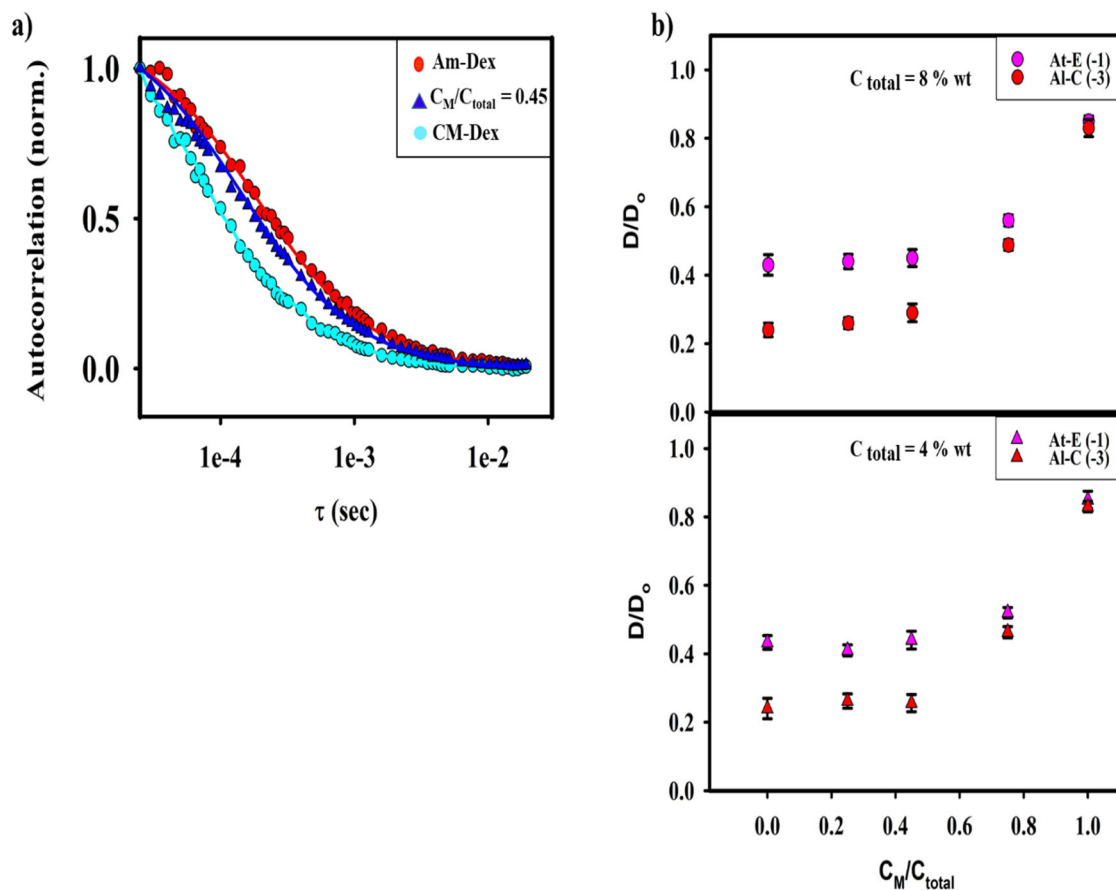


Figure 4.4 Transport properties of two negatively charged probes in mixed gel solutions. (a) Characteristic normalized FCS autocorrelation curves for the diffusion of negatively charged probes Al-C (-3) through a 10 mM MES buffer (pH =6.4) solution of 4 wt% total dextran concentration of a mixed charge dextran solution $C_{dex(-)}/C_{total} = 0.45$ and purely attractive Am-dex, purely repulsive CM-dex solutions. The autocorrelation plots are fitted with single component fits (solid lines) to obtain the translational diffusion coefficients. b) The diffusivity for negatively charged probes At-E (-1) and Al-C (-3) of oppositely charged Am-Dex and CM-Dex as a function of the CM-Dex to total dextran mass concentration ratio. The total mass concentration for polymer gels 4 wt% and 8 wt% were plotted.

Interestingly, this crossover behavior is fairly similar for both -1 and -3 charged particles. Prior experimental studies have shown that particles in biogels, such as ECM and mucus, experience a heterogenous environment where transport of particles is controlled by magnitude of the net charge rather than the sign as key determinant.^{61, 69} Our results are

also consistent with heterogeneous biopolymer gels, consisting of different attractive and repulsive functional groups, still performing as highly efficient filters for interacting particles. Even with relatively few attractive interaction sites within the mixed gel solution, we can significantly hinder the diffusion of oppositely charged particles leading to strong interaction filtering. Hansing and Netz showed in further simulations that mixed gels could have three distinct trapping mechanisms that are dependent on the spatial order of charges within the gels.¹¹¹ Specifically, they showed that for attractive electrostatic particle-gel interactions, particles are more strongly trapped in spatially disordered gels compared to ordered gels. Motivated by these results, we next turned our attention to probe transport in ampholytic dextran solutions to compare to these mixed-charge solutions.

4.3.4 Synthesis and characterization of N-succinylated amino dextran (NSA-Dex)

To synthesize polyampholytic dextran, with varying degrees of positive and negative charges, we synthesized a series of N-succinylated amino dextran (NSA-Dex) polymers by reaction of Am-Dex with succinic anhydride in DMSO (**Figure 4.5a**). This reaction converts some fraction of primary amines to negatively charged succinate groups. The degree of substitution was controlled by the mole ratio of succinic anhydride to amino dextran. Reactions with mole ratio 1:0.2, 1:1, and 1:2 were performed resulting in a corresponding percent modification in NSA of 5%, 40%, and 65% as determined by ¹H-NMR (**Figure 4.5b**). These NSA-Dex polymers were used for FCS studies of probe diffusion in polyampholytic polymer networks for comparison to the earlier mixed-charge dextrans solutions made by mixtures of Am-Dex and CM-Dex. NSA-Dex characterization was done by using FT-IR for qualitative determination and quantification by H¹-NMR analysis as described below.

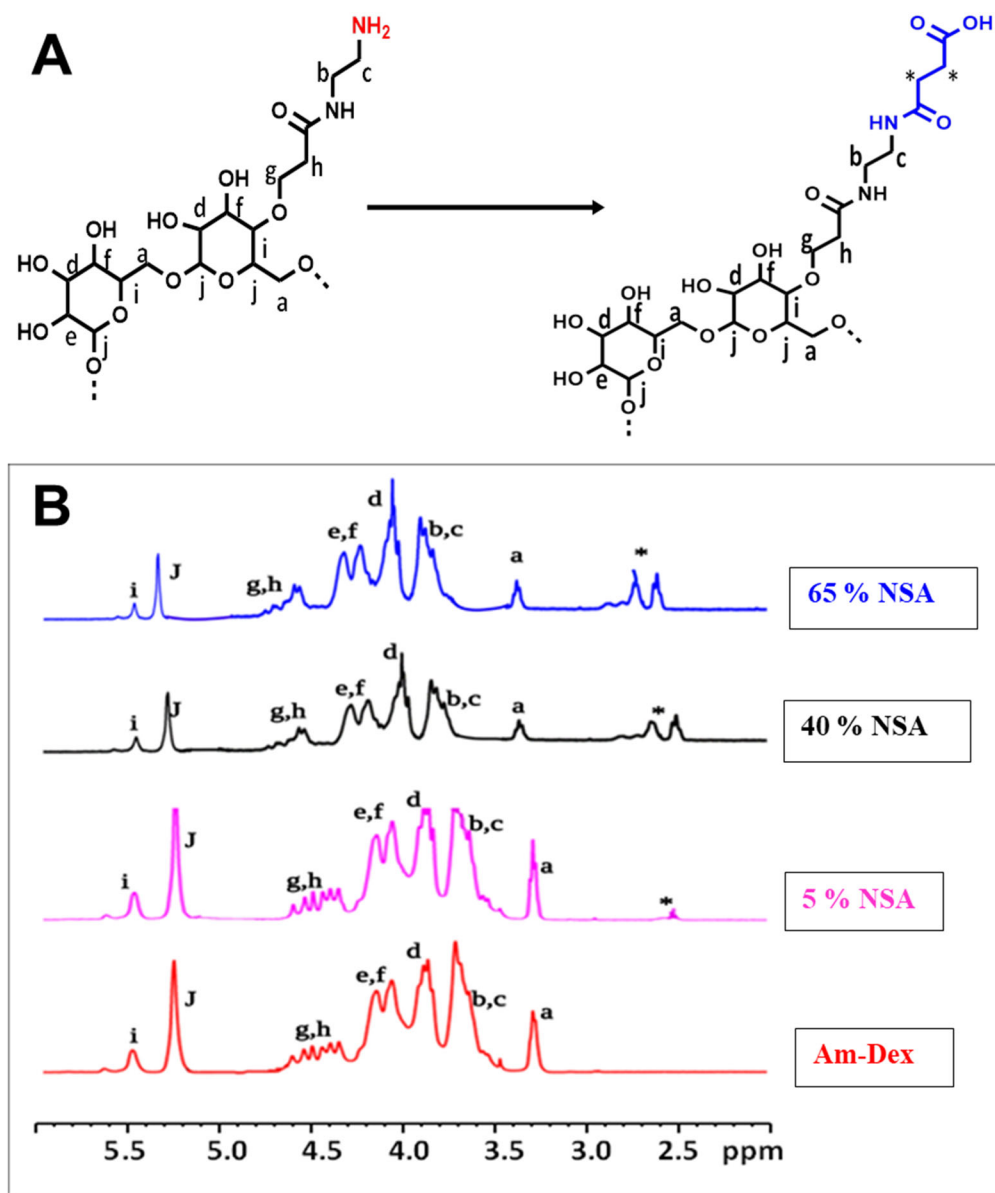


Figure 4.5 (A) NSA-Dex reaction scheme and (B) $^1\text{H-NMR}$ spectrum for amino dextran and succinylated products obtained for 5 %, 40 % and 65 % modifications.

4.3.4.1 ¹H-NMR spectra of Am-Dex and NSA-Dex polymers

Am-Dex and NSA-Dex were characterized by ¹H-NMR analysis to quantitatively determine the degree of substitution. Based on the ¹H-NMR spectrum of Am-Dex shown in **Figure 4.5**, methyl protons were observed at chemical shift values 3.3 ppm, whereas the chemical shifts at 3.7-4.5 ppm corresponds to the H₂-H₆ of glucosamine and N-acetyl methyl protons. The anomeric protons for Am-Dex and NSA-Dex were observed by ¹H-NMR at chemical shift values 5.0-5.4 ppm (**Figures 4.5B**). Characteristic NSA-Dex peaks were observed at chemical shift value 2.5 - 2.7 ppm corresponding to the proton signals from methylene groups of N-succinylated amino-dextran. These characteristic peaks were observed for all three different molar ratios of NSA-Dex indicating successful succinylation. Relative peak areas can be used to calculate the percent succinylation in these NSA-Dextrans. Different degrees of modification were determined for each molar ratio synthesis performed. These results are tabulated in **Table 4.1**. The degree of substitution is calculated using the integral of peaks at chemical shift values 2.5 ppm-2.7 ppm, and at chemical shift values 3.5 ppm-4.5 ppm. The calculated degree of substitution varied from 5% to 65% at these different feed mole ratios.

Table 4.1. Percent degree of substitution for NSA-Dex synthesized from different mole ratios of Am-Dex and succinic anhydride

Am-Dex to Succinic Anhydride mole ratio	Peak Area at 2.7 ppm	%DS (Degree of substitution)
1:0.2	103	5 %
1:1	780	40 %
1:2	1568	65 %

4.3.4.2 FTIR spectra of Am-Dex and NSA-Dex polymers

FT-IR spectrum of Am-Dex and synthesized NSA-Dex were obtained and shown in **Figure 4.6**. The characteristic peaks of Am-Dex include an O-H stretch at 3316 cm^{-1} , a C-H stretch at 2927 cm^{-1} , an NH_2 deformation at 1644 cm^{-1} , and a C-H bend at 1351 and 998 cm^{-1} . After the introduction of succinate groups, NSA-Dex showed characteristic absorption bands of Am-Dex, as well as a new absorption band observed at 1726 cm^{-1} corresponding to the symmetric stretch of $-\text{COO}$ group. This new absorption band is indicative of successful conversion of amines to succinate groups and observed in all NSA-Dex samples.

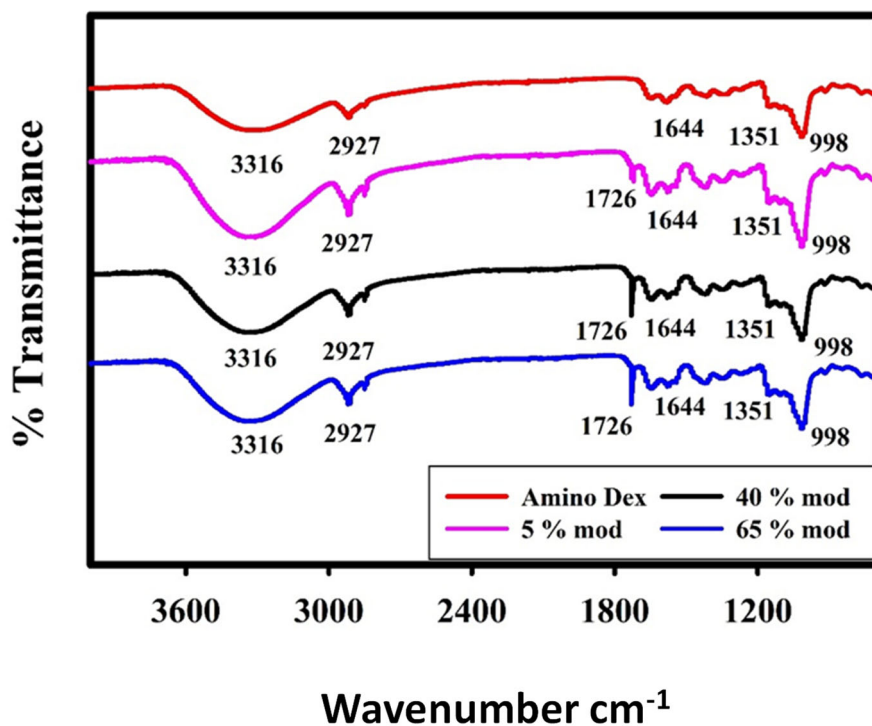


Figure 4.6 FTIR spectrum for amino dextran and succinylated NSA-Dex products.

4.3.5 Determination of particle transport in polyampholytic dextran solutions

Next, we examined the particle diffusivity of our charged probes in the polyampholytic NSA-Dex solutions for comparison to the previous mixed-charged dextran solutions. For our studies, 0% to 65% of the primary amines of Am-Dex were succinylated. **Figure 4.7** shows characteristic normalized autocorrelation functions for the negatively charged Al-C (-3) probe dye in a 2 wt% solution of Am-Dex(+), CM-Dex(-), and the 40% modified mixed charge NSA-Dex. In contrast to the mixed charge gels, where hindered diffusion was observed even with 80% of the gel composition consisting of repulsive Dex(-), in polyampholytic NSA-Dex the conversion of 40% of amines to negative charged succinyl groups is sufficient to greatly reduce attractive particle filtering. Here the characteristic dwell time for Al-C (-3) in 40% NSA-Dex is within ~5% of the dwell time observed in

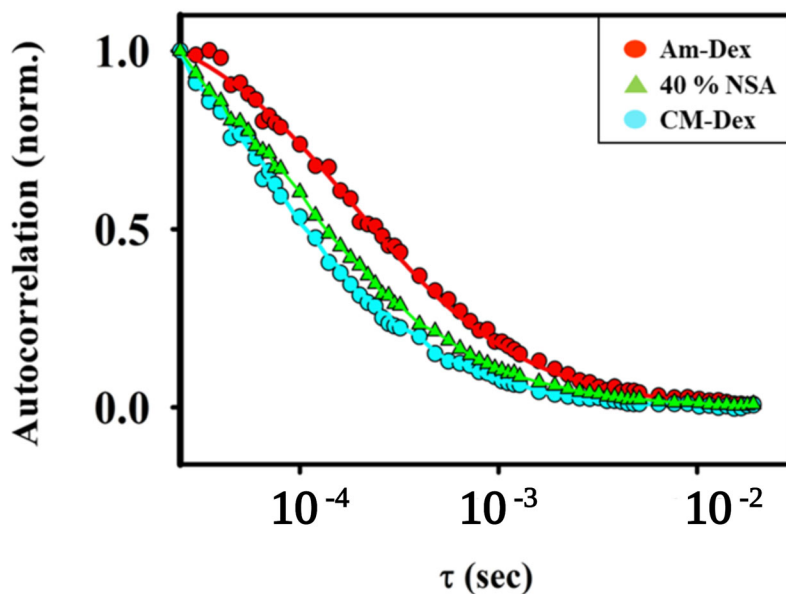


Figure 4.7 Normalized FCS autocorrelation curves for Al-C (-3) probe in 2 wt% polymer solutions of Am-Dex(+), CM-Dex(-) and 40% modified NSA-DEX in 10 mM MES buffer (pH 6.4). In contrast to mixed charged gels, where compositions as high as 80% Dex(-) showed hindered diffusion, 40% NSA-Dex shows particle diffusivities comparable to purely repulsive CM-Dex solutions.

purely negatively charged CM-Dex hydrogels. In **Figure 4.8**, we plot the relative diffusivity (D/D_0) for Al-C (-3) for pure Am-Dex and all three synthesized NSA-Dex gels for polymer concentrations ranging from 0-8 wt%. While low degrees of succinylation (e.g. 5%) do not alter the particle filtering capacity of NSA-Dex, by 40% modification we see a loss of most of the attractive electrostatic interaction between the charged dextran network and the negative probe. Relative diffusivities for both 40% and 65% are nearly identical to that observed in uncharged or purely negative charged dextran solutions dominated by only steric interactions. For example, Al-C(-3) translation diffusion coefficient is $298 \pm 5 \mu\text{m}^2/\text{s}$ in MES buffer. In 2 wt% solutions of Am-Dex(+) or 5% succinylated NSA-Dex, D is reduced by over 60% to $D \sim 113 \mu\text{m}^2/\text{s}$. In contrast, for 2 wt% solutions of 40% and 65% modified NSA-Dex, D is only reduced $\sim 12\%$ again comparable to the reduced diffusivity observed from uncharged or repulsive dextran solutions at the same polymer concentration.

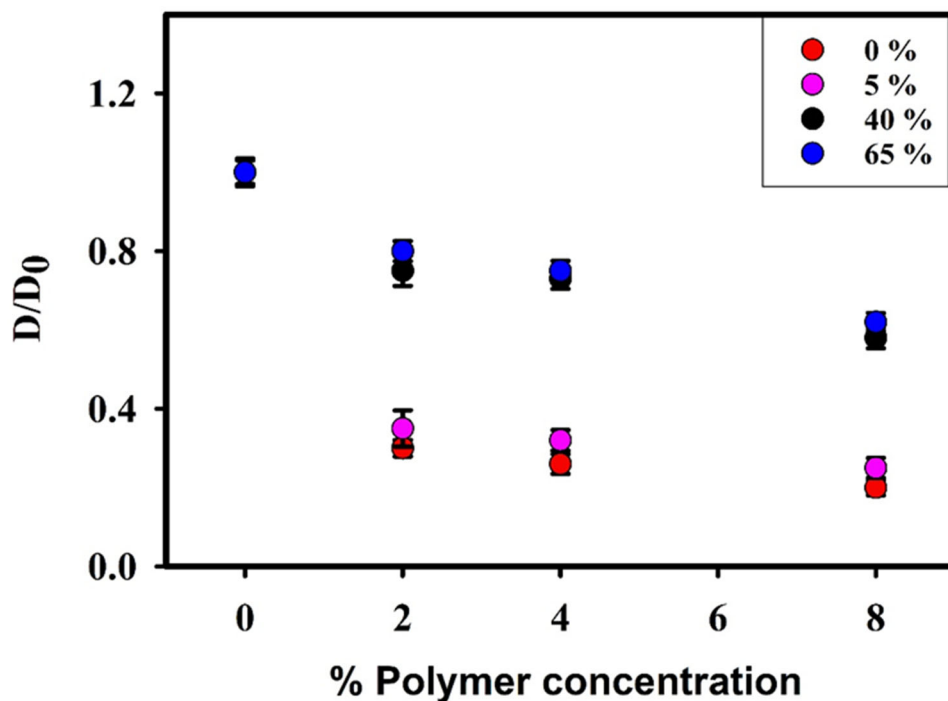


Figure 4.8 Relative diffusivity (D/D_0) as a function of polymer concentration for Al-C(-3) probe diffusion with Am-Dex(+) and various polyampholytic NSA-DEX solutions. Functionalization of 40% of the Am-Dex amines is sufficient to eliminate particle filtering due to attractive electrostatic interactions.

For Al-C in 65% NSA-Dex, D is $262 \pm 6 \mu\text{m}^2/\text{s}$ compared to $274 \pm 5 \mu\text{m}^2/\text{s}$ in pure CM-Dex(-) at the same 2 wt% weight percent. This behavior may suggest that the spatial ordering of the charges in polyampholytic dextran are resulting in a different trapping mechanism when compared to the mixed charge gels. The alternation of charges along a single polymer chain could lead to more localized charge neutralization. In addition, the charge density within the polyampholytic gels would be expected to be lower with only ~ 1 charge per 10 glucoses due to the degree of amidation in the original Am-Dex polymer. The mixed charged gels would therefore be expected to have more charges in the same volume inside the matrix as both Am-Dex and CM-Dex maintain their charges. This lower degree of total charges, and possible local charge neutralization, in the polyampholytic NSA-Dex may explain the lower sensitivity to the attractive probe-charge interactions when compared to mixed-charge polymer solutions.

4.4 Conclusion

Inside the human body, many particle-network interactions are complex and heterogeneous where transport through the networks depends upon the particle size, charge distribution and various other factors. This complexity of interactions, however, enables these biogels to function as selective filtering barriers for the transport of biomolecules or particles *in vivo*.^{61, 69} The goal of the project was to comparatively investigate charged particle diffusion through mixed-charge polymer gels with particle transport in polyampholytic gels where both positive and negatively charged functionalities coexist on the same polymer chain. Branched functionalized polysaccharide dextran polymers Am-Dex(+) and CM-Dex(-) were chosen for these model studies. Taken together, our results show significant differences in particle transport behavior are observed inside mixed-charge polymer networks compared to polyampholytic polymer networks. Selective particle filtering was observed in these mixed-charge dextran solutions over a broad range of compositions in both 4 and 8 wt% solutions. Even with only 20% of the gel comprised of Am-Dex(+) was sufficient to hinder probe diffusion of both -1 and -3 charged probe molecules significantly. In contrast, polyampholytic NSA-Dex showed a loss of hindered diffusion at much lower ratios of positive to negative charge. By 40% succinylation,

NSA-Dex shows no significant attractive electrostatic contribution between the probe and the polymer network resulting in the negatively charged probes diffusing in a manner nearly identical to that observed in neutral or purely repulsive, negatively charged dextran networks. Net neutral probe molecules showed no electrostatic interaction with mixed-charged polymer networks nor polyampholytic networks. These results suggest not only is the particle charge of the probe molecule important but also the composition and spatial configuration of the charges along the polymer network chains are critical to understanding particle transport and penetration within charged polymeric solutions.

Chapter 5: Constrained particle transport within phase-separated liquid droplets of tau protein

The central structural and functional component of the human nervous system are neuronal cells which transmit and receive chemical and electrical signals through axons and dendrites.²⁴⁷ The morphological differentiation of a neuron involves cytoskeletal rearrangements stabilized by microtubules in specific directions. Tau protein is a microtubule-associated protein (MAP) known to play an important role in microtubule assembly, neuronal development, and neuronal polarity.²⁴⁸ In the case of microtubules, tau both promotes and stabilizes their formation. In human brain, tau concentrations are highest in the axons of neuronal cells at $\sim 2 \mu\text{M}$.²⁴⁹ Tau is also present, but less abundant, in the spinal cord and peripheral nervous system.²⁵⁰

5.1 Structure and function of tau

Tau structure can be divided into four functional domains: the projection domain on the N-terminus [Tau(1-165)], a proline-rich region (PRR) domain [Tau(166-242)], the microtubule binding region (MTBR) [Tau(243-367)], and a C-terminal domain [Tau(368-441)].²⁵¹ Each of these regions have distinct roles. For example, the projection domain is proposed to be involved in interaction with cytoskeletal proteins, determines the spacing between axonal microtubules, and binding of heparin through the KKXK sequence.²⁵²⁻²⁵⁴ In the PRR, the PXXP motif is thought to be critical for its interaction with proteins containing SH3 domains.^{255, 256} There are 6 isoforms of tau protein in human brain, encoded by a single gene, located on chromosome 17 (**Figure 5.1a**).²⁵⁷ These isoforms arise from alternative splicing of tau transcripts by including or excluding exons 2, 3, and 10.²⁵⁸ Human tau isoforms differ in the presence of 0, 1 or 2 inserts in the N-terminal domain and the presence of three (3R) or four (4R) repeat sequences in the MTBR.²⁵⁸⁻²⁶⁰ The MTBR domain has partially repeated amino acid sequences named R1, R2, R3 and R4. 3R tau indicates the absence of the R2 sequence in the MTBR domain. **Figure 5.1b** shows the full sequence of the longest isoform of tau found in the human brain (2N4R).³

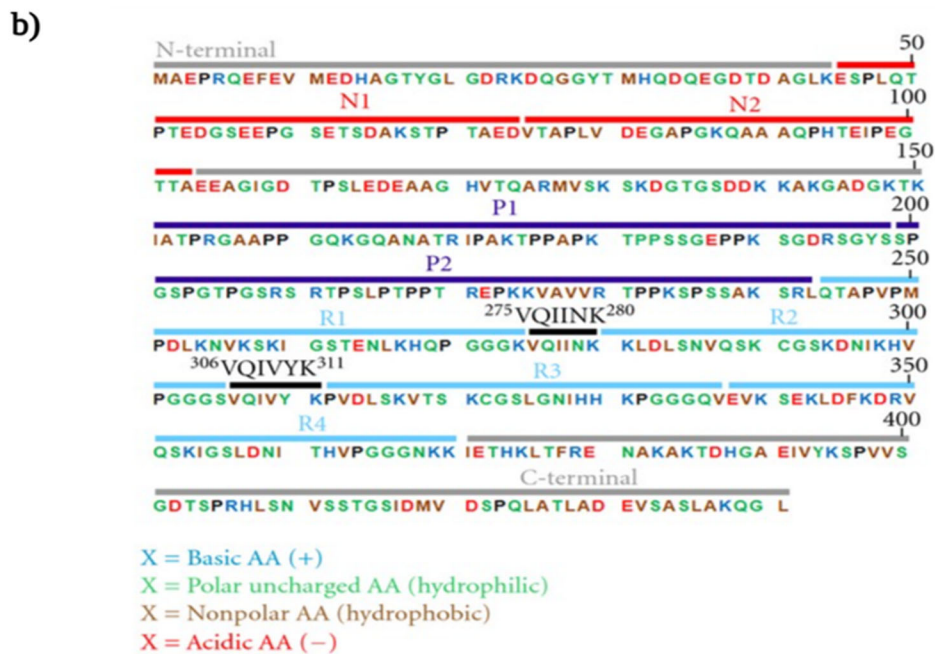
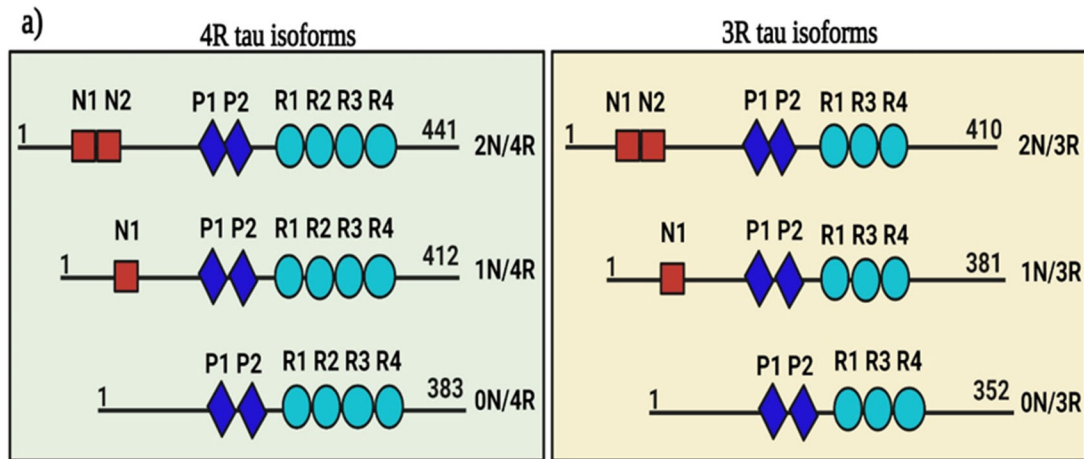


Figure 5.1 Tau isoforms and amino acid sequence of tau 441 (a) Tau is encoded by MAPT gene, alternative splicing of MAPT results in six different isoforms which are based on number of N-terminal inserts (0N,1N,2N) and microtubule binding repeats (3R,4R). (b) Amino acid sequence of the tau 441, containing projection domain with 2 N-terminal and proline rich polypeptide sequences, R1-R4 microtubule binding regions flanked by sequences with β structure (275-280, 306-311).³ (Reprinted sequence with permission from Krestova, M.; Garcia-Sierra, F.; Bartos, A.; Ríchny, J.; Ripova, D., Structure and Pathology of Tau Protein in Alzheimer Disease. *International journal of Alzheimer's disease* **2012**, 2012, 731526.

Tau is an intrinsically disordered protein (IDP) that has differences in the primary structure that arise due to the presence or absence of specific exons.²⁵⁸ Tau-441, or 2N4R, is the longest isoform of tau containing two amino terminal inserts and all four microtubule binding repeats resulting in a protein with 441 residues. Tau-441 contains exons 1-5, 7, 9-12 and low portions of hydrophobic residues.²⁶⁰ Tau-441 lacks a dominant stable conformation with only transient secondary structure present. For example, tau has been reported to form only local secondary structures including polyproline II helices in the PRR²⁶¹ and β -strands in the MTBR²⁶². Post-translational modifications (PTMs), including phosphorylation, O-glycosylation, acetylation, and deamidation, alters the protein charge of tau significantly.^{263,264} The most studied PTM for tau involves the regulation of phosphorylation by kinases and phosphatases (**Figure 5.2a**). Tau-441 has 79 putative serine/threonine phosphorylation sites,²⁵⁵ that be phosphorylated or dephosphorylated, respectively by kinases and phosphatases.^{265, 266} Kinases are further grouped as proline directed and non-proline directed.²⁶⁷⁻²⁶⁹ In many cases, microtubule binding to tau is controlled by the degree of phosphorylation therefore regulating tau function. In this manner, tau facilitates tubulin assembly²⁷⁰ and thereby stabilizes polymerized microtubules and promotes nucleation.²⁷¹⁻²⁷³ Biochemical studies have shown that tau binding to microtubule^{274, 275} as depicted in **Figure 5.2 b**, through the proline rich region (PRR) and R repeat domains.

5.1.1 Liquid-Liquid phase separation (LLPS)

Cells are organized into subcellular compartments, or organelles. Cells use compartments to control local concentrations of small molecules, proteins and other biopolymers thus controlling the biochemistry inside the compartment. Most commonly, these organelles have lipid layer membranes such as mitochondria²⁷⁶ and lysosomes.²⁷⁷ However, many organelles do not have a lipid layer membrane and are therefore referred to as non-membrane bound organelles. These phase-separated membraneless organelles are able to assemble, fuse, and disassemble rapidly in the cytoplasm.³¹ These properties suggest they are liquid-like compartments with viscoelastic properties such as plasticity and

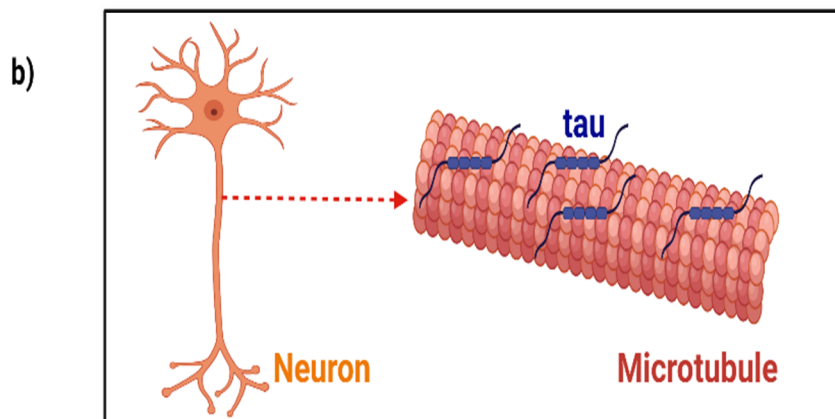
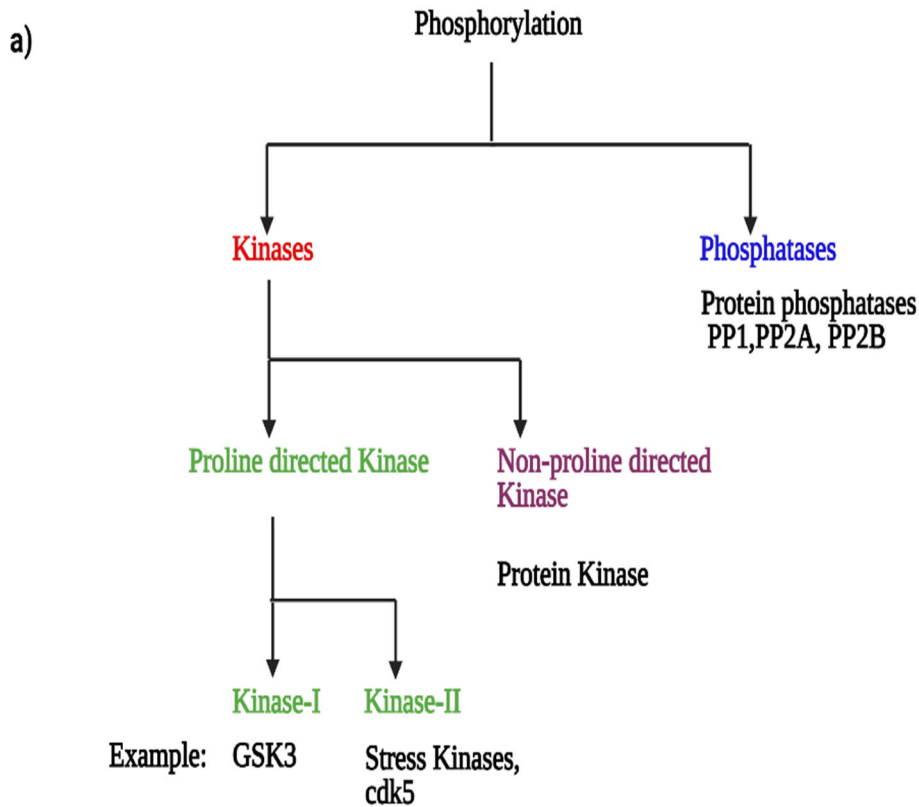


Figure 5.2. Phosphorylation of tau (a) Flow chart showing the classification of posttranslational modification of tau by kinases and phosphatases with some of the examples playing an important role in phosphorylation under physiological and pathological conditions. Stabilization of microtubules of neuron by tau b) Schematic representation showing neuronal cytoskeletal arrangement involving microtubules which are stabilized by tau protein binding.

flexibility.^{31, 278} Common examples of membraneless organelles include nucleoli, centrosomes, stress granules, Cajal bodies, and P granules. Membraneless organelles often have multiple biological functions. For example, P granule formation helps in the establishment of gradients of RNA transcription factors²⁷⁹ concentrating RNA binding proteins in stress granules,²⁸⁰ as well as aids in the storage of materials and stress response by the cells.^{281, 282} The nucleolus is a membraneless organelle and the largest nuclear body in eukaryotic cells. Recent work shows the nucleolus functions as a hub for many nuclear functions, including the 3D organization of the genome, enabled by the transport of proteins and nucleic acids between the nucleolus and nucleoplasm.^{283, 284}

The formation of non-membrane compartments is driven by multivalent interactions in nucleic acids and proteins.^{285, 33} Intrinsically disordered regions, or low-complexity domains, of the proteins facilitate the phase separation process, and drive assembly of the liquid drops.^{29, 30, 108} Also critical to droplet formation are temperature and ionic strength,¹⁰⁸ which affects the entropy and electrostatic interactions of the condensate systems, respectively. Post-translational modifications (PTMs), in particular the phosphorylation of proteins, impacts the charge state of roteins altering their electrostatic interactions. PTMs in tau have been shown to contribute to a loss of function and an inability to undergo the phase separation process.²⁸⁶⁻²⁸⁸

Many intrinsically disordered proteins (IDPs) are known to undergo liquid-liquid phase separation (LLPS) resulting in the formation of membraneless organelles. LLPS of proteins results in the formation of a concentrated protein-rich phase and a dilute protein-depleted phase through a process known as coacervation.^{289, 290} Coacervation can occur generally between two oppositely charged polyelectrolytes (complex coacervation)²⁹¹ or from self-association (self-coacervation).²⁹² In protein LLPS, complex coacervation typically arises from interactions with the protein and RNA or other polyanions present.

Tau is a highly soluble IDP protein, containing numerous hydrophilic and charged residues. Tau is also a polyampholytic protein consisting of many basic amino acids in the MTBR and PRR regions, while the N-terminal is rich in acidic residues. Classification of Intrinsically Disordered Ensemble Relationships, or CIDER, is a webserver that provides

straight-forward analysis of IDP properties that are derived from the protein primary sequence.²⁹³ In **Figure 5.3**, CIDER was used to generate a net charge per residue (NCPR) plot for tau 441 with a five-residue window at neutral pH. Charge distribution analysis of tau441 reveals a highly polarized IDP with negatively charged residues concentrated on the N-terminal (residues 1-117) and positively charged residues concentrated on the remainder of the sequence (residues 118-402). The residues from 402-441 have a net negative charge. These results are identical with previous CIDER analyses of tau441.²⁹⁴ Despite containing many charged amino acid residues, the net charge of tau441 is relatively modest at +2.5.²⁹⁵ In recent years, it has been shown that droplet-like tau can be observed in neurons and other cells as well as formation of tau441 droplets ex vivo under cell physiological conditions.²⁸¹ Tau has been shown to undergo LLPS by both self-coacervation^{294, 296, 297} and complex coacervation.^{298, 299} Wegmann et al. proposed that phase-separated tau droplets may be an intermediate toward tau aggregate formation.²⁸¹ Aggregation of tau into fibrils, or neurofibrillary tangles, is a hallmark of many neurodegenerative diseases. Therefore, any potential mechanism that could increase the local tau concentration in cells and help drive tau fibril formation would be of considerable interest to understanding tau pathologies.

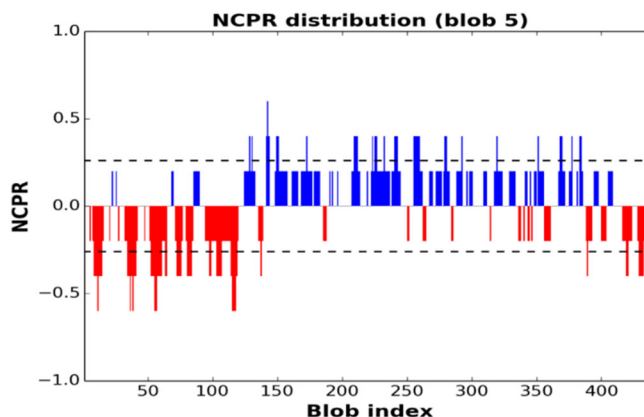


Figure 5.3 Algorithm CIDER analysis of intrinsically disordered protein tau 441 showing net charge per residue sequence at neutral pH.

5.1.2 Role of tau drops in formation of microtubule bundle

In vitro experiments by Hernandez-Vega et.al. show that the protein tubulin partitions into tau liquid droplets increasing the local tubulin concentration and enabling the nucleation of microtubules.⁵ The experiments were performed with and without GTP (guanosine triphosphate) and analyzed using fluorescence microscopy. In the absence of GTP, tubulin

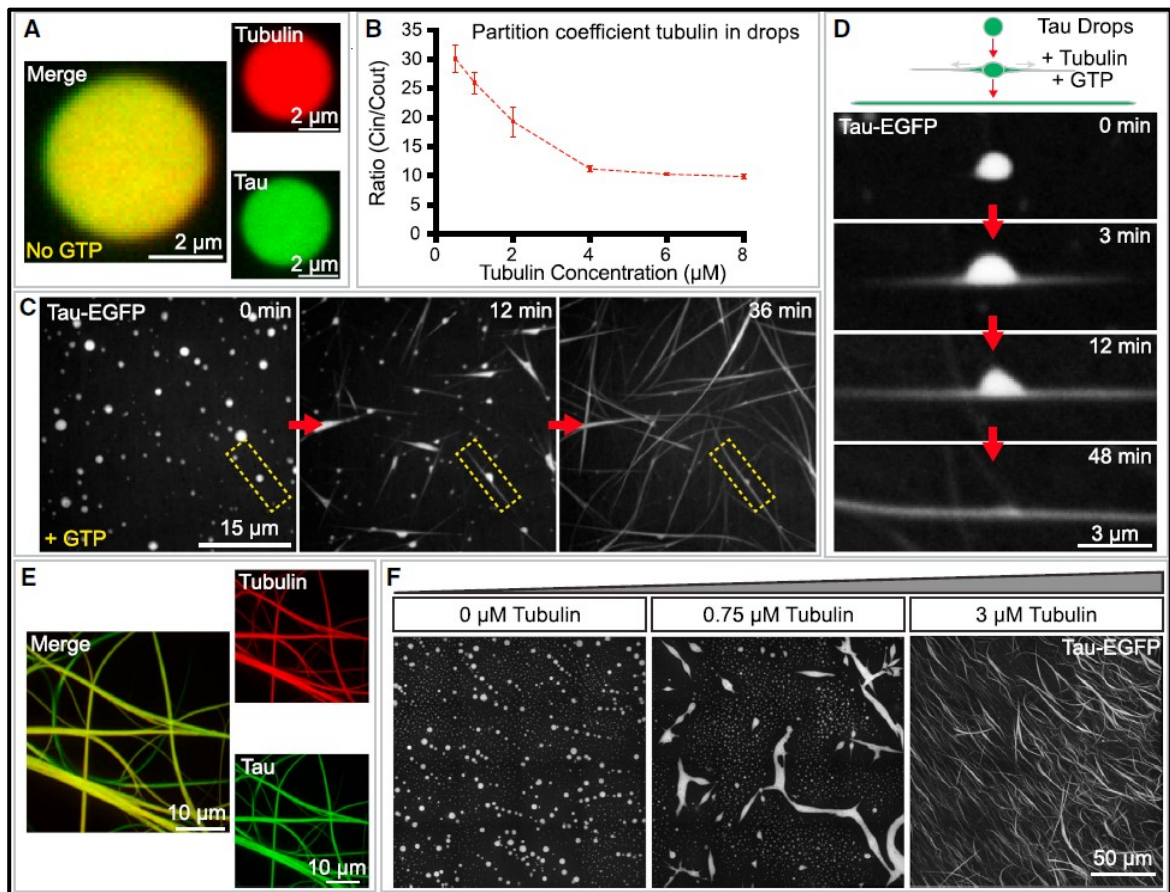


Figure 5.4 Formation of microtubule from tau drops, merged fluorescence images analyzed using single-channel fluorescence microscopy.⁵ A-B) Tau drops (green-EGFP) are formed *in vitro* using molecular crowder which concentrates tubulin (red-rhodamine labeled) proteins. C-F) Tau drops nucleation and polymerization within drops deforms into rod like structures resulting in microtubule bundle formation in presence of GTP.

(This figure is reprinted with permission from Hernandez-Vega et.al 2017, Cell reports, 20, 2304-2312).

partitions within tau drops and the concentration inside the droplet was higher than outside (**Figure 5.4 A-B**). In the presence of GTP, tau droplets deformed bidirectionally into rod like shapes as microtubule bundle with tau encapsulated structures (**Figure 5.4 C-F**).

5.1.3 Role of tau protein and its condensates for pathological conditions

Tau protein is the major constituent of neurofibrillary tangles in Alzheimer's and other neurological diseases (**Figure 5.5**) and has been shown to form intercellular inclusions in frontotemporal dementias (FTD's).²⁸¹ Abnormal hyperphosphorylation triggers conformational changes of the protein resulting ultimately in tau aggregation.^{300,301} Certain mutations also shown to be associated with tau aggregation process with abnormal ratio of 3R/4R.³⁰² Compounds that are shown to trigger fibrillization in hyperphosphorylated tau proteins are RNA³⁰³ and sulfo-glycosaminoglycans (sGAGs),³⁰⁴ which are sulfonated linear polysaccharides and include heparin, heparan sulfate and dermatan sulfate. Previous work has reported observing droplet-like tau accumulation in neurons, *in vitro* and *in vivo*, even in the absence of tau aggregation.^{281, 305} This likely suggests a unique biological function for tau LLPS not related to tau aggregation. Furthermore, Wegmann et al.²⁸¹ hypothesized that healthy neurons can maintain tau in a potentially reversible droplet state and further proposed that tau LLPS may act to initiate tau aggregation in neurodegenerative diseases. Hyperphosphorylation, as well as pro-aggregation mutations, favor tau LLPS causing subsequent maturation, hardening and aggregation in tau droplets. These effects can cause aberrant interactions with cellular organelles impacting homeostasis of neuron and protein expressions, eventually leading to neuronal death.^{278, 281} While some progress has been made towards understanding tau aggregate structure and kinetics of aggregation,³⁰⁶ and pathological toxicity of tau in diseased brain,³⁰⁷ many questions in the field remain unknown. These include (i) which molecules trigger tau aggregation and (ii) by what mechanism does functional highly soluble tau protein in healthy neurons switch to form highly insoluble, pathologically aberrant neurofibrillary tangles.²⁸¹

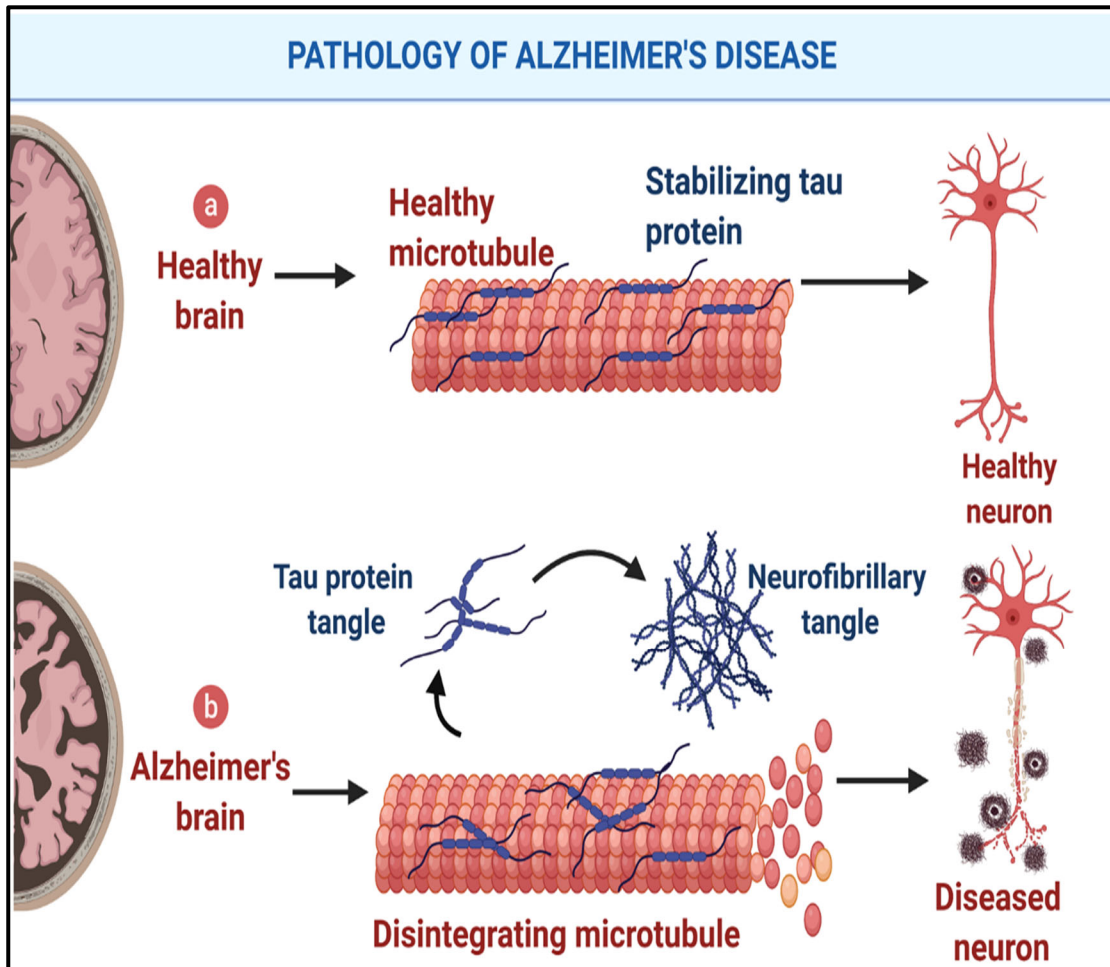


Figure 5.5 Pathology of neurodegenerative disorder a) Healthy neurons in brain have microtubules stabilized by tau protein. b) Disease associated neurofibrillary tangles of tau protein which leading to microtubule fragmentation and eventually neuronal death.

5.1.4 Project overview

It is recognized that protein droplets formed via LLPS are involved in the recruitment of molecules into the membraneless organelles. Despite the importance of particle entry within phase-separated droplets, little is known about the transport properties of particles within phase-separated protein droplets.

In this work, we utilize FCS measurements to measure the translational diffusion coefficients and number of probe dye molecules inside reconstituted tau protein droplets. FCS is able to clearly distinguish the transport properties of our probe molecules inside the tau droplets compared to outside the droplet. Upon formation, we see probe recruitment into the tau droplets resulting in higher concentration of probe molecules inside the droplet than outside. In addition to the particle partitioning effect into droplets, particle transport of the probe molecules is most reduced inside the droplet.

The essential characteristics of the condensates like internal diffusion rates, molecular sequestration and hierarchical organization of coexisting phases are dictated by the material properties such as surface tension and viscosity.^{308, 309} From polymer theory, we can make simple estimations of the structural length scale and mesh sizes within the tau condensates. We show the tau droplets are in the semi-dilute regime and are of low-density. Particles sufficiently small compared to the mesh size inside the droplet freely diffuse through the pores within the tau mesh network resulting in less hindered diffusion than expected from bulk viscosity measurements of the droplet.

Using a series of probe molecules with similar molecular size and core structure, but varying net molecular charge from 0 to -3, we systematically investigated the effect of charge-charge interactions on particle transport inside the tau droplets by FCS. Measured translational diffusion coefficients, D , by FCS showed that probe particles diffusion coefficients within the droplet is primarily driven by the local microviscosity of the tau droplet. Using a net charge neutral probe molecule, we estimate the microviscosity of tau condensates to be $\eta = (3.2 \pm 1.2) \times 10^{-3}$ Pa·s. FCS also allows us to directly determine the number of fluorescent probe molecules and we see a concentration of ~8-10-fold inside the tau droplets compared to outside the droplet. Probe particle transport is influenced to a lesser extent by the net probe charge. We observe a ~33% decrease in the probe diffusion coefficient as the net charge of the probe molecule increases from zero to -3 but similar 8-10-fold concentration within the tau LLPS.

We next compared particle diffusion of a larger protein molecule, bovine serum albumin (BSA) inside the tau droplet. FCS was used to measure translational diffusion coefficients

for BSA inside the tau droplets and these results were compared to BSA diffusion in buffer, soluble tau solution and in the dextran crowding solution used to form tau droplets. We show all four conditions can be distinguished by FCS. BSA transport was most hindered within the tau protein condensate. Surprisingly, the transport properties of BSA in all solutions are reasonably well described by using the Stokes-Einstein relation adjusted for the experimentally measured microviscosity obtained using the uncharged probe molecule. Measured values of D for BSA were slightly lower than the calculated values suggesting some systematic, non-steric contribution to the diffusion properties. BSA has a significantly higher net charge compared to the probe molecules used in this study and may suggest some additional contribution of charge-charge interaction between BSA and the tau protein chains within the tau condensates. Similar to the probe molecules, BSA was observed to be at a higher concentration ~ 10 -fold, inside the tau droplets than in the dextran crowding solution outside the tau LLPS.

Lastly, we examined the salt dependence on the particle transport properties inside the tau droplets. The net neutral charged probe molecule (At-A) showed no salt dependence on the measured translational diffusion coefficients (D), while all charged dye molecules and BSA showed a weak dependence of D on added KCl salt concentration. Remarkably, for both charged probe molecules and BSA, two plateau regions are observed with added salt with a crossover behavior at ~ 150 mM KCl. At KCl less than 150 mM, the measured D value of the molecules inside tau condensates does not change with added salt. Above 150 mM, however, an $\sim 20\%$ increase in D is observed within the tau droplets that then remains constant up to 500 mM KCl. The experimentally determined D values for charge probes, even at high salt, do not plateau to the same D value observed for the net neutral At-A probe molecule. This suggests the presence of charge-charge interactions between probe molecules and tau protein chains that are not screened out inside the condensate even at high salt. Taken together, these results shed light on the critical parameters for particle transport within liquid protein droplets of tau.

5.2 Materials and methods

5.2.1 Materials: A tau isoform tau 441, longest form 4RL was used for all experiments. Tau protein were expressed in bacterial strain E. coli (Escherichia coli) and purified using Ni-NTA column followed by gel electrophoresis to determine the presence and approximate purity of tau protein. For this study, uncharged dextran was used as a molecular crowder (Dextran 500 Pure neutral, Mw = 500 kDa), purchased from Sigma Aldrich (St. Louis, MO). A variety of water-soluble fluorescent probe molecules were purchased from Invitrogen (Carlsbad, CA). ATTO488-amine (AT-A, +0 charge), ATTO488-biotin (AT-B, -1 charge), and ATTO488-Carboxy (AT-C, -2 charge) were purchased from ATTO-TEC (Siegen, Germany). Alexa Fluor 488 carboxylic acid (AL-C, -3 charge) (Abs/Em maxima, 500/525 nm) was purchased from ThermoFisher Scientific (Waltham, MA). Rhodamine 110 used in calibration of confocal volume were purchased from Fischer Scientific. Protein probe BSA (Bovine albumin serum Alexa fluor 488 conjugate) with net charge -13 (pH =7.4) was purchased from Sigma Aldrich. All of the fluorescent probe molecules (Abs/Em maxima, ~500/525 nm) were used without further purification.

5.2.2 Droplet formation: To form droplets 44 μM Tau in 25 mM HEPES (2-[4-(2-hydroxyethyl) piperazin-1-yl] ethane sulfonic acid and 150 mM KCl (pH 7.4) with freshly added DTT (1mM) was mixed with 20 % dextran 1:1 to a final concentration of 22 μM and 10 % dextran and incubated for 24 hours. Tau protein condensates were collected by centrifugation at 1000 g for 120 s and pouring off the supernatant. The protein concentration of the tau condensate was assessed directly by measurement of the absorbance at 280 nm using a NanoDrop 2000 spectrophotometer (Thermo Scientific, Waltham, MA, USA). The measured absorbance was then used to calculate concentration using $A = \epsilon bc$ where ϵ is extinction coefficient of $7450 \text{ cm}^{-1}\text{M}^{-1}$ for tau, c is the concentration. With nanodrop instrument, the path length b is corrected for absorbance at 280 nm as 1cm.

5.2.3 Sample preparation with fluorophores: Fluorescent probes were added to the droplet solution to achieve a final concentration ~ 5 nM. Solutions were mixed gently using pipette and incubated overnight at room temperature. 10 μ L of sample was deposited into an imaging chamber (Secure sealTM hybridization chamber (Dimensions 7 \times 7 mm, depth 0.8 mm)) sealed with glass coverslip after removal of plastic liner. Droplets were allowed to equilibrate for 1 hour at room temperature inside the chamber before performing FCS measurements.

5.2.4 Confocal imaging: Tau condensates were prepared as described previously and incubated overnight at room temperature with ~ 10 nM probe concentration for visualization. Samples were deposited on Secure sealTM hybridization chamber and equilibrated at room temperature for 1 hr. Z-stack images were captured using a Nikon A1Rsi laser scanning confocal microscope equipped with a $\times 40$ objective. A 488 nm laser was used for excitation. Maximum intensity projections of Z- stacks fits were stitched together for tau droplet formation and converted to 8-bit depth images for analysis using image J software.

5.2.5 FCS set up: All FCS measurements were carried using a commercial dual-channel confocal fluorescent fluctuation system (ALBA FFS system, ISS, Champaign, IL). FCS experiments were made using a continuous wave 488 nm laser diode as an excitation source. Excitation light was directed into experimental samples through a Nikon Ti-U microscope (60 \times /1.2 NA water-immersion objective lens). The collected emission signals from the sample placed on the objective was then passed through a 514 nm long pass edge filter before detection. The emission signal was recorded by separate Hamamatsu H7422P-40 PMTs. The phase separated condensates are expected to have higher index of refraction than water, but previous characterization by Sherman et.al observed that confocal FCS can be reliably used to accurately determine translational diffusion coefficients of proteins and small molecules with refractive indices ranging from 1.33 to 1.46.³¹⁰ Confocal volume dimensions were determined through measurement of aqueous Rhodamine 110 at known concentrations. All FCS measurements were performed using 10 μ L of sample deposited

on a Secure seal™ hybridization chamber with sampling times of 30 s. To ensure homogeneity of measurements within the solutions, all FCS results shown are taken as an average of 15 measurements for every 5 repeats within each of the three different droplets within the sample. FCS curves were analyzed using the VistaVision Software (ISS, Champaign, IL) to determine the diffusion coefficient with measured diffusion coefficients expressed as the mean \pm SD.

5.2.6 FCS data analysis: The principles of FCS have been described in detail in literature^{189, 190} and chapter 2 of this dissertation. Here, we provide a brief overview. FCS measures the fluorescence fluctuations emitted from labeled molecules moving in and out of a small ~ 1 fL confocal volume. The size of the effective illumination volume is fixed by the confocal detection optics and the excitation profile of the focused laser beam and characterized by measurements against standard Rhodamine 110 of known diffusion constant ($D = 440 \mu\text{m}^2/\text{s}$).¹⁹¹ For uniformly distributed fluorescent particles diffusing by Brownian motion, dynamic information can be determined from the intensity fluctuations by means of a time autocorrelation given by

$$G(\tau) = 1 + \frac{1}{N} \left(1 + \frac{\tau}{\tau_d}\right)^{-1} \left(1 + \frac{\tau}{\beta^2 \tau_d}\right)^{-\frac{1}{2}} \quad (1)$$

where N is the average number of molecules in the detection volume, τ is the delay time, τ_d is the characteristic diffusion time, or the average passage time of a molecule through the confocal volume, and β is the structure parameter ($= z_o/\omega_o$) is the ratio of the axial to the radial dimensions of the confocal observation volume as determined by calibration measurements using dye with known diffusion constant. Here, β was fixed to 10 in all fits, based on results from calibration measurements with Rhodamine 110. Confocal volume with radial and axial $w_o = 0.358 \mu\text{m}$, $z_o = 3.58 \mu\text{m}$ respectively was determined via calibration of rhodamine 110 ($D = 440 \mu\text{m}^2 \text{s}^{-1}$) to confirm consistency in confocal beam geometry throughout the experiments. Acquisition time of 30 s, laser intensity 70% (Power = 200 μW) were used to optimize the signal-to-noise ratio for all the probes except BSA. Low intensity (85 μW) with sampling time of 20 s was used for labelled BSA to avoid fluorophore triplet states and photobleaching. Cross correlation with both detectors

minimizes the effects of detector after-pulsing in the resulting autocorrelations. The translational diffusion coefficient D ($\mu\text{m}^2/\text{s}$) can be calculated from τ_d and the radial width using

$$\tau_d = \frac{\omega_0^2}{4D} \quad (2)$$

For spherical particles, the diffusion coefficient D follows from the hydrodynamic radius, R_h , in solution and can be calculated by the Stokes-Einstein relation $D = k_B T / 6\pi\eta R_h$, where k_B is the Boltzmann constant, T is the temperature, and η is the viscosity of the medium.

5.2.7 Microviscosity measurements from Stokes-Einstein equation: The Stokes-Einstein equation, is used to understand the probe mobility where D is the translational diffusion driven by thermal energy, $k_B T$.

$$D = \frac{k_B T}{6\pi\eta R_h} \quad (3)$$

The bulk viscosity η is redefined as microviscosity for the probe diffusion, R_h is probe hydrodynamic radius. The normalized microviscosity (η/η_0), η and η_0 are the viscosities obtained for solution and buffer, respectively are proportional to the inverse of the normalized diffusion coefficients.

5.3 Results and discussion

5.3.1 Droplet solution profile showing differential interaction for probe

Tau can undergo a process of liquid-liquid phase separation (LLPS) to form liquid droplet-like membraneless organelles. LLPS formation is sensitive to solution ionic strength suggesting that tau phase separation is driven by electrostatic interactions likely between the negatively charged N-terminal and the positively charged mid-region.^{288, 294} Once formed, other particles or molecules can partition into the droplets and become concentrated. The partition coefficient of particles determines the degree of concentration within droplets and is shown to be important in regulating rate of reactions of the cell.³¹¹⁻

³¹⁴ For example, tubulin protein has been shown to partition into tau droplets nucleating and driving the formation of microtubule bundles in neurons.⁵ As a starting point to understand the importance of particle interaction and particle partitioning into the tau droplets, we first examined formation of tau protein droplets using brightfield microscopy. **Figure 5.6a** shows images of phase separated tau protein droplets. Droplets were formed from 22 μM tau using 10 % dextran as crowding agent and 25 mM HEPES buffer with 150 mM KCl salt. We next used fluorescence correlation spectroscopy (FCS) to determine translational diffusion coefficients and probe particle concentrations (**Figure 5.6b**) at four different locations (A-D) as indicated on the brightfield image. For these FCS experiments, we used Rhodamine 110 (R110) as our probe molecule. R110 is a dye molecule with a net molecule charge of zero. At pH 7.4, R110 is zwitterionic with one positive charge on the xanthene ring and one negative charge on the carboxyl group on the isolated benzene ring.³¹⁵ Normalized autocorrelation functions of R110 taken at locations A-D are shown in **Figure 5.6b**. All autocorrelation curves can be described by a single mean passage time with a clear shift to longer diffusion times for R110 inside the tau droplet compared to outside the droplet. Translational diffusion coefficients, D , as determined from equation 2, and R110 concentrations were determined for all four locations from the autocorrelation fits. The diffusion coefficient for R110 inside the tau droplet was approximately 25% lower than outside the droplet. Average diffusion coefficients were calculated from three FCS measurements at each location (A-D). Translational diffusion coefficient $D = 101 \pm 3 \mu\text{m}^2/\text{s}$ inside the tau droplet (locations B and C) compared to $D = 175 \pm 4 \mu\text{m}^2/\text{s}$ outside the droplet (location A and D). Diffusion of R110 outside the tau droplets is nearly identical to the diffusion coefficient determined for R110 in pure dextran crowding solution (10% dextran, 150 mM KCl, 25 mM HEPES) with $D = 170 \pm 6 \mu\text{m}^2/\text{s}$. FCS also gives us means to measure the particle concentration in these different locations. The complex environment inside protein droplets formed in vivo is thought to generate concentration gradients for diffusive flux of particles from cells into the droplets. Due to the lack of membranes, these liquid droplets allow for free exchange of molecules until an equilibrium state is reached. The constrained diffusion of particles within the droplet is indicative of the complex and differential particle transport properties in aqueous two-phase systems at

physiological conditions. Despite being loaded initially with ~ 10 nM R110, we find that the tau droplets are enriched with dye molecule with R110 concentrations >10 -fold higher

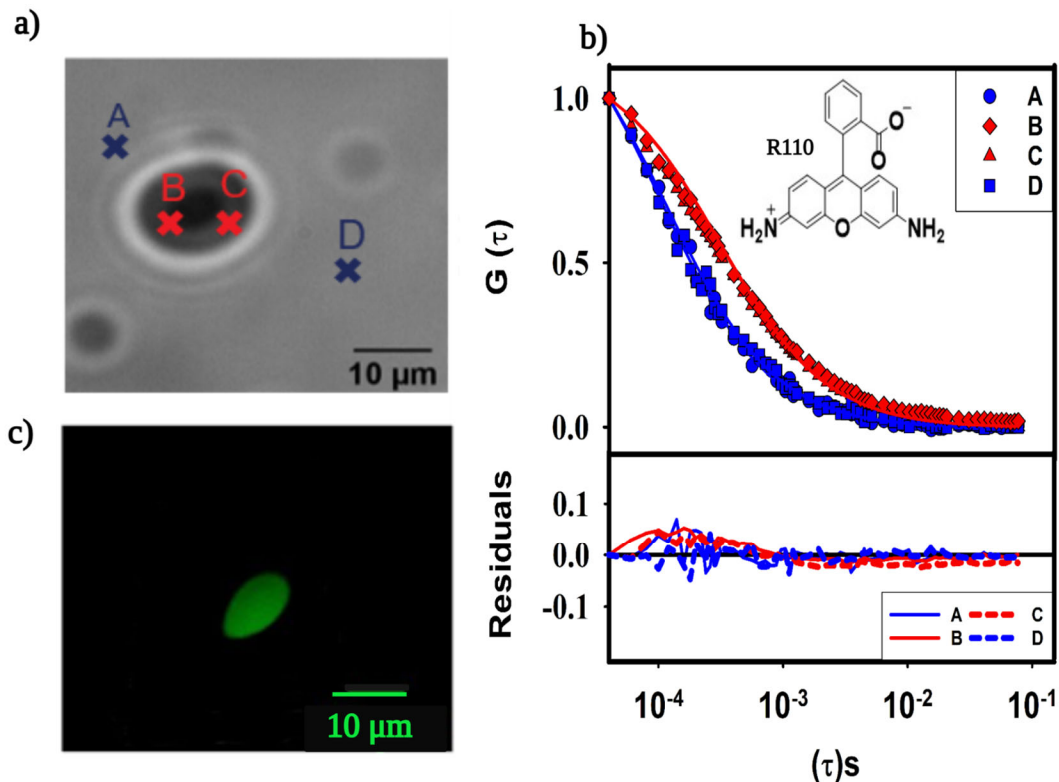


Figure 5.6 Droplet solution profile a) Brightfield image showing Tau protein droplets formation after liquid- liquid phase separation in the presence of 10 % dextran as crowding agent. b) Normalized autocorrelation curves for probe R110 in droplet solution, with reduced mobility for the phase separated droplet inside compared to outside solution. Insert shows the structure of zwitterionic probe R110. c) Confocal microscopy image of R110 accumulation inside tau protein droplets.

inside the tau protein droplet compared to outside the droplet. R110 concentration was $\sim 23 \pm 6$ nM inside the droplet and only $\sim 2 \pm 3$ nM outside the droplet. The partition coefficient of the dye molecules in the droplet solution is likely due to the high protein concentration and confinement of the tau condensate responsible for recruitment of particles within droplets. This combined effect for recruitment of particles and microtubule bundle formation was also indicated for tau drops with tubulin.⁵ The concentration of R110 inside the droplet is also observed by confocal microscopy. **Figure 5.6c** shows confocal

microscopy image of tau droplets loaded with R110. Due to the more than 10-fold concentration of R110 inside the tau droplet, we can easily observe tau droplets by confocal microscopy (**Figure 5.6c**).

5.3.2 R110 diffusion within tau solution, dextran solution and tau condensates

The liquid demixing in LLPS is a process of separation of protein into dense and light protein phases that is driven by microscopic interactions and governed by thermodynamic properties.³¹ When a molecular crowder, such as dextran is present, tau has been shown to undergo liquid demixing to form liquid-like drops. To understand how R110 diffusion differs in the presence of tau protein before and after the demixing process, we measured the transport properties of R110 in different solutions using FCS. **Figure 5.7a** shows normalized autocorrelation functions for R110 in tau condensates (Tau C), in 10% dextran (10% Dex), and in tau solution (Tau S). Here Tau S is 22 μM tau protein, identical to the concentration of tau used to make tau condensates. All three solutions used the same 150 mM KCl, 25 mM HEPES (pH 7.4) buffer. Again, we see a characteristic shift in the characteristic diffusion time τ_d , for R110 in the presence of tau protein before and after phase separation. Diffusion of R110 in 10% Dex is intermediate between Tau S and Tau C. FCS measurements were performed at various spots within the solutions and averaged. Consistent with our prior results, translational diffusion coefficients, D , in the protein droplets (Tau C) and in 10% Dex were $106 \pm 8 \mu\text{m}^2/\text{s}$ and $170 \pm 6 \mu\text{m}^2/\text{s}$, respectively. In Tau S, we measure a much higher diffusion coefficient ($D = 296 \pm 8 \mu\text{m}^2/\text{s}$) for R110. R110 diffusion in Tau S that is $\sim 5\%$ slower diffusion than in 150 mM KCl, 25 mM HEPES (pH 7.4) buffer alone ($D = 311 \pm 6 \mu\text{m}^2/\text{s}$). The small change in D for R110 in Tau S compared to buffer strongly suggests there are no strong probe-protein interactions present and R110 freely diffuses in the Tau S solution. The decreased transport properties of the probe in Tau C is presumably due to the higher protein concentration within the droplets. To test this, we measured the UV/VIS absorption at 280 nm for our four different solutions: buffer, Tau S, 10% Dex, and Tau C. Results are given in **Figure 5.7b**. As expected, the buffer and 10% Dex show very low A_{280} values as no tau is present. Using an extinction coefficient of $7450 \text{ cm}^{-1}\text{M}^{-1}$ for tau, the tau concentration in Tau S was determined to be $21 \pm 4 \mu\text{M}$

consistent with the $\sim 22 \mu\text{M}$ used to make TauC/TauS solutions. The experimentally determined protein concentration in droplets formed in Tau C was $172 \pm 5 \mu\text{M}$ representing an ~ 8 -fold increase in the concentration of tau in the droplet. This tau concentration inside the droplet is consistent with previous work that estimated tau protein (2N/4R) concentration of $210.7 \mu\text{M}$ within liquid droplets.²⁹⁵

A central tenet of the phase behavior within polymer solutions is the concept of the critical overlap concentration, c^* . The critical overlap concentration defines the boundary between the dilute and semi-dilute regimes and represents the concentration at which different polymer chains cease being separated from each other and begin to overlap. c^* also defines the point where inter-chain contacts between polymer chains are more likely than intra-chain contacts. By calculating c^* , we can determine if the tau protein concentration within droplets is above c^* and therefore in the semi-dilute concentration range. The overlap concentration can be calculated³¹⁶ using equation (4):

$$c^* = \frac{M_w}{N_A \left(\frac{h_0}{2}\right)^3} \quad (4)$$

where M_w is molecular weight of the tau protein (46.7 kDa), N_A is Avagadro's number and h_0 is the polymer end to end distance for tau determined by Monto-Carlo simulations as 18.6 nm.³¹⁷ For full-length human tau protein, c^* is determined to be 96.4 mg/ml or 2.06 mM. The calculated overlap concentration is far below the experimentally determined values for tau concentration inside the droplet. This suggests while tau condensates are dense compared to the surrounding solution they are still relatively low-density droplets that are solvent-rich and full of permeable voids. One should expect small molecules to be able therefore to freely diffuse within the protein droplets. Similar low-density droplets were previously reported by Wei et al. for LAF-1 protein that form P granule-like droplets in vitro.³¹⁸ For neutral probe molecules, such as R110, with dimensions much smaller than the droplet mesh size, we expect the transport properties to be dictated not by the bulk viscosity of the droplet but rather the local micro-viscosity within the low density droplet. This behavior has been reported previously for probe diffusion within proteins based on the volume fraction and its relation to the phase behavior large-mesh size polymer networks.²⁰⁶ The large conformational fluctuations of IDPs generate large, pervaded

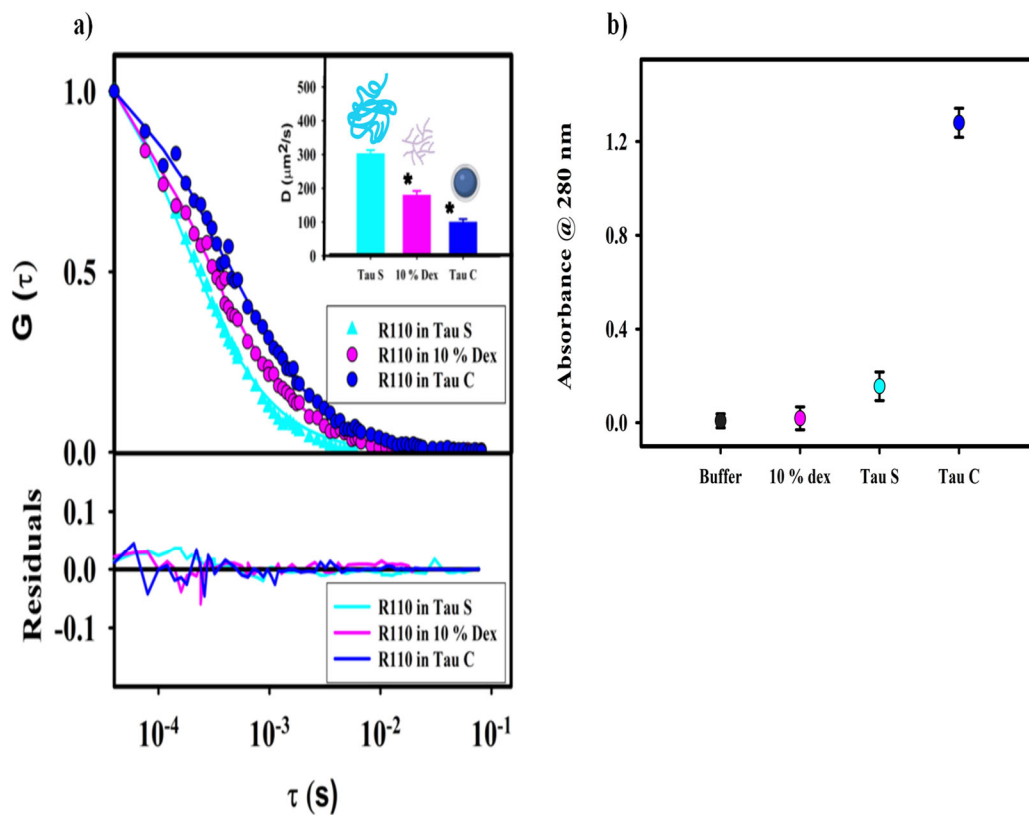


Figure 5.7 a) Plot showing the normalized autocorrelation curves for probe R110 in different tau protein environments, constituting a highly hindered mobility for the phase separated tau protein in comparison to the controls. Solid dashed lines are fits to the experimental data by equation 2 to determine the D , translation diffusion coefficient. The insert shows a schematic indication for changes in D for the probe R110, with change in interaction environment. $*p < 0.001$ vs D of Tau S. b) Nanodrop Lite spectrophotometer absorbance (280 nm) facilitates for the measurement of protein concentration of tau before and after liquid demixing process in 25 mM HEPES 150 mM KCl pH 7.4. The plot shows that the absorbance value is nearly 10 times higher for phase separated protein droplets.

volumes which is a measure of the volume of solution spanned by the polymer chain. Due to these large volumes, the concept of overlap volume fraction and its relation to the phase behavior of polymer solution can be well described.¹⁹⁶ The overlap volume fraction (ϕ^*) and volume fractions (ϕ) can be calculated using equations (5) and (6) respectively:

$$\phi^* = \frac{rV_m}{\frac{4}{3}\pi(R_{ee})^3} \quad (5)$$

$$\phi = c \left(\frac{V_m N_A}{M_m} \right) \quad (6)$$

where r is degree of polymerization, (number of amino acid residues in protein, 441), V_m is average volume occupied by amino acids in protein (140 \AA^3), M_m is average mass of an amino acid (110 g/mol), R_{ee} is end-end distance (18.6 nm for 2N4R isoform of tau),³¹⁷ N_A is Avagadro's number and c is the mass concentration of protein. De Gennes³¹⁹ equation describes the relationship between correlation length, radius of gyration (R_g), and polymer volume fraction (ϕ) as $\xi \sim R_g \left(\frac{\phi}{\phi^*} \right)^x$. Here, x is a function of scaling exponent and equation can be rewritten as (7).

$$\left(\frac{\phi}{\phi^*} \right)^x \sim \left(\frac{\xi}{R_g} \right) \quad (7)$$

The calculated ϕ and ϕ^* are 5.3×10^{-3} and 3×10^{-3} respectively, which are nearly the same so $\left(\frac{\phi}{\phi^*} \right)^x \sim 1$. As a result, the correlation lengths ξ are on the same order of chain dimension R_g of polymer as represented in equation 8.

$$\left(\frac{\xi}{R_g} \right) \sim 1 \quad (8)$$

The average radius of gyration measured in good solvent via hard sphere method for 4RL (longest isoform with 2 N-terminal repeats and 4 proline repeat residues) isoform³¹⁷ as 8.43 nm. Following the calculations discussed previously, the correlation length ξ within the tau droplet is therefore estimated to be ~ 8.4 nm. Using the experimentally determined tau protein concentration we obtained inside the tau droplet, we can estimate the intermolecular distance between tau chains as ~ 21 nm. These length scales are depicted in **Figure 5.8**, where the red dashed lines indicate R_g , and the black dashed lines indicate the intermolecular distance between tau chain.¹⁹⁵ Using the Stokes-Einstein equation the hydrodynamic radius, R_h , of R110 was determined to be ~ 0.6 nm. Using this R_h value, we can then calculate an apparent viscosity, for tau droplets based on the experimentally determined D values of R110 in Tau C. We measure an apparent viscosity of 3.63×10^{-3}

Pa.s for R110 within Tau C. This is consistent with R110 primarily diffusing through the aqueous buffer that permeates the low-density tau droplet mesh.

5.3.3 Electrostatic effects on particle transport within tau condensates

Human tau is a polyampholytic IDP expressed as six major isoforms, of which tau441 is

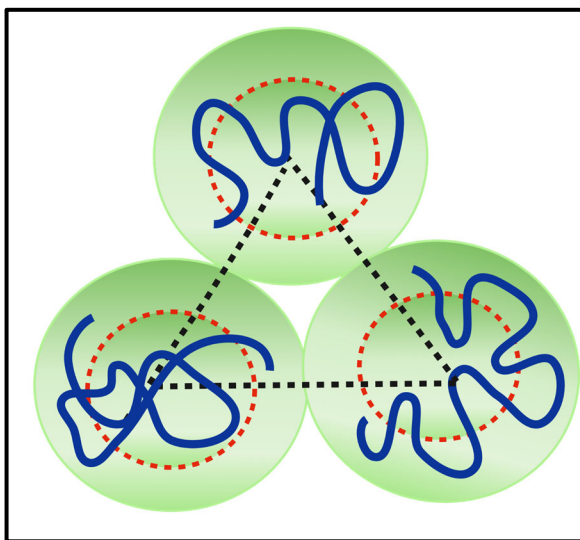


Figure 5.8 Schematic illustration showing molecular chain interactions in semi-dilute regime of tau condensates. The molecular domains represent a range of conformations with $R_g \sim 8.3$ nm shown in red dashed line. The calculated concentration for tau droplets corresponds to a number density of 1.0×10^{-4} molecules/nm³ and has intermolecular distance ~ 21 nm shown in black dashed lines.

the longest. The polarized nature of tau has led to the hypothesis that droplet formation of tau is largely driven by attractive electrostatic interactions between the acidic residues of the N-terminal and the basic residues of the middle and C-terminal of tau.²⁹⁴ Despite having many negatively and positively charged amino acid residues, the net charge of full length tau 441, 2N4R at pH 7.4 is modest at $\sim +2.5$.²⁹⁵

To better understand the role of charge on the transport processes within tau droplets, we used FCS to determine the translational diffusion coefficients of a series of probe molecules with nearly identical core structure but varying overall net molecular charge. Structures for the four probe molecules used in this study are provided in **Figure 5.9**. The Atto/Alexa dyes have similar core structures, excitation and emission spectra, and size ($\sim R_h \sim 6.2 \text{ \AA}$) but vary in net charge from 0 to -3 at pH 7.4. Specifically, these probes include Atto 488 amine [At-A, net charge 0], Atto 488 ester [At-E, net charge -1], Atto 488 carboxy [At-C, net charge -2], and Alexa 488 carboxy [Al-C, net charge -3]. Using these four probes, we can systematically study the effect of probe charge on the diffusion properties within the tau condensates.

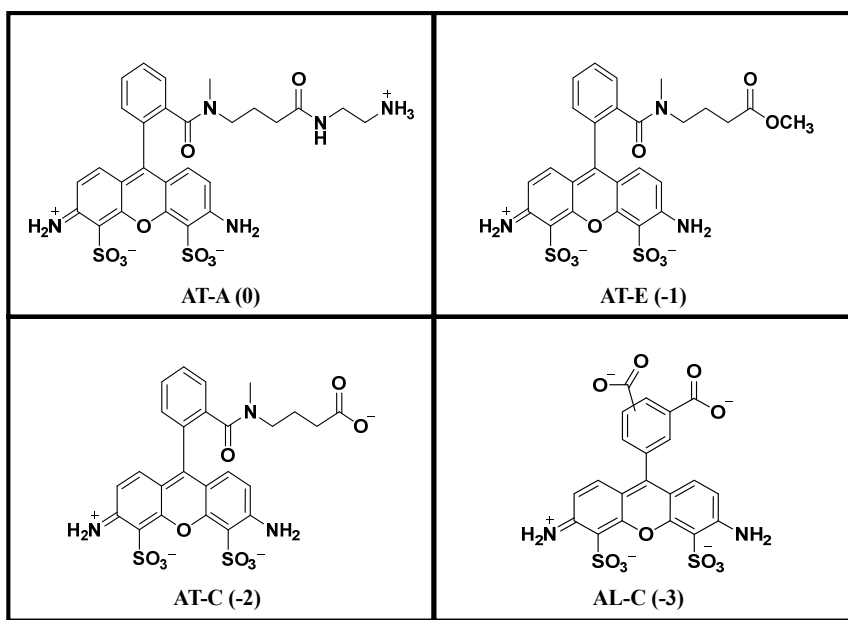


Figure 5.9. Molecular structures of the four probes used in this study

Normalized autocorrelation functions of the neutral and negatively charged probe molecules measured within the tau condensates are shown in **Figure 5.10a**. All autocorrelation curves can be described by a single mean passage time. The measured τ_D

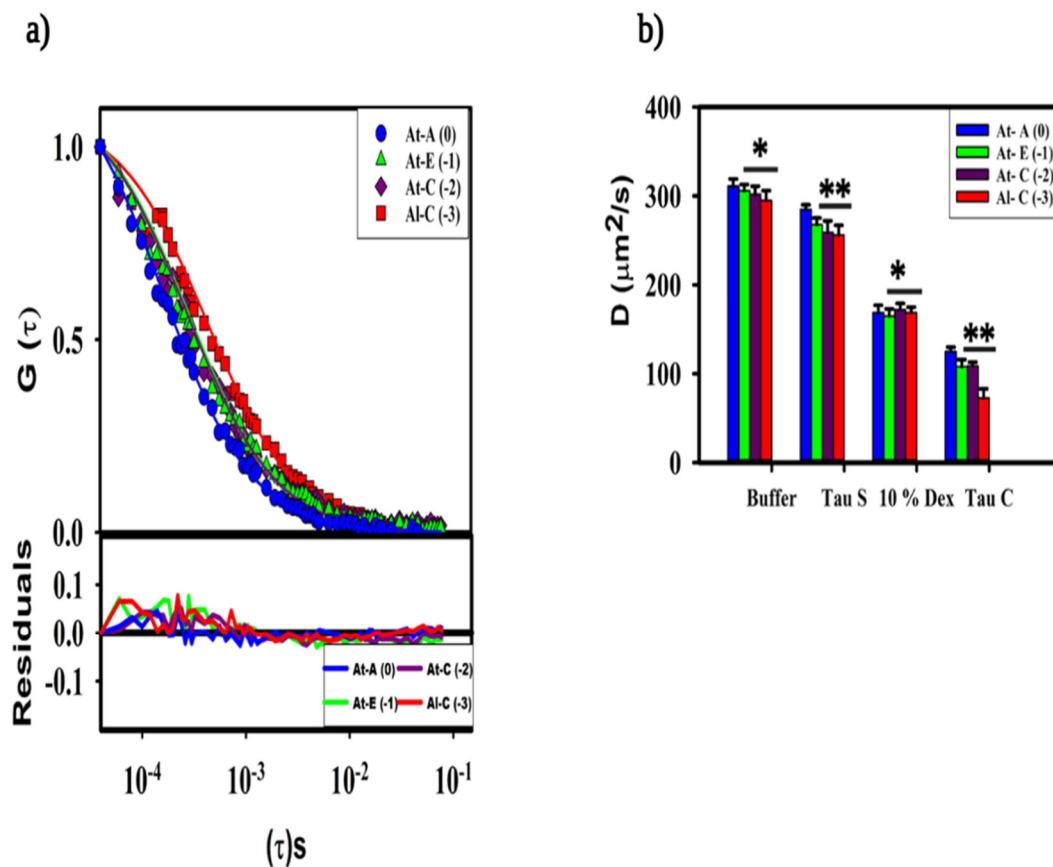


Figure 5.10 a) Representative plots of normalized FCS autocorrelation of probe molecules of varying net charge in tau protein condensates. b) Comparative apparent diffusion coefficients D determined from FCS for various controls and condensates in understanding the reduced transport within condensates. * $p > 0.05$, ** $p < 0.01$ vs D of At-A (0) of each appropriate solution.

of the probes inside the tau condensates increases only weakly for probes with higher net charge. **Figure 5.10b** shows the translational diffusion coefficients calculated from equation 2 for all four probes. FCS measurements were performed in buffer (25 mM HEPES, 150 mM KCl), in 22 μM tau solution, in 10 wt % dextran, and in tau condensates formed from 22 μM tau in 10 wt% dextran. As expected, no statistically significant difference in D is observed for the 4 probes in buffer or in the uncharged dextran solutions.

In the presence of tau, both Tau S and Tau C, statistically relevant changes in D are observed for charged probes when compared to uncharged At-A. This suggests attractive electrostatic interactions between the probes and tau molecule chains are playing a role in the observed reduced transport properties. The largest effects are observed for the highest charged (-3) probe molecule. Also, diffusion of the neutral At-A probe is observed to be nearly identical to R110 consistent with both net neutral, zwitterionic probes having minimal probe-tau interactions. Also, as shown in **Figure 5.10b**, D values in tau condensates are all significantly reduced 2.5- to 4-fold in comparison to tau solution for all four fluorophores studied regardless of charge. This suggests transport in the tau droplets is primarily dictated by the confinement and the higher local concentration of tau droplets with only a weak dependence on molecular probe charge. In our series of probes, the charge-charge interactions are sufficient to decrease probe diffusion $\sim 33\%$ from $114 \mu\text{m}^2/\text{s} \pm 5$ to $\sim 76 \pm 7 \mu\text{m}^2/\text{s}$ for the same size probe molecule with net charge ranging from zero to -3.

In simple fluids, the translational diffusion coefficient of spherical particles is well described by the Stokes-Einstein relation (equation 3). In ternary mixtures, containing polymer molecules, solvent and particles, multiple length scales exist, and application of Stokes-Einstein becomes more complicated. For example, Holyst et al. performed FCS experiments with a variety of probe molecules with different radii R diffusing inside poly(ethylene glycol) (PEG) solutions in water.²⁰⁶ They showed that when R was sufficiently smaller than the correlation lengths inside the PEG solution, the measured diffusion coefficient was significantly faster than expected from the bulk macroviscosity of the PEG solution.²⁰⁶ Fixing the particle R_h determined in buffer, one can use FCS to estimate an apparent microviscosity felt by the probe molecule inside the polymer network. The microviscosity reflects the fact that in this scenario the probes primarily diffuse through the aqueous solution that permeates the polymer network. Holyst et al. showed the microviscosity they measured was orders of magnitude smaller than the macroviscosity for their PEG solutions. With large enough probes, where R was larger than the PEG correlation lengths, Stokes-Einstein behavior was recovered consistent with the macroviscosity.

To understand the effects of local environment on probe mobility in our system, we also used similar methods to determine the apparent microviscosity experienced by our probes in our different solutions. Within the semi-dilute tau condensates, we estimate a correlation length of ~ 8.4 nm for the 4RL isoform of tau. This length is considerably larger than our probe systems ($R_h \sim 0.6$ nm). Apparent microviscosities calculated for all four probes (net charge 0 to -3) for 25 mM HEPES, 150 mM KCl buffer, Tau S, 10% Dex and Tau C solutions and normalized relative to their diffusion in water ($\eta_0 = 9.01 \times 10^{-4}$ Pa.s). The normalized microviscosities (η/η_0) are given in **Figure 5.11**. As expected, the microviscosity for all four probes was nearly identical in 25 mM HEPES, 150 mM KCl (pH 7.4) buffer as in water. Microviscosities increased in Tau S and 10% dextran solutions approximately 1.3 and 2-fold, respectively, over buffer. No clear dependence on the apparent microviscosity with increasing probe charge was observed for either Tau S or 10% dextran solutions. Our calculated value for microviscosity of 10 w/v % dextran is also consistent with reported value for eGFP-CaM diffusion within 10 w/v% dextran solutions as determined from MEMFCS fits (autocorrelation fits obtained by multiple-component model with maximum entropy method).²⁰⁸ In contrast, apparent microviscosities for the neutral probe At-A increased (~ 3.5 - 4.2 fold over water) inside the tau condensates. In addition, a systematic decrease of $\sim 20\%$ in the translational diffusion coefficient for our probe molecules inside was observed with increasing probe charge. This decrease in D reflects the increased charge-charge attractions of the -3 probe inside the tau droplet. Using these measured D values to estimate an apparent viscosity within the tau condensates, we see a systematic change dependent on probe charge only in the tau condensates (**Figure 5.11**).

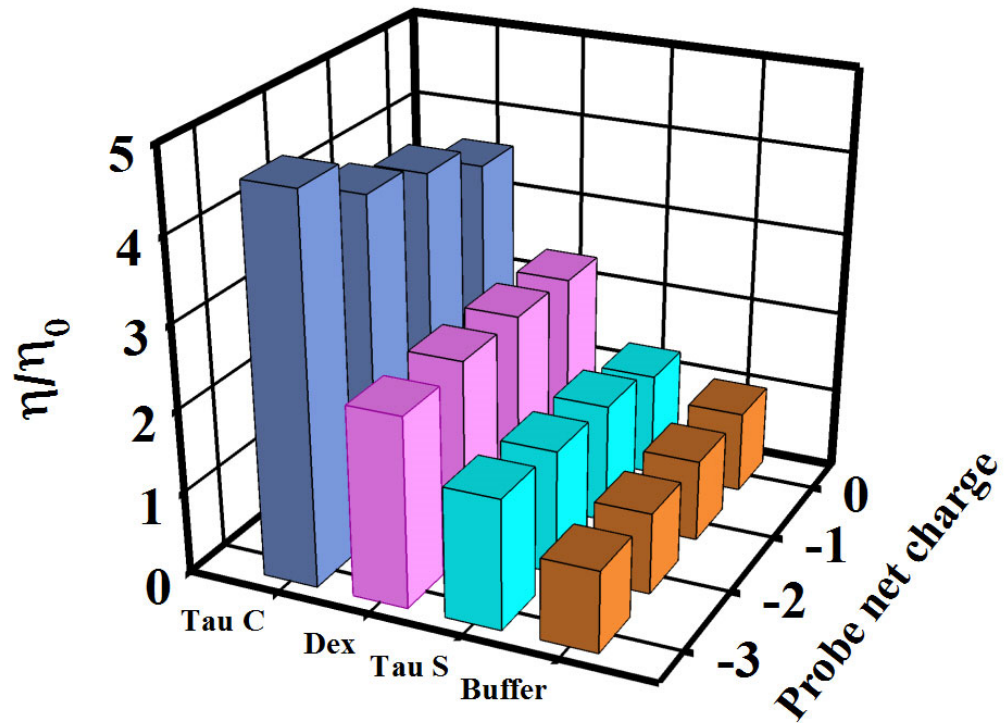


Figure 5.11 Normalized microviscosity (η/η_0) using Stokes Einstein equation where η and η_0 are the viscosities obtained for solution and water respectively. The normalized microviscosity increases for tau protein condensates when compared to Tau S and its controls which is proportional to the physiochemical interactions of probe diffusion in a crowded polymeric solution.

5.3.4 Protein transport within protein droplets

Protein droplets, being membraneless, have the advantage that they can form and dissolve readily in vivo and have been shown to enable various cellular functions often through the recruitment of larger molecules such as proteins. How protein droplets influence the dynamics of proteins inside them is still not fully understood. Here, we have focused on investigations of the transport properties of bovine serum albumin (BSA) inside tau protein droplets. Albumin is a globular monomeric protein that is a major component of proteins found in blood. Its function is to regulate body fluid distribution inside human body by maintaining plasma colloid osmotic pressure.³²⁰ Albumin is also known to bind and carry

various substances including water, cations, hormones and exogenous drugs and also acts as a free radical scavenger in inflammation.³²¹ BSA consists of 585 amino acid residues including 35 cysteines that form disulfide bridges that result in a relatively strong stability of BSA in solution³²². BSA has a hydrodynamic radius (R_h) of 3.5 nm,³²³ significantly larger than the previously studied dye probe molecules $R_h \sim 0.6$ nm. BSA is also charged with a net negative charge³²² of -13 at pH 7.4. Translational diffusion coefficient of Alexa488-labeled BSA in HEPES/KCl buffer, Tau S, 10% Dex and Tau C was determined using FCS. Representative normalized autocorrelation curves for all four solutions are shown in **Figure 5.12a**. All autocorrelation curves are again well described by a single mean passage time. The measured translation diffusion coefficient D of BSA in 25 mM HEPES, 150 mM KCl (pH 7.4) buffer is $69 (\pm 6) \mu\text{m}^2/\text{s}$. Using Stokes-Einstein relation (equation 3), a hydrodynamic radius can be calculated as 3.4 nm in good agreement with previous measurements of R_h for BSA. As seen in **Figure 5.12a**, the characteristic diffusion time is slightly larger for BSA in Tau S resulting in a calculated $D \sim 42 \pm 5 \mu\text{m}^2/\text{s}$. By FCS, we see minimal evidence of significant protein-protein interactions between BSA and Tau hindering free diffusion within the tau protein solution. In a similar fashion, BSA diffusion was determined to be $26 \pm 4 \mu\text{m}^2/\text{s}$ inside 10 wt % dextran solution and $12 \pm 6 \mu\text{m}^2/\text{s}$ inside the tau protein droplets. The formation of liquid droplets by LLPS has been proposed as a means to locally concentrate proteins through varying strength of affinities between the protein in the droplet and other proteins.³²⁴ By FCS, we find after equilibration that BSA is enriched inside the tau droplets with BSA concentrations ~ 10 -fold higher inside the tau protein droplet. BSA concentration was $\sim 26 \pm 6$ nM inside the tau droplets and only $\sim 3 \pm 3$ nM outside the droplets. Fixing the R_h of BSA, we can again determine the apparent microviscosity for each solution as described in section 5.3.3. Using the neutral At-A probe, we previously determined the microviscosity in our solutions with normalized microviscosities ranging from 25 mM HEPES, 150 mM KCl buffer $\eta/\eta_0 = 1.0$ (no apparent change in microviscosity compared to viscosity in water) to $\eta/\eta_0 \sim 4.5$ inside the tau condensates. Fixing the hydrodynamic radius of BSA at 3.4 nm, we can use these microviscosity values to calculate an expected D value for BSA within each solution assuming BSA diffusion is free and dominated by the apparent viscosity within each

solution. In **Figure 5.12b**, we plot the measured D values for BSA in the four solution as a function of the normalized microviscosities. Calculated values for D, are shown by the

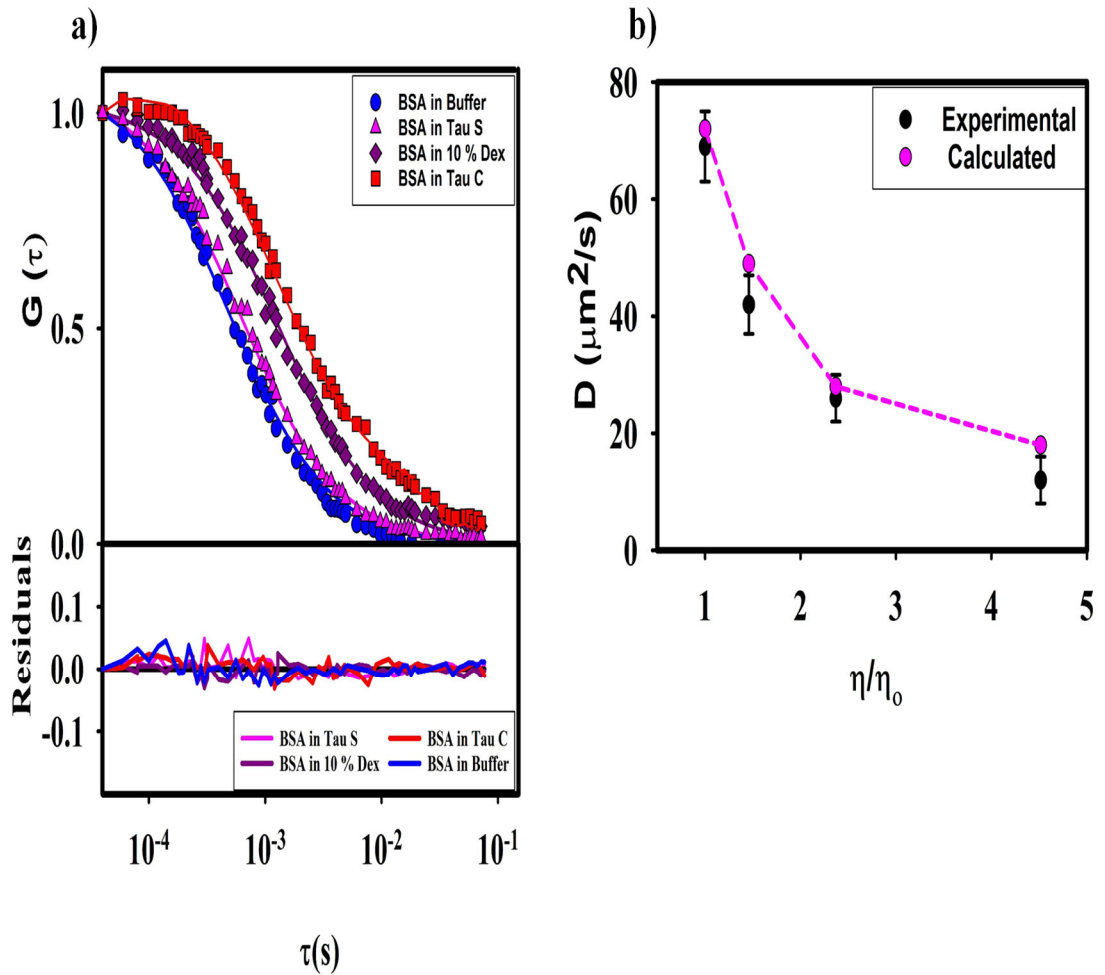


Figure 5.12 a) Representative autocorrelation plots for Alexa488-labelled bovine serum albumin (BSA) in buffer [25 mM HEPES 150 mM KCl], tau protein solution, 10% dex and Tau condensates. b) Comparative apparent diffusion coefficients D determined experimentally from FCS for various solutions and inside tau condensate compared to calculated D using experimentally determined microviscosity values. Diffusion in all solutions is reasonably well described by accounting for microviscosity. * $p < 0.01$ ** $p < 0.001$ vs D of buffer solution.

dashed line. In general, we see good agreement between experiment and calculated D values for BSA in all four solutions. So despite the larger BSA protein being larger in size (diameter ~ 6.2 nm) with particle dimensions closer in size to the calculated tau droplet

mesh size (21 nm), BSA is still sufficiently small to permeate and diffuse relatively freely inside the permeable voids of the tau condensate, and commensurate with Stokes-Einstein behavior for the experimentally determined microviscosity of the polymer solution. Experimental values of D are observed to be slightly lower than expected in Tau S and Tau C. This may be due to weak attractive electrostatic effects between the charged BSA and tau proteins. However, these estimates suggest these interactions are a minor contributor to the total transport behavior of BSA in Tau S or Tau C.

5.3.5 Dependency of ionic strength on tau droplet formation and particle transport inside droplets

Previous studies of tau have shown the formation of tau protein droplets is strongly dependent on the ionic strength of the buffer.^{5,281} Boyko et al. showed tau droplet formation in PEG solutions resulted in fewer droplets, with smaller dimensions, being formed at 150 mM NaCl when compared to 10 mM NaCl.²⁹⁴ This dependence was similar for either KCl or NaCl monovalent salt. We therefore examined the ionic strength dependence on tau droplet formation in our system. 22 μ M tau 441 in 25 mM HEPES buffer (pH 7.4) was used to form droplets in the presence of 10 wt % dextran crowding solution. KCl salt concentration was varied from 50-500 mM. Representative bright-field images of the tau protein droplets observed are shown in **Figure 5.13a**. In these conditions, we observe the size of the droplets to be approximately the same over these ionic strengths. Droplets are \sim 10-11 μ m in diameter for all salt concentrations used in this study. UV/VIS was used to measure the A280 values and determine the tau protein concentration inside the droplets. **Figure 5.13b** shows the measured tau concentration in droplets as a function of the KCl concentration in the buffer. The protein concentration inside the droplets is nearly independent of the ionic strength showing only a slight decrease at the highest KCl concentration measured. To determine if the ionic strength of the buffer screens the electrostatic interactions between probe and tau protein inside the droplets, we next used FCS to measure the diffusion coefficients of all four dye proteins and BSA at various KCl concentrations. As discussed earlier, tau protein droplet is a low-density droplet with relatively large-mesh size allowing both our dye probes and BSA protein to diffuse readily.

BSA size is not particularly sensitive to salt concentration, as it was shown that at low BSA concentration, the addition of more salt does not change any relative Coulombic interaction.³²⁵ In addition, the ionic strength would affect the Debye length and thus the

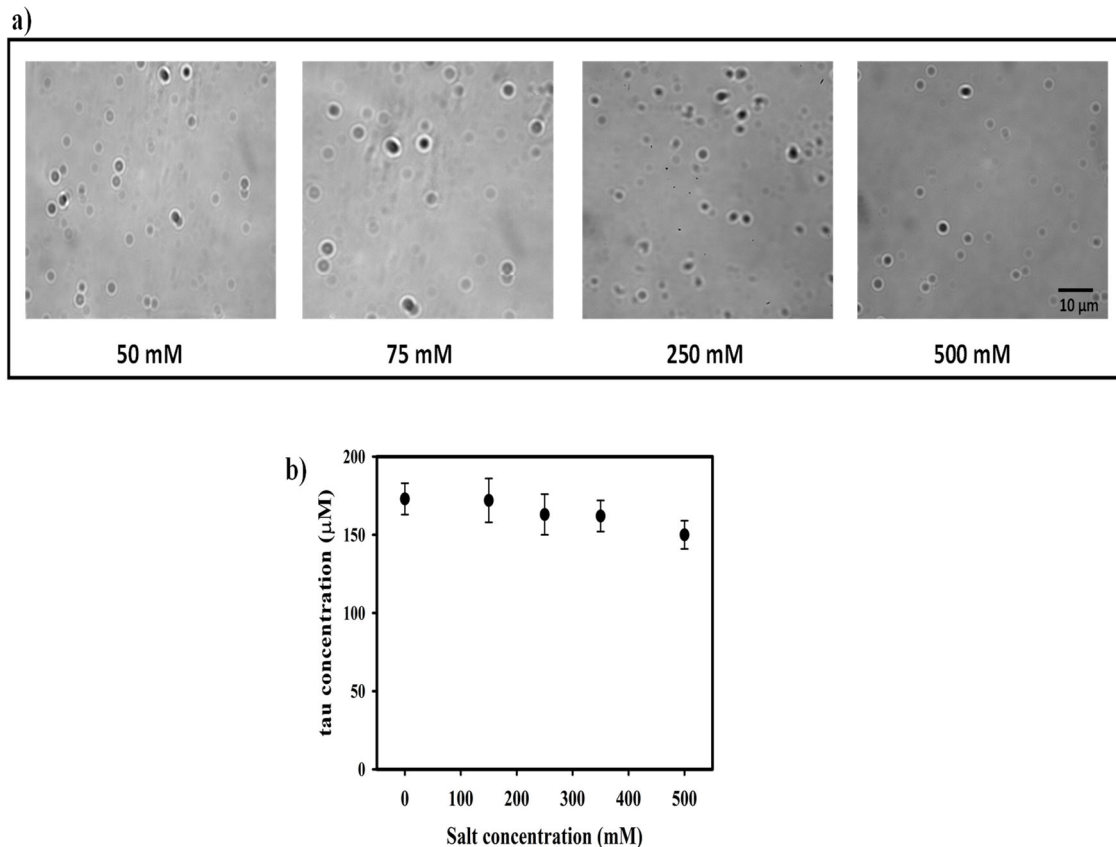


Figure 5.13 Salt effect study in tau condensates a) Representative bright-field images of tau protein droplets formed in the presence of varied KCl salt concentration. b) Tau protein concentration inside liquid-droplets as determined by A280 values from UV/VIS as a function of the KCl salt concentration.

distance over which electrostatic forces can influence the particle transport inside the droplet. Translational diffusion coefficients for various probe molecules inside tau droplets are shown in **Figure 5.14** as a function of increasing KCl concentration in the buffer. For the neutral zwitterionic dye At-A, no dependence of D with increasing ionic strength is observed consistent with minimal charge-charge interactions between probe and tau inside

the droplet. Recent research on the droplet systems of proteins like *Caenorhabditis elegans* protein LAF-1, showed a decrease in the bulk viscosity upon increasing salt concentration.³¹⁸ But in tau condensate systems, we see no significant decrease in the microviscosity with increasing KCl concentration. The net neutral probe diffuses nearly identically inside the tau droplet for all KCl concentrations studied. This suggests the slight decrease in the measured tau concentration in droplets formed at high KCl concentrations did not significantly alter the local microenvironment. Using ultrafast-scanning FCS (usFCS), Wei et al. measured translational diffusion coefficients for 14 nm diameter fluorescent polystyrene beads inside LAF-1 protein droplets.¹⁹⁶ They reported LAF-1 droplet viscosity of 27.2 ± 5.9 Pa s at 125 mM NaCl consistent with prior estimates of droplet viscosity determined by particle tracking microrheology. These larger polystyrene beads (>10 nm) in LAF-1 gave viscosities consistent with bulk droplet viscosity values. With increasing ionic strength, they observed a corresponding decrease in bulk viscosity inside the LAF-1 droplets. For smaller particles, usFCS showed enhanced diffusion consistent with apparent viscosities, or microviscosities, roughly two orders of magnitude lower than bulk consistent with particle diffusion within voids inside the LAF-1 droplets. For our measurements, At-A probe is much smaller and D values will reflect the microviscosities inside the droplet. As D is insensitive to ionic strength in the tau droplets, the microviscosity values are not changed by added salt.

Comparing the neutral At-A dye to our other similar sized dye probes, we can systematically examine the effect of increasing ionic strength on particle-tau interactions with increasing probe charge (**Figure 5.14**). For At-E (-1), At-C (-2) and Al-C (-3), we see the values of D are unaffected by ionic strength up to ~150 mM KCl. At higher ionic strength (>200 mM), all three probes increase in apparent diffusion coefficient. For example, At-E (-1) has D values of 90 ± 5 $\mu\text{m}^2/\text{s}$ at low ionic strength but increases by 20% to 113 ± 4 $\mu\text{m}^2/\text{s}$ at high ionic strength. Al-C (-3) similarly increases 26% from $D = 73 \pm 3$ $\mu\text{m}^2/\text{s}$ inside droplets formed below 200 mM KCl, to 99 ± 4 $\mu\text{m}^2/\text{s}$ above 200 mM. Even the larger protein probe Alexa-BSA (-15 charge) showed similar transport behavior inside the droplet with an apparent change in D of 20% with increasing KCl from $D = 13 \pm 5$ $\mu\text{m}^2/\text{s}$ below 200 mM KCl to $D = 33 \pm 7$ $\mu\text{m}^2/\text{s}$ at high salt concentrations. None of the charged probes show a change in D with increasing salt concentration in tau solutions over

this same KCl concentration range. This data suggests similar charge screening effects are observed for all 4 of our charged probe molecules inside the tau droplets. Most likely the Debye screening lengths inside the tau droplets are sufficiently reduced above 200 mM salt resulting in an increased probe diffusion. Interestingly, this ionic strength effect is not significantly affected by the overall probe molecule charge for probes small relative to the tau droplet mesh size.

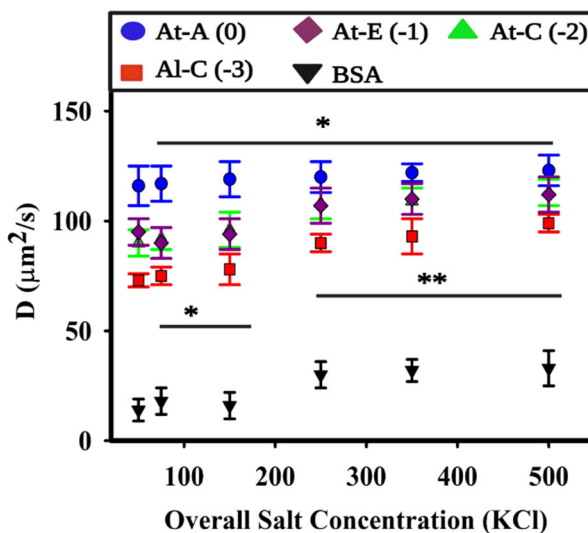


Figure 5.14 Ionic strength effect on translational diffusion for dye molecules At-A (0) through Al-C (-3) and Alexa labelled BSA protein in tau condensates. Debye screening of all charged probes exhibits slight rise in D values till ~ 250 mM KCl in condensates is observed whereas the transport is highly unaffected for uncharged zwitterionic probe with increase of overall salt concentrations. * $p > 0.05$ vs D of 50 mM salt concentration for uncharged probe, * $p > 0.05$ ** $p < 0.001$ vs D of 50 mM salt concentration for all charged probes studied.

5.4 Conclusion

It is recognized that the protein droplets that are formed via phase separation exhibit properties that allow molecular reactants to become concentrated in one place in the cell for promotion of various reactions.^{31, 326} This has ramifications for biology as the formation of tau protein droplets may facilitate processes such as the nucleation of microtubules.

Despite its potential biological significance, few experiments have directly probed the transport properties of particles inside tau protein condensates. Using FCS we analyzed the translational diffusion coefficients of various probe dye molecules in liquid-liquid phase separated tau droplets. Our results show that tau condensate formation results in a ~10-fold concentration increase of probe molecules inside the tau droplet compared to outside due to favorable partitioning in the dense phase. The probes also show a hindered diffusion that is dependent on the particle net charge with more highly charged probes interacting more strongly with tau molecules inside the condensed phase. This charge dependence indicates the importance of electrostatic interactions operating between probe molecules and tau protein chains. Estimates of the relevant structural length scales within the tau droplet suggest the tau droplet, while high in tau protein concentration, is consistent with a solvent rich, low density, semidilute polymer solution. We show that the relevant polymer length scales inside the tau droplet are large relative to both the probes and a much larger BSA protein molecule. Both probe molecules and BSA are observed to freely diffuse within the tau condensate. Using measurements of the apparent microviscosity from a neutral probe molecule, we can estimate the diffusional coefficient for probes and BSA inside the tau droplet and find good agreement with experiments. Changes in solution strength for both charged probes and BSA show a crossover behavior at near physiological salt concentrations. We have shown how molecular charge and ionic strength control the transport and recruitment of particles and proteins within tau droplets. The ability to tune and control these interactions in protein droplets *in vivo* is likely to have important consequences for the biological function of these organelles.

References

1. Edidin, M., Lipids on the frontier: a century of cell-membrane bilayers. *Nat Rev Mol Cell Biol* **2003**, *4* (5), 414-8.
2. Schmidt, H. B.; Görlich, D., Transport Selectivity of Nuclear Pores, Phase Separation, and Membraneless Organelles. *Trends in biochemical sciences* **2016**, *41* (1), 46-61.
3. Krestova, M.; Garcia-Sierra, F.; Bartos, A.; Ricny, J.; Ripova, D., Structure and Pathology of Tau Protein in Alzheimer Disease. *International journal of Alzheimer's disease* **2012**, *2012*, 731526.
4. Lane, L. A.; Qian, X.; Smith, A. M.; Nie, S. J. A. r. o. p. c., Physical chemistry of nanomedicine: understanding the complex behaviors of nanoparticles in vivo. **2015**, *66*, 521-547.
5. Hernández-Vega, A.; Braun, M.; Scharrel, L.; Jahnel, M.; Wegmann, S.; Hyman, B. T.; Alberti, S.; Diez, S.; Hyman, A. A., Local Nucleation of Microtubule Bundles through Tubulin Concentration into a Condensed Tau Phase. *Cell reports (Cambridge)* **2017**, *20* (10), 2304-2312.
6. Ahmed, E. M., Hydrogel: Preparation, characterization, and applications: A review. *Journal of Advanced Research* **2015**, *6* (2), 105-121.
7. Schiller, J. L.; Lai, S. K., Tuning Barrier Properties of Biological Hydrogels. *ACS applied bio materials* **2020**, *3* (5), 2875-2890.
8. Parhi, R., Cross-Linked Hydrogel for Pharmaceutical Applications: A Review. *Adv Pharm Bull* **2017**, *7* (4), 515-530.
9. Lieleg, O.; Ribbeck, K. J. T. i. c. b., Biological hydrogels as selective diffusion barriers. **2011**, *21* (9), 543-551.
10. Lieleg, O.; Ribbeck, K., Biological hydrogels as selective diffusion barriers. *Trends in Cell Biology* **2011**, *21* (9), 543-551.
11. Orell, A.; Fröls, S.; Albers, S.-V., Archaeal Biofilms: The Great Unexplored. *Annual review of microbiology* **2013**, *67* (1), 337-354.
12. Flemming, H.-C.; Wingender, J., The biofilm matrix. *Nature reviews. Microbiology* **2010**, *8* (9), 623-633.
13. Flemming, H.-C.; Neu, T. R.; Wozniak, D. J., The EPS matrix: the "house of biofilm cells". *Journal of bacteriology* **2007**, *189* (22), 7945-7947.
14. Vu, B.; Chen, M.; Crawford, R. J.; Ivanova, E. P., Bacterial extracellular polysaccharides involved in biofilm formation. *Molecules (Basel, Switzerland)* **2009**, *14* (7), 2535-2554.
15. Bansil, R.; Stanley, E.; Lamont, J. T., Mucin Biophysics. *Annual Review of Physiology* **1995**, *57* (1), 635-657.
16. Gendler, S. J.; Spicer, A. P., Epithelial mucin genes. *Annu Rev Physiol* **1995**, *57*, 607-34.
17. Ensign, L. M.; Schneider, C.; Suk, J. S.; Cone, R.; Hanes, J., Mucus Penetrating Nanoparticles: Biophysical Tool and Method of Drug and Gene Delivery. *Advanced materials (Weinheim)* **2012**, *24* (28), 3887-3894.
18. Ensign, L. M.; Tang, B. C.; Wang, Y.-Y.; Terence, A. T.; Hoen, T.; Cone, R.; Hanes, J. J. S. t. m., Mucus-penetrating nanoparticles for vaginal drug delivery protect against herpes simplex virus. **2012**, *4* (138), 138ra79-138ra79.
19. Knowles, M. R.; Boucher, R. C., Mucus clearance as a primary innate defense mechanism for mammalian airways. *J Clin Invest* **2002**, *109* (5), 571-577.
20. Netsomboon, K.; Bernkop-Schnürch, A., Mucoadhesive vs. mucopenetrating particulate drug delivery. *European Journal of Pharmaceutics and Biopharmaceutics* **2016**, *98*, 76-89.

21. Strambio-De-Castillia, C.; Niepel, M.; Rout, M. P., The nuclear pore complex: bridging nuclear transport and gene regulation. *Nature Reviews Molecular Cell Biology* **2010**, *11* (7), 490-501.
22. Schmidt, H. B.; Görlich, D., Transport Selectivity of Nuclear Pores, Phase Separation, and Membraneless Organelles. *Trends in biochemical sciences* **2016**, *41* (1), 46-61.
23. Görlich, D.; Kutay, U., Transport Between the Cell Nucleus and the Cytoplasm. *Annual Review of Cell and Developmental Biology* **1999**, *15* (1), 607-660.
24. Rexach, M.; Blobel, G., Protein import into nuclei: association and dissociation reactions involving transport substrate, transport factors, and nucleoporins. *Cell* **1995**, *83* (5), 683-92.
25. Colwell, L. J.; Brenner, M. P.; Ribbeck, K., Charge as a Selection Criterion for Translocation through the Nuclear Pore Complex (Charge as a Selection Criterion). *PLoS Computational Biology* **2010**, *6* (4), e1000747.
26. Rout, M. P.; Wenthe, S. R., Pores for thought: nuclear pore complex proteins. *Trends in Cell Biology* **1994**, *4* (10), 357-365.
27. Denning, D. P.; Patel, S. S.; Uversky, V.; Fink, A. L.; Rexach, M., Disorder in the nuclear pore complex: the FG repeat regions of nucleoporins are natively unfolded. *Proc Natl Acad Sci U S A* **2003**, *100* (5), 2450-5.
28. Moussavi-Baygi, R.; Mofrad, M. R. K., Rapid Brownian Motion Primes Ultrafast Reconstruction of Intrinsically Disordered Phe-Gly Repeats Inside the Nuclear Pore Complex. *Scientific Reports* **2016**, *6* (1), 29991.
29. Forman-Kay, Julie D.; Mittag, T., From Sequence and Forces to Structure, Function, and Evolution of Intrinsically Disordered Proteins. *Structure (London)* **2013**, *21* (9), 1492-1499.
30. Kato, M.; Han, Tina W.; Xie, S.; Shi, K.; Du, X.; Wu, Leeju C.; Mirzaei, H.; Goldsmith, Elizabeth J.; Longgood, J.; Pei, J.; Grishin, Nick V.; Frantz, Douglas E.; Schneider, Jay W.; Chen, S.; Li, L.; Sawaya, Michael R.; Eisenberg, D.; Tycko, R.; McKnight, Steven L., Cell-free Formation of RNA Granules: Low Complexity Sequence Domains Form Dynamic Fibers within Hydrogels. *Cell (Cambridge)* **2012**, *149* (4), 753-767.
31. Hyman, A. A.; Weber, C. A.; Jülicher, F., Liquid-Liquid Phase Separation in Biology. *Annual review of cell and developmental biology* **2014**, *30* (1), 39-58.
32. Alberti, S.; Gladfelter, A.; Mittag, T., Considerations and Challenges in Studying Liquid-Liquid Phase Separation and Biomolecular Condensates. *Cell* **2019**, *176* (3), 419-434.
33. Shin, Y.; Brangwynne, C. P., Liquid phase condensation in cell physiology and disease. *Science (American Association for the Advancement of Science)* **2017**, *357* (6357), eaaf4382.
34. Ciofu, O.; Tolker-Nielsen, T.; Jensen, P. Ø.; Wang, H.; Høiby, N., Antimicrobial resistance, respiratory tract infections and role of biofilms in lung infections in cystic fibrosis patients. *Advanced drug delivery reviews* **2015**, *85*, 7-23.
35. Lewis, K., Persister cells, dormancy and infectious disease. *Nature reviews. Microbiology* **2007**, *5* (1), 48-56.
36. Marshall, C. W., III; Frank, R.; Amandine, B.; Michael, J. F.; Philip, S. S., Contributions of Antibiotic Penetration, Oxygen Limitation, and Low Metabolic Activity to Tolerance of *Pseudomonas aeruginosa* Biofilms to Ciprofloxacin and Tobramycin. *Antimicrobial Agents and Chemotherapy* **2003**, *47* (1), 317-323.
37. Schuster, B. S.; Suk, J. S.; Woodworth, G. F.; Hanes, J., Nanoparticle diffusion in respiratory mucus from humans without lung disease. *Biomaterials* **2013**, *34* (13), 3439-3446.
38. George, A.; Edward, B. B.; Ricky, T. T.; Trevor, D. M.; Robert, B. C.; Yves, B.; Rakesh, K. J., Two-photon fluorescence correlation microscopy reveals the two-phase nature of transport in tumors. *Nature Medicine* **2004**, *10* (2), 203.

39. Williams, R. M.; Zipfel, W. R.; Tinsley, M. L.; Farnum, C. E., Solute Transport in Growth Plate Cartilage: In Vitro and In Vivo. *Biophysical Journal* **2007**, *93* (3), 1039-1050.
40. Eibauer, M.; Pellanda, M.; Turgay, Y.; Dubrovsky, A.; Wild, A.; Medalia, O., Structure and gating of the nuclear pore complex. *Nature Communications* **2015**, *6* (1), 7532.
41. Fried, H.; Kutay, U., Nucleocytoplasmic transport: taking an inventory. *Cellular and molecular life sciences : CMLS* **2003**, *60* (8), 1659-88.
42. Gomes, E.; Shorter, J., The molecular language of membraneless organelles. *The Journal of biological chemistry* **2019**, *294* (18), 7115-7127.
43. Gong, J. P., Friction and lubrication of hydrogels—its richness and complexity. *Soft Matter* **2006**, *2* (7), 544-552.
44. Bansil, R.; Turner, B. S., The biology of mucus: Composition, synthesis and organization. *Adv Drug Deliv Rev* **2018**, *124*, 3-15.
45. Thornton, D.; Rousseau, K.; McGuckin, M., Structure and Function of the Polymeric Mucins in Airways Mucus. *Annual Review of Physiology* **2008**, *70*, 459.
46. Bansil, R.; Turner, B. S., Mucin structure, aggregation, physiological functions and biomedical applications. *Current Opinion in Colloid & Interface Science* **2006**, *11* (2), 164-170.
47. Kreda, S. M.; Davis, C. W.; Rose, M. C., CFTR, mucins, and mucus obstruction in cystic fibrosis. *Cold Spring Harb Perspect Med* **2012**, *2* (9), a009589-a009589.
48. Jennings, L. K.; Storek, K. M.; Ledvina, H. E.; Coulon, C.; Marmont, L. S.; Sadovskaya, I.; Secor, P. R.; Tseng, B. S.; Scian, M.; Filloux, A.; Wozniak, D. J.; Howell, P. L.; Parsek, M. R., Pel is a cationic exopolysaccharide that cross-links extracellular DNA in the *Pseudomonas aeruginosa* biofilm matrix. *Proceedings of the National Academy of Sciences of the United States of America* **2015**, *112* (36), 11353-11358.
49. Byrd, M. S.; Sadovskaya, I.; Vinogradov, E.; Lu, H.; Sprinkle, A. B.; Richardson, S. H.; Ma, L.; Ralston, B.; Parsek, M. R.; Anderson, E. M.; Lam, J. S.; Wozniak, D. J., Genetic and biochemical analyses of the *Pseudomonas aeruginosa* Psl exopolysaccharide reveal overlapping roles for polysaccharide synthesis enzymes in Psl and LPS production. *Molecular Microbiology* **2009**, *73* (4), 622-638.
50. Sutherland, I. W., Biofilm exopolysaccharides : a strong and sticky framework. *Microbiology (Society for General Microbiology)* **2001**, *147* (Pt 1), 3-9.
51. Mack, D.; Fischer, W.; Krokotsch, A.; Leopold, K.; Hartmann, R.; Egge, H.; Laufs, R., The intercellular adhesin involved in biofilm accumulation of *Staphylococcus epidermidis* is a linear beta-1,6-linked glucosaminoglycan: purification and structural analysis. *Journal of Bacteriology* **1996**, *178* (1), 175-183.
52. Colwell, L. J.; Brenner, M. P.; Ribbeck, K., Charge as a selection criterion for translocation through the nuclear pore complex. *PLoS computational biology* **2010**, *6* (4), e1000747-e1000747.
53. Kwon, I.; Kato, M.; Xiang, S.; Wu, L.; Theodoropoulos, P.; Mirzaei, H.; Han, T.; Xie, S.; Corden, Jeffrey L.; McKnight, Steven L., Phosphorylation-Regulated Binding of RNA Polymerase II to Fibrous Polymers of Low-Complexity Domains. *Cell (Cambridge)* **2013**, *155* (5), 1049-1060.
54. Shorter, J., Prion-like Domains Program Ewing's Sarcoma. *Cell* **2017**, *171* (1), 30-31.
55. Boija, A.; Klein, I. A.; Sabari, B. R.; Dall'Agnesse, A.; Coffey, E. L.; Zamudio, A. V.; Li, C. H.; Shrinivas, K.; Manteiga, J. C.; Hannett, N. M.; Abraham, B. J.; Afeyan, L. K.; Guo, Y. E.; Rimel, J. K.; Fant, C. B.; Schuijers, J.; Lee, T. I.; Taatjes, D. J.; Young, R. A., Transcription Factors Activate Genes through the Phase-Separation Capacity of Their Activation Domains. *Cell* **2018**, *175* (7), 1842-1855.e16.
56. Larson, A. G.; Elnatan, D.; Keenen, M. M.; Trnka, M. J.; Johnston, J. B.; Burlingame, A. L.; Agard, D. A.; Redding, S.; Narlikar, G. J., Liquid droplet formation by HP1 α suggests a role for phase separation in heterochromatin. *Nature* **2017**, *547* (7662), 236-240.

57. Strom, A. R.; Emelyanov, A. V.; Mir, M.; Fyodorov, D. V.; Darzacq, X.; Karpen, G. H., Phase separation drives heterochromatin domain formation. *Nature* **2017**, *547* (7662), 241-245.
58. Banani, S. F.; Rice, A. M.; Peeples, W. B.; Lin, Y.; Jain, S.; Parker, R.; Rosen, M. K., Compositional Control of Phase-Separated Cellular Bodies. *Cell* **2016**, *166* (3), 651-663.
59. Ferrolino, M. C.; Mitrea, D. M.; Michael, J. R.; Kriwacki, R. W., Compositional adaptability in NPM1-SURF6 scaffolding networks enabled by dynamic switching of phase separation mechanisms. *Nature Communications* **2018**, *9* (1), 5064.
60. Riback, J. A.; Zhu, L.; Ferrolino, M. C.; Tolbert, M.; Mitrea, D. M.; Sanders, D. W.; Wei, M.-T.; Kriwacki, R. W.; Brangwynne, C. P., Composition-dependent thermodynamics of intracellular phase separation. *Nature* **2020**, *581* (7807), 209-214.
61. Lieleg, O.; Vladescu, I.; Ribbeck, K., Characterization of Particle Translocation through Mucin Hydrogels. *Biophysical Journal* **2010**, *98* (9), 1782-1789.
62. Netti, P. A.; Berk, D. A.; Swartz, M. A.; Grodzinsky, A. J.; Jain, R. K., Role of extracellular matrix assembly in interstitial transport in solid tumors. *Cancer research* **2000**, *60* (9), 2497-503.
63. Lai, S. K.; Wang, Y. Y.; Hida, K.; Cone, R.; Hanes, J., Nanoparticles reveal that human cervicovaginal mucus is riddled with pores larger than viruses. *Proceedings of the National Academy of Sciences of the United States of America* **2010**, *107* (2), 598-603.
64. Birjiniuk, A.; Billings, N.; Nance, E.; Hanes, J.; Ribbeck, K.; Doyle, P. S., Single particle tracking reveals spatial and dynamic organization of the Escherichia coli biofilm matrix. *New journal of physics* **2014**, *16* (8).
65. Crater, J. S.; Carrier, R. L., Barrier properties of gastrointestinal mucus to nanoparticle transport. *Macromolecular bioscience* **2010**, *10* (12), 1473-83.
66. Wühr, M.; Güttler, T.; Peshkin, L.; McAlister, G. C.; Sonnett, M.; Ishihara, K.; Groen, A. C.; Presler, M.; Erickson, B. K.; Mitchison, T. J.; Kirschner, M. W.; Gygi, S. P., The Nuclear Proteome of a Vertebrate. *Current biology : CB* **2015**, *25* (20), 2663-71.
67. Güttler, T.; Frey, S.; Mohr, D.; Görlich, D.; Fischer, T., Characterisation of the passive permeability barrier of nuclear pore complexes. *The EMBO journal* **2009**, *28* (17), 2541-2553.
68. Li, Leon D.; Crouzier, T.; Sarkar, A.; Dunphy, L.; Han, J.; Ribbeck, K., Spatial Configuration and Composition of Charge Modulates Transport into a Mucin Hydrogel Barrier. *Biophysical Journal* **2013**, *105* (6), 1357-1365.
69. Lieleg, O.; Baumgärtel, R. M.; Bausch, A. R., Selective filtering of particles by the extracellular matrix: an electrostatic bandpass. *Biophysical journal* **2009**, *97* (6), 1569-1577.
70. Hansing, J.; Netz, R. R., Particle Trapping Mechanisms Are Different in Spatially Ordered and Disordered Interacting Gels. *Biophys J* **2018**, *114* (11), 2653-2664.
71. Carlstedt, I.; Sheehan, J. K., Macromolecular properties and polymeric structure of mucus glycoproteins. *Ciba Foundation symposium* **1984**, *109*, 157-72.
72. Thornton, D. J.; Rousseau, K.; McGuckin, M. A., Structure and function of the polymeric mucins in airways mucus. *Annu Rev Physiol* **2008**, *70*, 459-86.
73. Abdulkarim, M.; Agulló, N.; Cattoz, B.; Griffiths, P.; Bernkop-Schnürch, A.; Borros, S. G.; Gumbleton, M., Nanoparticle diffusion within intestinal mucus: Three-dimensional response analysis dissecting the impact of particle surface charge, size and heterogeneity across polyelectrolyte, pegylated and viral particles. *European journal of pharmaceuticals and biopharmaceutics : official journal of Arbeitsgemeinschaft fur Pharmazeutische Verfahrenstechnik e.V* **2015**, *97* (Pt A), 230-8.
74. Dawson, M.; Wirtz, D.; Hanes, J., Enhanced viscoelasticity of human cystic fibrotic sputum correlates with increasing microheterogeneity in particle transport. *J Biol Chem* **2003**, *278* (50), 50393-401.

75. Lai, S. K.; Hanlon, D. E.; Harrold, S.; Man, S. T.; Wang, Y.-Y.; Cone, R.; Hanes, J., Rapid transport of large polymeric nanoparticles in fresh undiluted human mucus. *Proceedings of the National Academy of Sciences* **2007**, *104* (5), 1482.
76. Lai, S. K.; Hida, K.; Shukair, S.; Wang, Y. Y.; Figueiredo, A.; Cone, R.; Hope, T. J.; Hanes, J., Human immunodeficiency virus type 1 is trapped by acidic but not by neutralized human cervicovaginal mucus. *Journal of virology* **2009**, *83* (21), 11196-200.
77. Broughton-Head, V. J.; Shur, J.; Carroll, M. P.; Smith, J. R.; Shute, J. K., Unfractionated heparin reduces the elasticity of sputum from patients with cystic fibrosis. *American journal of physiology. Lung cellular and molecular physiology* **2007**, *293* (5), L1240-9.
78. Bouvet, J. P.; Grésenguet, G.; Bélec, L., Vaginal pH neutralization by semen as a cofactor of HIV transmission. *Clinical microbiology and infection : the official publication of the European Society of Clinical Microbiology and Infectious Diseases* **1997**, *3* (1), 19-23.
79. Brunelli, R.; Papi, M.; Arcovito, G.; Bompiani, A.; Castagnola, M.; Parasassi, T.; Sampaiolese, B.; Vincenzoni, F.; De Spirito, M., Globular structure of human ovulatory cervical mucus. *FASEB journal : official publication of the Federation of American Societies for Experimental Biology* **2007**, *21* (14), 3872-6.
80. Flemming, H.-C.; Wingender, J., The biofilm matrix. *Nature Reviews Microbiology* **2010**, *8* (9), 623-633.
81. Kanwar, Y. S.; Linker, A.; Farquhar, M. G., Increased permeability of the glomerular basement membrane to ferritin after removal of glycosaminoglycans (heparan sulfate) by enzyme digestion. *The Journal of cell biology* **1980**, *86* (2), 688-93.
82. Zámecník, J.; Vargová, L.; Homola, A.; Kodet, R.; Syková, E., Extracellular matrix glycoproteins and diffusion barriers in human astrocytic tumours: Extracellular matrix in astrocytomas. *Neuropathology and applied neurobiology* **2004**, *30* (4), 338-350.
83. Taipale, J.; Keski-Oja, J., Growth factors in the extracellular matrix. *FASEB journal : official publication of the Federation of American Societies for Experimental Biology* **1997**, *11* (1), 51-9.
84. Thorne, R. G.; Lakkaraju, A.; Rodriguez-Boulan, E.; Nicholson, C., & In vivo diffusion of lactoferrin in brain extracellular space is regulated by interactions with heparan sulfate. *Proceedings of the National Academy of Sciences* **2008**, *105* (24), 8416.
85. Dowd, C. J.; Cooney, C. L.; Nugent, M. A., Heparan sulfate mediates bFGF transport through basement membrane by diffusion with rapid reversible binding. *J Biol Chem* **1999**, *274* (8), 5236-44.
86. Jastrebova, N.; Vanwildemeersch, M.; Rapraeger, A. C.; Giménez-Gallego, G.; Lindahl, U.; Spillmann, D., Heparan sulfate-related oligosaccharides in ternary complex formation with fibroblast growth factors 1 and 2 and their receptors. *J Biol Chem* **2006**, *281* (37), 26884-92.
87. Kreuger, J.; Spillmann, D.; Li, J.-p.; Lindahl, U., Interactions between heparan sulfate and proteins: the concept of specificity. *The Journal of cell biology* **2006**, *174* (3), 323-327.
88. Stewart, P. S., A review of experimental measurements of effective diffusive permeabilities and effective diffusion coefficients in biofilms. *Biotechnology and Bioengineering* **1998**, *59* (3), 261-272.
89. Abdi-Ali, A.; Mohammadi-Mehr, M.; Agha Alaei, Y., Bactericidal activity of various antibiotics against biofilm-producing *Pseudomonas aeruginosa*. *International journal of antimicrobial agents* **2006**, *27* (3), 196-200.
90. Shigeta, M.; Tanaka, G.; Komatsuzawa, H.; Sugai, M.; Suginaka, H.; Usui, T., Permeation of antimicrobial agents through *Pseudomonas aeruginosa* biofilms: a simple method. *Chemotherapy* **1997**, *43* (5), 340-5.
91. Walters, M. C., 3rd; Roe, F.; Bugnicourt, A.; Franklin, M. J.; Stewart, P. S., Contributions of antibiotic penetration, oxygen limitation, and low metabolic activity to tolerance of

- Pseudomonas aeruginosa* biofilms to ciprofloxacin and tobramycin. *Antimicrobial agents and chemotherapy* **2003**, *47* (1), 317-23.
92. Jovanovic-Taliman, T.; Tetenbaum-Novatt, J.; McKenney, A. S.; Zilman, A.; Peters, R.; Rout, M. P.; Chait, B. T., Artificial nanopores that mimic the transport selectivity of the nuclear pore complex. *Nature* **2009**, *457* (7232), 1023-1027.
93. Frey, S.; Görlich, D., A saturated FG-repeat hydrogel can reproduce the permeability properties of nuclear pore complexes. *Cell* **2007**, *130* (3), 512-23.
94. Ribbeck, K.; Görlich, D., Kinetic analysis of translocation through nuclear pore complexes. *The EMBO journal* **2001**, *20* (6), 1320-1330.
95. Jäkel, S.; Görlich, D., Importin beta, transportin, RanBP5 and RanBP7 mediate nuclear import of ribosomal proteins in mammalian cells. *The EMBO journal* **1998**, *17* (15), 4491-4502.
96. Jäkel, S.; Albig, W.; Kutay, U.; Bischoff, F. R.; Schwamborn, K.; Doenecke, D.; Görlich, D., The importin beta/importin 7 heterodimer is a functional nuclear import receptor for histone H1. *The EMBO journal* **1999**, *18* (9), 2411-2423.
97. Bonner, W. M., Protein migration into nuclei. I. Frog oocyte nuclei in vivo accumulate microinjected histones, allow entry to small proteins, and exclude large proteins. *J Cell Biol* **1975**, *64* (2), 421-30.
98. Ribbeck, K.; Görlich, D., The permeability barrier of nuclear pore complexes appears to operate via hydrophobic exclusion. *Embo j* **2002**, *21* (11), 2664-71.
99. Weis, K., The nuclear pore complex: oily spaghetti or gummy bear? *Cell* **2007**, *130* (3), 405-7.
100. Naim, B.; Reich, Z.; Zbaida, D.; Kapon, R.; Dagan, S., Cargo surface hydrophobicity is sufficient to overcome the nuclear pore complex selectivity barrier. *The EMBO journal* **2009**, *28* (18), 2697-2705.
101. Bayliss, R.; Littlewood, T.; Stewart, M., Structural basis for the interaction between FxFG nucleoporin repeats and importin-beta in nuclear trafficking. *Cell* **2000**, *102* (1), 99-108.
102. Updike, D.; Strome, S., P granule assembly and function in *Caenorhabditis elegans* germ cells. *Journal of andrology* **2010**, *31* (1), 53-60.
103. Updike, D. L.; Hachey, S. J.; Kreher, J.; Strome, S., P granules extend the nuclear pore complex environment in the *C. elegans* germ line. *Journal of Cell Biology* **2011**, *192* (6), 939-948.
104. Voronina, E.; Seydoux, G., The *C. elegans* homolog of nucleoporin Nup98 is required for the integrity and function of germline P granules. *Development* **2010**, *137* (9), 1441.
105. Hondele, M.; Heinrich, S.; De Los Rios, P.; Weis, K., Membraneless organelles: phasing out of equilibrium. *Emerging topics in life sciences* **2020**, *4* (3), 331-342.
106. Woodruff, J. B.; Ferreira Gomes, B.; Widlund, P. O.; Mahamid, J.; Honigsmann, A.; Hyman, A. A., The Centrosome Is a Selective Condensate that Nucleates Microtubules by Concentrating Tubulin. *Cell (Cambridge)* **2017**, *169* (6), 1066-1077.e10.
107. Nott, T. J.; Craggs, T. D.; Baldwin, A. J., Membraneless organelles can melt nucleic acid duplexes and act as biomolecular filters. *Nature Chemistry* **2016**, *8* (6), 569-575.
108. Nott, Timothy J.; Petsalaki, E.; Farber, P.; Jervis, D.; Fussner, E.; Plochowitz, A.; Craggs, T. D.; Bazett-Jones, David P.; Pawson, T.; Forman-Kay, Julie D.; Baldwin, Andrew J., Phase Transition of a Disordered Nuage Protein Generates Environmentally Responsive Membraneless Organelles. *Molecular cell* **2015**, *57* (5), 936-947.
109. Zhang, X.; Hansing, J.; Netz, R. R.; DeRouchey, J. E. J. B. j., Particle transport through hydrogels is charge asymmetric. **2015**, *108* (3), 530-539.

110. Zhang, X. Nanoparticle behavior in biological gels and biofluids: The impact of interactions with charged biogels and the formation of protein coronas on nanoparticles. University of Kentucky, 2015.
111. Hansing, J.; Duke, J. R.; Fryman, E. B.; DeRouchey, J. E.; Netz, R. R., Particle Diffusion in Polymeric Hydrogels with Mixed Attractive and Repulsive Interactions. *Nano Letters* **2018**, *18* (8), 5248-5256.
112. Magde, D.; Elson, E.; Webb, W. W., Thermodynamic Fluctuations in a Reacting System—Measurement by Fluorescence Correlation Spectroscopy. *Physical review letters* **1972**, *29* (11), 705-708.
113. Magde, D.; Elson, E. L.; Webb, W. W., Fluorescence correlation spectroscopy. II. An experimental realization. *Biopolymers* **1974**, *13* (1), 29-61.
114. Elson, E. L.; Magde, D., Fluorescence correlation spectroscopy. I. Conceptual basis and theory. *Biopolymers* **1974**, *13* (1), 1-27.
115. Rigler, R.; Elson, E. S., *Fluorescence correlation spectroscopy: theory and applications*. Springer Science & Business Media: 2012; Vol. 65.
116. Rigler, R.; Mets, Ü.; Widengren, J.; Kask, P., Fluorescence correlation spectroscopy with high count rate and low background : analysis of translational diffusion. *European biophysics journal* **1993**, *22* (3), 169-175.
117. Schwille, P., There and back again: from the origin of life to single molecules. *Eur Biophys J* **2018**, *47* (4), 493-498.
118. Muetze, J.; Ohrt, T.; Schwille, P., Fluorescence correlation spectroscopy in vivo. *Laser and Photonics Reviews*, v.5, 52-67 (2011) **2011**, 5.
119. Haustein, E.; Schwille, P., Fluorescence Correlation Spectroscopy: Novel Variations of an Established Technique. *Annual Review of Biophysics and Biomolecular Structure* **2007**, *36* (1), 151-169.
120. Hess, S. T.; Huang, S.; Heikal, A. A.; Webb, W. W., Biological and Chemical Applications of Fluorescence Correlation Spectroscopy: A Review. *Biochemistry (Easton)* **2002**, *41* (3), 697-705.
121. Tian, Y.; Martinez, M. M.; Pappas, D., Fluorescence Correlation Spectroscopy: A Review of Biochemical and Microfluidic Applications. *Applied spectroscopy* **2011**, *65* (4), 115A-115A.
122. Haustein, E.; Schwille, P., Ultrasensitive investigations of biological systems by fluorescence correlation spectroscopy. *Methods (San Diego, Calif.)* **2003**, *29* (2), 153-166.
123. Papadakis, C. M.; Košován, P.; Richtering, W.; Wöll, D., Polymers in focus: fluorescence correlation spectroscopy. *Colloid and polymer science* **2014**, *292* (10), 2399-2411.
124. Wöll, D., Fluorescence correlation spectroscopy in polymer science. *Rsc Advances* **2014**, *4* (5), 2447-2465.
125. Wöll, D., Fluorescence Correlation Spectroscopy Studies of Polymer Systems. In *Fluorescence Studies of Polymer Containing Systems*, Procházka, K., Ed. Springer International Publishing: Cham, 2016; pp 255-297.
126. Krichevsky, O.; Bonnet, G., Fluorescence correlation spectroscopy: the technique and its applications. *Reports on Progress in Physics* **2002**, *65* (2), 251.
127. Ermolaev, V. L., Ultrafast nonradiative transitions between higher excited states in organic molecules. *Russian Chemical Reviews* **2001**, *70* (6), 471-490.
128. Procházka, K., *Fluorescence studies of polymer containing systems*. Springer: 2016; Vol. 16.
129. Skoog, D. A.; Holler, F. J.; Crouch, S. R., *Principles of instrumental analysis*. Cengage learning: 2017.
130. Cremoux, B. D., Avalanche photo-diodes. Google Patents: 1976.

131. Van Rompaey, E.; Engelborghs, Y.; Sanders, N.; De Smedt, S. C.; Demeester, J., Interactions Between Oligonucleotides and Cationic Polymers Investigated by fluorescence Correlation Spectroscopy. *Pharmaceutical research* **2001**, *18* (7), 928-936.
132. Jia, P.; Yang, Q.; Gong, Y.; Zhao, J., Dynamic exchange of counterions of polystyrene sulfonate. *The Journal of chemical physics* **2012**, *136* (8), 084904-084904-7.
133. Lee, J. I.; Sato, M.; Ushida, K.; Mochida, J., Measurement of diffusion in articular cartilage using fluorescence correlation spectroscopy. *BMC biotechnology* **2011**, *11* (1), 19-19.
134. Sprague, B. L.; Müller, F.; Pego, R. L.; Bungay, P. M.; Stavreva, D. A.; McNally, J. G., Analysis of Binding at a Single Spatially Localized Cluster of Binding Sites by Fluorescence Recovery after Photobleaching. *Biophysical Journal* **2006**, *91* (4), 1169-1191.
135. Day, R. N.; Schaufele, F., Imaging Molecular Interactions in Living Cells. *Molecular Endocrinology* **2005**, *19* (7), 1675-1686.
136. Zhang, Z.; Yomo, D.; Gradinaru, C., Choosing the right fluorophore for single-molecule fluorescence studies in a lipid environment. *Biochimica et biophysica acta. Biomembranes* **2017**, *1859* (7), 1242-1253.
137. Van der Walle, C.; ClinicalKey, *Peptide and protein delivery*. 1st ed. ed.; London

San Diego, Calif. : Academic Press: London

San Diego, Calif.

San Diego, CA, 2011.

138. Sakiyama, T.; Tsutsui, T.; Masuda, E.; Imamura, K.; Nakanishi, K., Ionization Characteristics of Polyelectrolyte Complex Gels: Analysis Based on Their Swelling Behaviors. *Macromolecules* **2003**, *36* (13), 5039-5042.
139. Pristiniski, D.; Kozlovskaya, V.; Sukhishvili, S. A., Fluorescence correlation spectroscopy studies of diffusion of a weak polyelectrolyte in aqueous solutions. *The Journal of chemical physics* **2005**, *122* (1), 14907-14907.
140. Kim, B.-S.; Lebedeva, O. V.; Koynov, K.; Gong, H.; Glasser, G.; Lieberwith, I.; Vinogradova, O. I., Effect of Organic Solvent on the Permeability and Stiffness of Polyelectrolyte Multilayer Microcapsules. *Macromolecules* **2005**, *38* (12), 5214-5222.
141. Arrio-Dupont, M.; Foucault, G.; Vacher, M.; Devaux, P. F.; Cribier, S., Translational diffusion of globular proteins in the cytoplasm of cultured muscle cells. *Biophys J* **2000**, *78* (2), 901-7.
142. Seksek, O.; Biwersi, J.; Verkman, A. S., Translational diffusion of macromolecule-sized solutes in cytoplasm and nucleus. *J Cell Biol* **1997**, *138* (1), 131-42.
143. Weiss, M.; Elsner, M.; Kartberg, F.; Nilsson, T., Anomalous subdiffusion is a measure for cytoplasmic crowding in living cells. *Biophysical journal* **2004**, *87* (5), 3518-3524.
144. Politz, J. C.; Browne, E. S.; Wolf, D. E.; Pederson, T., Intranuclear diffusion and hybridization state of oligonucleotides measured by fluorescence correlation spectroscopy in living cells. *Proceedings of the National Academy of Sciences* **1998**, *95* (11), 6043.
145. Vishwasrao, H. D.; Heikal, A. A.; Kasischke, K. A.; Webb, W. W. J. o. B. C., Conformational dependence of intracellular NADH on metabolic state revealed by associated fluorescence anisotropy. **2005**, *280* (26), 25119-25126.
146. Elson, E. L.; Schlessinger, J.; Koppel, D. E.; Axelrod, D.; Webb, W. W., Measurement of lateral transport on cell surfaces. *Progress in clinical and biological research* **1976**, *9*, 137-47.
147. Webb, W. W.; Barak, L. S.; Tank, D. W.; Wu, E. S., Molecular mobility on the cell surface. *Biochemical Society symposium* **1981**, (46), 191-205.

148. Saffman, P. G.; Delbrück, M., Brownian motion in biological membranes. *Proceedings of the National Academy of Sciences* **1975**, *72* (8), 3111.
149. Schwille, P.; Koriach, J.; Webb, W. W., Fluorescence correlation spectroscopy with single-molecule sensitivity on cell and model membranes. *Cytometry* **1999**, *36* (3), 176-82.
150. Foquet, M.; Koriach, J.; Zipfel, W. R.; Webb, W. W.; Craighead, H. G., Focal Volume Confinement by Submicrometer-Sized Fluidic Channels. *Analytical Chemistry* **2004**, *76* (6), 1618-1626.
151. Köhler, R. H.; Cao, J.; Zipfel, W. R.; Webb, W. W.; Hanson, M. R., Exchange of Protein Molecules Through Connections Between Higher Plant Plastids. *Science* **1997**, *276* (5321), 2039.
152. Kohler, R. H.; Schwille, P.; Webb, W. W.; Hanson, M. R., Active protein transport through plastid tubules: velocity quantified by fluorescence correlation spectroscopy. *Journal of Cell Science* **2000**, *113* (22), 3921.
153. Tsang, K.; Cheung, M.; Chan, D.; Cheah, K., The developmental roles of the extracellular matrix: beyond structure to regulation. *Cell and Tissue Research* **2010**, *339* (1), 93-110.
154. Xiaomeng, W.; Robin, E. H.; Laura, J. B.; Hilary, L. A., Type IV collagens regulate BMP signalling in Drosophila. *Nature* **2008**, *455* (7209), 72.
155. Witten, J.; Ribbeck, K., The particle in the spider's web: transport through biological hydrogels. *Nanoscale* **2017**, *9* (24), 8080-8095.
156. Maguire, L.; Betterton, M. D.; Hough, L. E., Bound-State Diffusion due to Binding to Flexible Polymers in a Selective Biofilter. *Biophysical journal* **2019**, *118* (2).
157. Thornton, D. J.; Rousseau, K.; McGuckin, M. A., Structure and Function of the Polymeric Mucins in Airways Mucus. **2008**, *70* (1), 459-486.
158. McGuckin, M. A.; Lindén, S. K.; Sutton, P.; Florin, T. H., Mucin dynamics and enteric pathogens. *Nat Rev Microbiol* **2011**, *9* (4), 265-78.
159. Lai, S. K.; Suk, J. S.; Pace, A.; Wang, Y.-Y.; Yang, M.; Mert, O.; Chen, J.; Kim, J.; Hanes, J., Drug carrier nanoparticles that penetrate human chronic rhinosinusitis mucus. *Biomaterials* **2011**, *32* (26), 6285-6290.
160. Schneider, A. F. L.; Hackenberger, C. P. R., Fluorescent labelling in living cells. *Current Opinion in Biotechnology* **2017**, *48*, 61-68.
161. Huang, X.; Chisholm, J.; Zhuang, J.; Xiao, Y.; Duncan, G.; Chen, X.; Suk, J. S.; Hanes, J., Protein nanocages that penetrate airway mucus and tumor tissue. *Proceedings of the National Academy of Sciences* **2017**, *114* (32), E6595.
162. Mohr, D.; Frey, S.; Fischer, T.; Güttler, T.; Görlich, D., Characterisation of the passive permeability barrier of nuclear pore complexes. *The EMBO Journal* **2009**, *28* (17), 2541-2553.
163. Timney, B. L.; Raveh, B.; Mironska, R.; Trivedi, J. M.; Kim, S. J.; Russel, D.; Wentz, S. R.; Sali, A.; Rout, M. P., Simple rules for passive diffusion through the nuclear pore complex. *Journal of Cell Biology* **2016**, *215* (1), 57-76.
164. Dhaneshwar, S.; Kadam, S.; Kandpal, M.; Gairola, N., Dextran: A promising macromolecular drug carrier.(Review Article). *Indian journal of pharmaceutical sciences* **2006**, *68* (6).
165. Sandolo, C.; Coviello, T.; Matricardi, P.; Alhaique, F., Characterization of polysaccharide hydrogels for modified drug delivery. *European biophysics journal* **2007**, *36* (7), 693-700.
166. Liu, Z.; Jiao, Y.; Wang, Y.; Zhou, C.; Zhang, Z., Polysaccharides-based nanoparticles as drug delivery systems. *Advanced Drug Delivery Reviews* **2008**, *60* (15), 1650-1662.
167. Shi, J.; Zhang, Z.; Qi, W.; Cao, S., Hydrophobically modified biomineralized polysaccharide alginate membrane for sustained smart drug delivery. *International journal of biological macromolecules* **2012**, *50* (3), 747-753.

168. Takakura, Y.; Matsumoto, S.; Hashida, M.; Sezaki, H., Enhanced Lymphatic Delivery of Mitomycin C Conjugated with Dextran. *Cancer research* **1984**, *44* (6), 2505.
169. Huang, G.; Huang, H., Application of dextran as nanoscale drug carriers. *Nanomedicine (London, England)* **2018**, *13* (24), 3149-3158.
170. Hashida, M.; Takakura, Y.; Matsumoto, S.; Sasaki, H.; Kato, A.; Kojima, T.; Muranishi, S.; Sezaki, H., Regeneration characteristics of mitomycin C-dextran conjugate in relation to its activity. *Chemical & pharmaceutical bulletin* **1983**, *31* (6), 2055-63.
171. Huang, S.; Huang, G., Preparation and drug delivery of dextran-drug complex. *Drug delivery* **2019**, *26* (1), 252-261.
172. Schechter, B.; Pazner, R.; Wilchek, M.; Arnon, R., Cis-platinum (II) complexes of carboxymethyl-dextran as potential antitumor agents. II. In vitro and in vivo activity. *Cancer biochemistry biophysics* **1986**, *8* (4), 289-98.
173. Schechter, B.; Rosing, M. A.; Wilchek, M.; Arnon, R., Blood levels and serum protein binding of cis-Platinum(II) complexed to carboxymethyl-dextran. *Cancer Chemotherapy and Pharmacology* **1989**, *24* (3), 161-166.
174. Lai, S. K.; O'Hanlon, D. E.; Harrold, S.; Man, S. T.; Wang, Y.-Y.; Cone, R.; Hanes, J., Rapid transport of large polymeric nanoparticles in fresh undiluted human mucus. *Proceedings of the National Academy of Sciences of the United States of America* **2007**, *104* (5), 1482-1487.
175. Cu, Y.; Saltzman, W. M., Mathematical modeling of molecular diffusion through mucus. *Advanced Drug Delivery Reviews* **2009**, *61* (2), 101-114.
176. Kekenus-Huskey, P. M.; Gillette, A. K.; McCammon, J. A., Predicting the influence of long-range molecular interactions on macroscopic-scale diffusion by homogenization of the Smoluchowski equation. *The Journal of Chemical Physics* **2014**, *140* (17), 174106.
177. Arends, F.; Baumgärtel, R.; Lieleg, O., Ion-Specific Effects Modulate the Diffusive Mobility of Colloids in an Extracellular Matrix Gel. *Langmuir* **2013**, *29* (51), 15965-15973.
178. Mangelot, S.; Keller, S.; Rädler, J., Transport of nucleosome core particles in semidilute DNA solutions. *Biophys J* **2003**, *85* (3), 1817-25.
179. Rusu, L.; Lumma, D.; Rädler, J. O., Charge and Size Dependence of Liposome Diffusion in Semidilute Biopolymer Solutions. *Macromolecular bioscience* **2010**, *10* (12), 1465-1472.
180. Cu, Y.; Saltzman, W. M., Drug delivery: Stealth particles give mucus the slip. *Nat Mater* **2009**, *8* (1), 11-13.
181. Odijk, T., Depletion Theory of Protein Transport in Semi-Dilute Polymer Solutions. *Biophysical Journal* **2000**, *79* (5), 2314-2321.
182. Sellers, L. A.; Allen, A.; Morris, E. R.; Ross-Murphy, S. B., Mechanical characterization and properties of gastrointestinal mucus gel. *Biorheology* **1987**, *24* (6), 615-23.
183. Matsui, H.; Wagner, V. E.; Hill, D. B.; Schwab, U. E.; Rogers, T. D.; Button, B.; Taylor, R. M., 2nd; Superfine, R.; Rubinstein, M.; Iglewski, B. H.; Boucher, R. C., A physical linkage between cystic fibrosis airway surface dehydration and Pseudomonas aeruginosa biofilms. *Proc Natl Acad Sci U S A* **2006**, *103* (48), 18131-6.
184. Strous, G. J.; Dekker, J., Mucin-type glycoproteins. *Critical reviews in biochemistry and molecular biology* **1992**, *27* (1-2), 57-92.
185. Wolf, D. P.; Sokoloski, J.; Khan, M. A.; Litt, M., Human cervical mucus. III. Isolation and characterization of rheologically active mucin. *Fertility and sterility* **1977**, *28* (1), 53-8.
186. Kohli, I.; Mukhopadhyay, A., Diffusion of Nanoparticles in Semidilute Polymer Solutions: Effect of Different Length Scales. *Macromolecules* **2012**, *45* (15), 6143-6149.
187. Zhang, X.; Hansing, J.; Netz, Roland r.; Derouchey, Jason e., Particle Transport through Hydrogels Is Charge Asymmetric. *Biophysical Journal* **2015**, *108* (3), 530-539.

188. Sauter, A.; Richter, G.; Micoulet, A.; Martinez, A.; Spatz, J. P.; Appel, S., Effective polyethylene glycol passivation for the inhibition of surface interactions of peripheral blood mononuclear cells and platelets. *Biointerphases* **2013**, *8* (1), 1-12.
189. Ries, J.; Schwille, P., Fluorescence correlation spectroscopy. *BioEssays* **2012**, *34* (5), 361-368.
190. Widengren, J., Fluorescence Flicker as a Read-out in FCS: Principles, Applications and Further Developments. Berlin, Heidelberg: Springer Berlin Heidelberg: Berlin, Heidelberg, 2009; pp 155-172.
191. Gendron, P. O.; Avaltroni, F.; Wilkinson, K. J., Diffusion Coefficients of Several Rhodamine Derivatives as Determined by Pulsed Field Gradient–Nuclear Magnetic Resonance and Fluorescence Correlation Spectroscopy. *Journal of fluorescence* **2008**, *18* (6), 1093-1101.
192. Doi, M.; Edwards, S. F., *The theory of polymer dynamics*. Clarendon Press: Oxford [Oxfordshire, 1986.
193. Chatterjee, A. P.; Schweizer, K. S., Liquid-State Theory of Semidilute and Concentrated Polymer Solutions. *Macromolecules* **1998**, *31* (7), 2353-2367.
194. Rubinstein, M.; Colby, R. H., *Polymer physics / Michael Rubinstein and Ralph H. Colby*. Oxford University Press: Oxford ;, 2007.
195. Gordon, M., Scaling concepts in polymer physics: Pierre-Gilles de Gennes Cornell University Press, Ithaca and London, 1980. Elsevier Ltd: 1981; Vol. 22, pp 565-565.
196. Wei, M.-T.; Elbaum-Garfinkle, S.; Holehouse, A. S.; Chen, C. C.-H.; Feric, M.; Arnold, C. B.; Priestley, R. D.; Pappu, R. V.; Brangwynne, C. P., Phase behaviour of disordered proteins underlying low density and high permeability of liquid organelles. *Nature chemistry* **2017**, *9* (11), 1118-1125.
197. Pelton, R., Polyvinylamine: A Tool for Engineering Interfaces. *Langmuir* **2014**, *30* (51), 15373-15382.
198. Kim, T. J.; Li, B.; Hägg, M. B., Novel fixed-site–carrier polyvinylamine membrane for carbon dioxide capture. *Journal of polymer science. Part B, Polymer physics* **2004**, *42* (23), 4326-4336.
199. Suekama, T. C.; Aziz, V.; Mohammadi, Z.; Berkland, C.; Gehrke, S. H., Synthesis and characterization of poly(N-vinyl formamide) hydrogels—A potential alternative to polyacrylamide hydrogels. *Journal of Polymer Science Part A: Polymer Chemistry* **2013**, *51* (2), 435-445.
200. Nordmeier, E., Static and dynamic light-scattering solution behavior of pullulan and dextran in comparison. *Journal of physical chemistry (1952)* **1993**, *97* (21), 5770-5785.
201. The science of polymer molecules. *Materials characterization* **1997**, *38* (1), 51.
202. Scott, D.; Coleman, P. J.; Mason, R. M.; Levick, J. R., Action of polysaccharides of similar average mass but differing molecular volume and charge on fluid drainage through synovial interstitium in rabbit knees. *The Journal of physiology* **2000**, *528* (3), 609-618.
203. Granath, K. A., Solution properties of branched dextrans. *Journal of colloid science* **1958**, *13* (4), 308-328.
204. Senti, F. R.; Hellman, N. N.; Ludwig, N. H.; Babcock, G. E.; Tobin, R.; Glass, C. A.; Lamberts, B. L., Viscosity, sedimentation, and light-scattering properties of fraction of an acid-hydrolyzed dextran. *Journal of polymer science* **1955**, *17* (86), 527-546.
205. Gennes, P.-G. d., *Scaling concepts in polymer physics*. Ithaca, N.Y. : Cornell University Press: Ithaca, N.Y., 1979.
206. Holyst, R.; Bielejewska, A.; Ziebacz, N.; Wieczorek, S. A.; Szymanski, J.; Wilk, A.; Patkowski, A.; Gapinski, J.; Zywockinski, A.; Kalwarczyk, T.; Kalwarczyk, E.; Tabaka, M., Scaling form of viscosity at all length-scales in poly(ethylene glycol) solutions studied by fluorescence

- correlation spectroscopy and capillary electrophoresis. *Physical chemistry chemical physics : PCCP* **2009**, *11* (40), 9025-9032.
207. Chu, Kengyeh K.; Mojahed, D.; Fernandez, Courtney M.; Li, Y.; Liu, L.; Wilsterman, Eric J.; Diephuis, B.; Birket, Susan E.; Bowers, H.; Martin Solomon, G.; Schuster, Benjamin S.; Hanes, J.; Rowe, Steven M.; Tearney, Guillermo J., Particle-Tracking Microrheology Using Micro-Optical Coherence Tomography. *Biophysical journal* **2016**, *111* (5), 1053-1063.
208. Goins, A. B.; Sanabria, H.; Waxham, M. N., Macromolecular Crowding and Size Effects on Probe Microviscosity. *Biophysical journal* **2008**, *95* (11), 5362-5373.
209. Pacheco-Alvarez, D.; Solórzano-Vargas, R. S.; Del Río, A. L., Biotin in metabolism and its relationship to human disease. *Archives of medical research* **2002**, *33* (5), 439-47.
210. DeChancie, J.; Houk, K. N., The Origins of Femtomolar Protein–Ligand Binding: Hydrogen-Bond Cooperativity and Desolvation Energetics in the Biotin–(Strept)Avidin Binding Site. *Journal of the American Chemical Society* **2007**, *129* (17), 5419-5429.
211. Chivers, C. E.; Koner, A. L.; Lowe, E. D.; Howarth, M., How the biotin-streptavidin interaction was made even stronger: investigation via crystallography and a chimaeric tetramer. *Biochem J* **2011**, *435* (1), 55-63.
212. Girod, S.; Zahm, J. M.; Plotkowski, C.; Beck, G.; Puchelle, E., Role of the physiochemical properties of mucus in the protection of the respiratory epithelium. *The European respiratory journal* **1992**, *5* (4), 477-87.
213. Lai, S. K.; Wang, Y. Y.; Wirtz, D.; Hanes, J., Micro- and macrorheology of mucus. *Adv Drug Deliv Rev* **2009**, *61* (2), 86-100.
214. Crockett, R., Boundary Lubrication in Natural Articular Joints. *Tribology Letters* **2009**, *35* (2), 77-84.
215. Zhao, W.; Jin, X.; Cong, Y.; Liu, Y.; Fu, J., Degradable natural polymer hydrogels for articular cartilage tissue engineering. *Journal of chemical technology and biotechnology (1986)* **2013**, *88* (3), 327-339.
216. Fletcher, D. A.; Mullins, R. D., Cell mechanics and the cytoskeleton. *Nature* **2010**, *463* (7280), 485-492.
217. Fomovsky, G. M.; Thomopoulos, S.; Holmes, J. W., Contribution of extracellular matrix to the mechanical properties of the heart. *Journal of molecular and cellular cardiology* **2010**, *48* (3), 490-6.
218. Yang, Y. J.; Mai, D. J.; Dursch, T. J.; Olsen, B. D., Nucleopore-Inspired Polymer Hydrogels for Selective Biomolecular Transport. *Biomacromolecules* **2018**, *19* (10), 3905-3916.
219. Yu, M.; Xu, L.; Tian, F.; Su, Q.; Zheng, N.; Yang, Y.; Wang, J.; Wang, A.; Zhu, C.; Guo, S.; Zhang, X.; Gan, Y.; Shi, X.; Gao, H., Rapid transport of deformation-tuned nanoparticles across biological hydrogels and cellular barriers. *Nature communications* **2018**, *9* (1), 2607-2607.
220. Huckaby, J. T.; Lai, S. K., PEGylation for enhancing nanoparticle diffusion in mucus. *Advanced Drug Delivery Reviews* **2018**, *124*, 125-139.
221. Shan, W.; Zhu, X.; Liu, M.; Li, L.; Zhong, J.; Sun, W.; Zhang, Z.; Huang, Y., Overcoming the diffusion barrier of mucus and absorption barrier of epithelium by self-assembled nanoparticles for oral delivery of insulin. *ACS Nano* **2015**, *9* (3), 2345-56.
222. Liu, M.; Zhang, J.; Zhu, X.; Shan, W.; Li, L.; Zhong, J.; Zhang, Z.; Huang, Y., Efficient mucus permeation and tight junction opening by dissociable "mucus-inert" agent coated trimethyl chitosan nanoparticles for oral insulin delivery. *Journal of controlled release : official journal of the Controlled Release Society* **2016**, *222*, 67-77.
223. Lieleg, O.; Ribbeck, K., Biological hydrogels as selective diffusion barriers. *Trends Cell Biol* **2011**, *21* (9), 543-51.

224. Mouw, J. K.; Ou, G.; Weaver, V. M., Extracellular matrix assembly: a multiscale deconstruction. *Nature reviews. Molecular cell biology* **2014**, *15* (12), 771-785.
225. Knudson, C. B.; Knudson, W., Cartilage proteoglycans. *Seminars in Cell & Developmental Biology* **2001**, *12* (2), 69-78.
226. Schittny, J. C.; Yurchenco, P. D., Basement membranes: molecular organization and function in development and disease. *Current opinion in cell biology* **1989**, *1* (5), 983-988.
227. Rosso, F.; Giordano, A.; Barbarisi, M.; Barbarisi, A., From Cell-ECM interactions to tissue engineering. *Journal of cellular physiology* **2004**, *199* (2), 174-180.
228. Frantz, C.; Stewart, K. M.; Weaver, V. M., The extracellular matrix at a glance. *J Cell Sci* **2010**, *123* (Pt 24), 4195-200.
229. Valiente-Alandi, I.; Schafer, A. E.; Blaxall, B. C., Extracellular matrix-mediated cellular communication in the heart. *Journal of molecular and cellular cardiology* **2016**, *91*, 228-237.
230. Taipale, J.; Keski-Oja, J., Growth factors in the extracellular matrix. *The FASEB journal* **1997**, *11* (1), 51-59.
231. Bayston, L. J.; Wang, X.; Harris, R. E.; Ashe, H. L., Type IV collagens regulate BMP signalling in Drosophila. *Nature (London)* **2008**, *455* (7209), 72-77.
232. Sophia Fox, A. J.; Bedi, A.; Rodeo, S. A., The basic science of articular cartilage: structure, composition, and function. *Sports Health* **2009**, *1* (6), 461-468.
233. Amemiya, S., Nanoelectrochemical Study of Molecular Transport through the Nuclear Pore Complex. *Chemical record (New York, N.Y.)* **2021**.
234. Chen, W. G.; Witten, J.; Grindy, S. C.; Holten-Andersen, N.; Ribbeck, K., Charge Influences Substrate Recognition and Self-Assembly of Hydrophobic FG Sequences. *Biophysical journal* **2017**, *113* (9), 2088-2099.
235. Tagliazucchi, M.; Peleg, O.; Kröger, M.; Rabin, Y.; Szleifer, I., Effect of charge, hydrophobicity, and sequence of nucleoporins on the translocation of model particles through the nuclear pore complex. *Proceedings of the National Academy of Sciences of the United States of America* **2013**, *110* (9), 3363-3368.
236. Laffleur, F.; Hintzen, F.; Shahnaz, G.; Rahmat, D.; Leithner, K.; Bernkop-Schnürch, A., Development and in vitro evaluation of slippery nanoparticles for enhanced diffusion through native mucus. *Nanomedicine* **2013**, *9* (3), 387-396.
237. Wang, Y.-Y.; Lai, S. K.; Suk, J. S.; Pace, A.; Cone, R.; Hanes, J., Addressing the PEG Mucoadhesivity Paradox to Engineer Nanoparticles that "Slip" through the Human Mucus Barrier. *Angewandte Chemie International Edition* **2008**, *47* (50), 9726-9729.
238. Käsdorf, Benjamin T.; Arends, F.; Lieleg, O., Diffusion Regulation in the Vitreous Humor. *Biophysical journal* **2015**, *109* (10), 2171-2181.
239. Robert, G. T.; Aparna, L.; Enrique, R.-B.; Charles, N., In vivo Diffusion of Lactoferrin in Brain Extracellular Space Is Regulated by Interactions with Heparan Sulfate. *Proceedings of the National Academy of Sciences - PNAS* **2008**, *105* (24), 8416-8421.
240. Hansing, J.; Ciemer, C.; Kim, W. K.; Zhang, X.; DeRouchey, J. E.; Netz, R. R., Nanoparticle filtering in charged hydrogels: Effects of particle size, charge asymmetry and salt concentration. *The European physical journal. E, Soft matter and biological physics* **2016**, *39* (5), 1-13.
241. Xu, Q.; Boylan, N. J.; Suk, J. S.; Wang, Y.-Y.; Nance, E. A.; Yang, J.-C.; McDonnell, P. J.; Cone, R. A.; Duh, E. J.; Hanes, J., Nanoparticle diffusion in, and microrheology of, the bovine vitreous ex vivo. *Journal of Controlled Release* **2013**, *167* (1), 76-84.
242. Arends, F.; Baumgärtel, R.; Lieleg, O., Ion-Specific Effects Modulate the Diffusive Mobility of Colloids in an Extracellular Matrix Gel. *Langmuir* **2013**, *29* (51), 15965-15973.

243. Stylianopoulos, T.; Poh, M.-Z.; Insin, N.; Bawendi, M. G.; Fukumura, D.; Munn, Lance I.; Jain, R. K., Diffusion of Particles in the Extracellular Matrix: The Effect of Repulsive Electrostatic Interactions. *Biophysical Journal* **2010**, *99* (5), 1342-1349.
244. Shattock, R. J.; Moore, J. P., Inhibiting sexual transmission of HIV-1 infection. *Nature Reviews Microbiology* **2003**, *1* (1), 25-34.
245. Miller, C. J.; Shattock, R. J., Target cells in vaginal HIV transmission. *Microbes and Infection* **2003**, *5* (1), 59-67.
246. Bouvet, J.-P.; Grésenguet, G.; Bélec, L., Vaginal pH neutralization by semen as a cofactor of HIV transmission. *Clinical Microbiology and Infection* **1997**, *3* (1), 19-23.
247. Mitchison, T.; Kirschner, M., Cytoskeletal dynamics and nerve growth. *Neuron (Cambridge, Mass.)* **1988**, *1* (9), 761-772.
248. Murray, D. W.; Arthur, H. L.; Shu-Ying, H.; Marc, W. K., A Protein Factor Essential for Microtubule Assembly. *Proceedings of the National Academy of Sciences - PNAS* **1975**, *72* (5), 1858-1862.
249. Karen, A. B.; Marc, W. K., Tau Protein Binds to Microtubules through a Flexible Array of Distributed Weak Sites. *The Journal of cell biology* **1991**, *115* (3), 717-730.
250. Trojanowski, J. Q.; Schuck, T.; Schmidt, M. L.; Lee, V. M., Distribution of tau proteins in the normal human central and peripheral nervous system. *The journal of histochemistry and cytochemistry* **1989**, *37* (2), 209-215.
251. Barbier, P.; Zejneli, O.; Martinho, M.; Lasorsa, A.; Belle, V.; Smet-Nocca, C.; Tsvetkov, P. O.; Devred, F.; Landrieu, I., Role of Tau as a Microtubule-Associated Protein: Structural and Functional Aspects. *Frontiers in aging neuroscience* **2019**, *11*.
252. Jung, D.; Filliol, D.; Mieke, M.; Rendon, A., Interaction of brain mitochondria with microtubules reconstituted from brain tubulin and MAP2 or TAU. *Cell motility and the cytoskeleton* **1993**, *24* (4), 245-55.
253. Mietelska-Porowska, A.; Wasik, U.; Goras, M.; Filipek, A.; Niewiadomska, G., Tau protein modifications and interactions: their role in function and dysfunction. *Int J Mol Sci* **2014**, *15* (3), 4671-4713.
254. Brandt, R.; Léger, J.; Lee, G., Interaction of tau with the neural plasma membrane mediated by tau's amino-terminal projection domain. *J Cell Biol* **1995**, *131* (5), 1327-40.
255. Jesús, A.; José J, L.; Mar, P.; Félix, H., Role of Tau Protein in Both Physiological and Pathological Conditions. *Physiological Reviews* **2004**, *84* (2), 361-384.
256. Wang, X.; Chang, C.; Wang, D.; Hong, S., Systematic profiling of SH3-mediated Tau-Partner interaction network in Alzheimer's disease by integrating in silico analysis and in vitro assay. *Journal of molecular graphics & modelling* **2019**, *90*, 265-272.
257. David, G. D.; Marc, W. K., Tau Protein Function in Living Cells. *The Journal of cell biology* **1986**, *103* (6), 2739-2746.
258. Avila, J.; Jiménez, J. S.; Sayas, C. L.; Bolós, M.; Zabala, J. C.; Rivas, G.; Hernández, F., Tau Structures. *Frontiers in aging neuroscience* **2016**, *8*, 262-262.
259. Andreadis, A., Tau splicing and the intricacies of dementia. *Journal of cellular physiology* **2012**, *227* (3), 1220-1225.
260. Goedert, M.; Spillantini, M. G.; Jakes, R.; Rutherford, D.; Crowther, R. A., Multiple isoforms of human microtubule-associated protein tau: sequences and localization in neurofibrillary tangles of Alzheimer's disease. *Neuron (Cambridge, Mass.)* **1989**, *3* (4), 519-526.
261. Sibille, N.; Huvent, I.; Fauquant, C.; Verdegem, D.; Amniai, L.; Leroy, A.; Wieruszeski, J. M.; Lippens, G.; Landrieu, I., Structural characterization by nuclear magnetic resonance of the impact of phosphorylation in the proline-rich region of the disordered Tau protein. *Proteins, structure, function, and bioinformatics* **2012**, *80* (2), 454-462.

262. Mukrasch, M. D.; Bibow, S.; Korukottu, J.; Jeganathan, S.; Biernat, J.; Griesinger, C.; Mandelkow, E.; Zweckstetter, M., Structural polymorphism of 441-residue Tau at single residue resolution. *PLoS biology* **2009**, *7* (2), 0399-0414.
263. Guo, T.; Noble, W.; Hanger, D. P., Roles of tau protein in health and disease. *Acta neuropathologica* **2017**, *133* (5), 665-704.
264. Clément, D.; Cillian, B.; Haoling, Q.; François-Xavier, C.; Isabelle, H.; Béatrice, C.; Etienne-Emile, B.; Yves, J.; Isabelle, L.; Guy, L.; Caroline, S.-N., Identification of the Tau phosphorylation pattern that drives its aggregation. *Proceedings of the National Academy of Sciences - PNAS* **2017**, *114* (34), 9080-9085.
265. Goedert, M.; Cohen, E. S.; Jakes, R.; Cohen, P., p42 map kinase phosphorylation sites in microtubule-associated protein tau are dephosphorylated by protein phosphatase 2A1 Implications for Alzheimer's disease. *FEBS letters* **1992**, *312* (1), 95-99.
266. Gordon-Krajcer, W.; Yang, L. S.; Ksiezak-Reding, H., Conformation of paired helical filaments blocks dephosphorylation of epitopes shared with fetal tau except Ser199/202 and Ser202/Thr205. *Brain research* **2000**, *856* (1), 163-175.
267. Correas, I.; DÃ-az-Nido, J.; Avila, J., Microtubule-associated protein tau is phosphorylated by protein kinase C on its tubulin binding domain. *The Journal of biological chemistry* **1992**, *267* (22), 15721-15728.
268. Drewes, G.; Lichtenberg-Kraag, B.; Döring, F.; Mandelkow, E. M.; Biernat, J.; Goris, J.; Dorée, M.; Mandelkow, E., Mitogen activated protein (MAP) kinase transforms tau protein into an Alzheimer-like state. *The EMBO journal* **1992**, *11* (6), 2131-2138.
269. Goedert, M.; Hasegawa, M.; Jakes, R.; Lawler, S.; Cuenda, A.; Cohen, P., Phosphorylation of microtubule-associated protein tau by stress-activated protein kinases. *FEBS letters* **1997**, *409* (1), 57-62.
270. Weingarten, M. D.; Lockwood, A. H.; Hwo, S. Y.; Kirschner, M. W., A protein factor essential for microtubule assembly. *Proceedings of the National Academy of Sciences* **1975**, *72* (5), 1858.
271. Bré, M. H.; Karsenti, E., Effects of brain microtubule-associated proteins on microtubule dynamics and the nucleating activity of centrosomes. **1990**, *15* (2), 88-98.
272. Drechsel, D. N.; Hyman, A. A.; Cobb, M. H.; Kirschner, M. W., Modulation of the dynamic instability of tubulin assembly by the microtubule-associated protein tau. *Molecular Biology of the Cell* **1992**, *3* (10), 1141-1154.
273. Drubin, D. G.; Kirschner, M. W., Tau protein function in living cells. *Journal of Cell Biology* **1986**, *103* (6), 2739-2746.
274. Gustke, N.; Trinczek, B.; Biernat, J.; Mandelkow, E. M.; Mandelkow, E., Domains of tau Protein and Interactions with Microtubules. *Biochemistry* **1994**, *33* (32), 9511-9522.
275. Butner, K. A.; Kirschner, M. W., Tau protein binds to microtubules through a flexible array of distributed weak sites. *Journal of Cell Biology* **1991**, *115* (3), 717-730.
276. Friedman, J. R.; Nunnari, J., Mitochondrial form and function. *Nature (London)* **2014**, *505* (7483), 335-343.
277. Pryor, P. R.; Luzio, J. P.; Bright, N. A., Lysosomes: fusion and function. *Nature reviews. Molecular cell biology* **2007**, *8* (8), 622-632.
278. Salminen, A.; Kauppinen, A.; Suuronen, T.; Kaarniranta, K.; Ojala, J., ER stress in Alzheimer's disease: a novel neuronal trigger for inflammation and Alzheimer's pathology. *Journal of neuroinflammation* **2009**, *6* (1), 41-41.
279. Joel, B.; Stephanie, C. W.; Nilesh, V.; Mikko, H.; Clifford, P. B., RNA transcription modulates phase transition-driven nuclear body assembly. *Proceedings of the National Academy of Sciences - PNAS* **2015**, *112* (38), E5237-E5245.

280. Lin, Y.; Protter, David S. W.; Rosen, Michael K.; Parker, R., Formation and Maturation of Phase-Separated Liquid Droplets by RNA-Binding Proteins. *Molecular cell* **2015**, *60* (2), 208-219.
281. Wegmann, S.; Eftekhazadeh, B.; Tepper, K.; Zoltowska, K. M.; Bennett, R. E.; Dujardin, S.; Laskowski, P. R.; MacKenzie, D.; Kamath, T.; Commins, C.; Vanderburg, C.; Roe, A. D.; Fan, Z.; Mollieux, A. M.; Hernandez-Vega, A.; Muller, D.; Hyman, A. A.; Mandelkow, E.; Taylor, J. P.; Hyman, B. T., Tau protein liquid–liquid phase separation can initiate tau aggregation. *The EMBO Journal* **2018**, *37* (7).
282. Protter, D. S. W.; Parker, R., Principles and Properties of Stress Granules. *Trends in cell biology* **2016**, *26* (9), 668-679.
283. Németh, A.; Längst, G., Genome organization in and around the nucleolus. *Trends in genetics* **2011**, *27* (4), 149-156.
284. Iarovaia, O. V.; Minina, E. P.; Sheval, E. V.; Onichtchouk, D.; Dokudovskaya, S.; Razin, S. V.; Vassetzky, Y. S., Nucleolus: A Central Hub for Nuclear Functions. *Trends in cell biology* **2019**, *29* (8), 647-659.
285. Banani, S. F.; Lee, H. O.; Hyman, A. A.; Rosen, M. K., Biomolecular condensates: organizers of cellular biochemistry. *Nature reviews. Molecular cell biology* **2017**, *18* (5), 285-298.
286. Aumiller, J. W. M.; Keating, C. D., Phosphorylation-mediated RNA/peptide complex coacervation as a model for intracellular liquid organelles. *Nature chemistry* **2016**, *8* (2), 129-137.
287. Ferreon, J. C.; Jain, A.; Choi, K.-J.; Tsoi, P. S.; MacKenzie, K. R.; Jung, S. Y.; Ferreon, A. C., Acetylation Disfavors Tau Phase Separation. *Int J Mol Sci* **2018**, *19* (5), 1360.
288. Rai, S. K.; Savastano, A.; Singh, P.; Mukhopadhyay, S.; Zweckstetter, M., Liquid-liquid phase separation of tau: From molecular biophysics to physiology and disease. *Protein science : a publication of the Protein Society* **2021**, *30* (7), 1294-1314.
289. de Kruif, C. G.; Weinbreck, F.; de Vries, R., Complex coacervation of proteins and anionic polysaccharides. *Current Opinion in Colloid & Interface Science* **2004**, *9* (5), 340-349.
290. Gabryelczyk, B.; Cai, H.; Shi, X.; Sun, Y.; Swinkels, P. J. M.; Salentinig, S.; Pervushin, K.; Miserez, A., Hydrogen bond guidance and aromatic stacking drive liquid-liquid phase separation of intrinsically disordered histidine-rich peptides. *Nature communications* **2019**, *10* (1), 5465-5465.
291. Sing, C. E.; Perry, S. L., Recent progress in the science of complex coacervation. *Soft Matter* **2020**, *16* (12), 2885-2914.
292. Danielsen, S. P. O.; McCarty, J.; Shea, J.-E.; Delaney, K. T.; Fredrickson, G. H., Molecular design of self-coacervation phenomena in block polyampholytes. *Proceedings of the National Academy of Sciences - PNAS* **2019**, *116* (17), 8224-8232.
293. Holehouse, A. S.; Das, R. K.; Ahad, J. N.; Richardson, M. O.; Pappu, R. V., CIDER: Resources to Analyze Sequence-Ensemble Relationships of Intrinsically Disordered Proteins. *Biophys J* **2017**, *112* (1), 16-21.
294. Boyko, S.; Qi, X.; Chen, T.-H.; Surewicz, K.; Surewicz, W. K., Liquid-liquid phase separation of tau protein: The crucial role of electrostatic interactions. *The Journal of biological chemistry* **2019**, *294* (29), 11054-11059.
295. Kanaan, N. M.; Hamel, C.; Grabinski, T.; Combs, B., Liquid-liquid phase separation induces pathogenic tau conformations in vitro. *Nature Communications* **2020**, *11* (1), 2809.
296. Ambadipudi, S.; Biernat, J.; Riedel, D.; Mandelkow, E.; Zweckstetter, M., Liquid–liquid phase separation of the microtubule-binding repeats of the Alzheimer-related protein Tau. *Nature Communications* **2017**, *8* (1), 275.
297. Boyko, S.; Surewicz, K.; Surewicz, W. K., Regulatory mechanisms of tau protein fibrillation under the conditions of liquid–liquid phase separation. *Proceedings of the National Academy of Sciences* **2020**, *117* (50), 31882.

298. Lin, Y.; McCarty, J.; Rauch, J. N.; Delaney, K. T.; Kosik, K. S.; Fredrickson, G. H.; Shea, J.-E.; Han, S., Narrow equilibrium window for complex coacervation of tau and RNA under cellular conditions. *eLife* **2019**, *8*.
299. Zhang, X.; Lin, Y.; Eschmann, N. A.; Zhou, H.; Rauch, J. N.; Hernandez, I.; Guzman, E.; Kosik, K. S.; Han, S., RNA stores tau reversibly in complex coacervates. *PLoS biology* **2017**, *15* (7), e2002183-e2002183.
300. Alonso, A.; Zaidi, T.; Novak, M.; Grundke-Iqbal, I.; Iqbal, K., Hyperphosphorylation induces self-assembly of tau into tangles of paired helical filaments/straight filaments. *Proceedings of the National Academy of Sciences - PNAS* **2001**, *98* (12), 6923-6928.
301. Iqbal, K.; Alonso, A. d. C.; Grundke-Iqbal, I., Alzheimer's disease hyperphosphorylated tau sequesters normal tau into tangles of filaments and disassembles microtubules. *Nature medicine* **1996**, *2* (7), 783-787.
302. Lu, M.; Kosik, K. S., Competition for microtubule-binding with dual expression of tau missense and splice isoforms. *Molecular biology of the cell* **2001**, *12* (1), 171-184.
303. Kampers, T.; Friedhoff, P.; Biernat, J.; Mandelkow, E. M.; Mandelkow, E., RNA stimulates aggregation of microtubule-associated protein tau into Alzheimer-like paired helical filaments. *FEBS letters* **1996**, *399* (3), 344-349.
304. Crowther, R. A.; Smith, M. J.; Hasegawa, M.; Goedert, M.; Jakes, R.; Spillantini, M. G., Assembly of microtubule-associated protein tau into Alzheimer-like filaments induced by sulphated glycosaminoglycans. *Nature (London)* **1996**, *383* (6600), 550-553.
305. Vanderweyde, T.; Apicco, D. J.; Youmans-Kidder, K.; Ash, P. E. A.; Cook, C.; Lummertz da Rocha, E.; Jansen-West, K.; Frame, A. A.; Citro, A.; Leszyk, J. D.; Ivanov, P.; Abisambra, J. F.; Steffen, M.; Li, H.; Petrucelli, L.; Wolozin, B., Interaction of tau with the RNA-Binding Protein TIA1 Regulates tau Pathophysiology and Toxicity. *Cell reports* **2016**, *15* (7), 1455-1466.
306. von Bergen, M.; Barghorn, S.; Biernat, J.; Mandelkow, E. M.; Mandelkow, E., Tau aggregation is driven by a transition from random coil to beta sheet structure. *Biochimica et biophysica acta* **2005**, *1739* (2-3), 158-66.
307. Walker, L. C.; Diamond, M. I.; Duff, K. E.; Hyman, B. T., Mechanisms of protein seeding in neurodegenerative diseases. *JAMA neurology* **2013**, *70* (3), 304-10.
308. Fisher, R. S.; Elbaum-Garfinkle, S., Tunable multiphase dynamics of arginine and lysine liquid condensates. *Nature communications* **2020**, *11* (1), 4628-4628.
309. Holehouse, A. S.; Pappu, R. V., Functional Implications of Intracellular Phase Transitions. *Biochemistry (Easton)* **2018**, *57* (17), 2415-2423.
310. Sherman, E.; Itkin, A.; Kuttner, Y. Y.; Rhoades, E.; Amir, D.; Haas, E.; Haran, G., Using fluorescence correlation spectroscopy to study conformational changes in denatured proteins. *Biophys J* **2008**, *94* (12), 4819-27.
311. Banjade, S.; Rosen, M. K., Phase transitions of multivalent proteins can promote clustering of membrane receptors. *eLife* **2014**, *3*.
312. Jiang, H.; Wang, S.; Huang, Y.; He, X.; Cui, H.; Zhu, X.; Zheng, Y., Phase Transition of Spindle-Associated Protein Regulate Spindle Apparatus Assembly. *Cell (Cambridge)* **2015**, *163* (1), 108-122.
313. Pilong, L. I.; Banjade, S.; Russo, P. S.; Jiang, Q.-X.; Tracy Nixon, B.; Rosen, M. K.; Cheng, H.-C.; Kim, S.; Baoyu, C.; Liang, G. U. O.; Llaguno, M.; Hollingsworth, J. V.; King, D.; Banani, S., Phase transitions in the assembly of multivalent signalling proteins. *Nature (London)* **2012**, *483* (7389), 336-340.
314. Su, X.; Ditlev, J. A.; Hui, E.; Xing, W.; Banjade, S.; Okrut, J.; King, D. S.; Taunton, J.; Rosen, M. K.; Vale, R. D., Phase separation of signaling molecules promotes T cell receptor signal

- transduction. *Science (American Association for the Advancement of Science)* **2016**, 352 (6285), 595-599.
315. Jeannot, V.; Salmon, J.-M.; Deumie, M.; Viallet, P., Intracellular Accumulation of Rhodamine 110 in Single Living Cells. *The journal of histochemistry and cytochemistry* **1997**, 45 (3), 403-412.
316. Hosseini, H.; Rangchian, A.; Prins, M. L.; Giza, C. C.; Ruberti, J. W.; Kavehpour, H. P., Probing Flow-Induced Biomolecular Interactions With Micro-Extensional Rheology: Tau Protein Aggregation. *Journal of biomechanical engineering* **2020**, 142 (3).
317. Jho, Y. S.; Zhulina, E. B.; Kim, M. W.; Pincus, P. A., Monte Carlo Simulations of Tau Proteins: Effect of Phosphorylation. *Biophysical journal* **2010**, 99 (8), 2387-2397.
318. Ming-Tzo, W.; Shana, E.-G.; Alex, S. H.; Carlos Chih-Hsiung, C.; Marina, F.; Craig, B. A.; Rodney, D. P.; Rohit, V. P.; Clifford, P. B., Phase behaviour of disordered proteins underlying low density and high permeability of liquid organelles. *Nature Chemistry* **2017**, 9 (11).
319. De Gennes, P. G., Dynamics of Entangled Polymer Solutions. I. The Rouse Model. *Macromolecules* **1976**, 9 (4), 587-593.
320. Singh-Zocchi, M.; Andreasen, A.; Zocchi, G., Osmotic pressure contribution of albumin to colloidal interactions. *Proceedings of the National Academy of Sciences of the United States of America* **1999**, 96 (12), 6711-6715.
321. Bernardi, M.; Ricci, C. S.; Zaccherini, G., Role of Human Albumin in the Management of Complications of Liver Cirrhosis. *Journal of clinical and experimental hepatology* **2014**, 4 (4), 302-311.
322. Barbosa, L. R. S.; Ortore, M. G.; Spinozzi, F.; Mariani, P.; Bernstorff, S.; Itri, R., The Importance of Protein-Protein Interactions on the pH-Induced Conformational Changes of Bovine Serum Albumin: A Small-Angle X-Ray Scattering Study. *Biophysical journal* **2010**, 98 (1), 147-157.
323. Falke, S.; Dierks, K.; Blanchet, C.; Graewert, M.; Cipriani, F.; Meijers, R.; Svergun, D.; Betzel, C., Multi-channel in situ dynamic light scattering instrumentation enhancing biological small-angle X-ray scattering experiments at the PETRA III beamline P12. *Journal of synchrotron radiation* **2018**, 25 (2), 361-372.
324. Jo, Y.; Jung, Y., Interplay between intrinsically disordered proteins inside membraneless protein liquid droplets Electronic supplementary information (ESI) available. See DOI: 10.1039/c9sc03191j. *Chemical science (Cambridge)* **2020**, 11 (5), 1269-1275.
325. Gaigalas, A. K.; Hubbard, J. B.; McCurley, M.; Woo, S., Diffusion of bovine serum albumin in aqueous solutions. *The Journal of Physical Chemistry* **1992**, 96 (5), 2355-2359.
326. Aumiller, W. M.; Keating, C. D., Phosphorylation-mediated RNA/peptide complex coacervation as a model for intracellular liquid organelles. *Nature Chemistry* **2016**, 8 (2), 129-137.

Vita

Kanthi Nuti

Personal Information

Place of Birth: India

Education

09/2009 – 07/2012 **Osmania University**

Hyderabad, India, Bachelor of Science

09/2012 – 06/2014 **Osmania University**

Hyderabad, India, Master of Science (Organic Chemistry)

Awards and Scholarships

- 10/2020 Third place in UK Grad Research Live competition
- 05/2020 Outstanding Teaching Assistant Award, University of Kentucky
- 05/2019 Research Challenge Trust Fund Fellowship
- 05/2019 People's Choice Award in UK Grad Teach Live competition

Scientific publications

- Fu, X., Song, Y., Masud, A., Nuti, V.S., DeRouchey, J.E., and Richards, C.I., High throughput fluorescence correlation spectroscopy enable analysis of surface components of cell-derived vesicles, *Analytical and Bioanalytical Chemistry*, 2020, 412(11):2589-2597.
- Lichtenberg, Stuart S, Nuti, Kanthi, DeRouchey, Jason, Tsyusko, Olga V, and Unrine, Jason M. "Efficacy of Chitosan/double-stranded RNA Polyplex Nanoparticles for Gene Silencing under Variable Environmental Conditions." *Environmental Science. Nano* 7.5 (2020): 1582-592. Web.
- Nuti, Kanthi., DeRouchey, Jason., Creamer Trevor., "Constrained particle transport within phase-separated liquid droplets of tau protein" (manuscript in preparation)

- Nuti, Kanthi., DeRouchey, Jason., “Particle transport in semi-dilute polymers: effect of particle charge and polymer chain charge density” (manuscript in preparation)